Brown Dwarfs and Planetary Mass Objects in Star Forming Regions:

Toward the Low Mass End of Initial Mass Function

Takuya Suenaga

Doctor of Philosophy

Department of Astronomical Science
School of Physical Sciences
The Graduate University for Advanced Studies

2013

Abstract

Brown dwarfs (BDs) and planetary mass objects (PMOs) are substellar mass objects between the planetary and stellar mass regimes ($0.013 \leq M/M_{\odot} \leq 0.075$ where M is an object's mass and $M_{\odot}$ is the solar mass). Since their discovery in the 1990s, hundreds of examples have been reported, and NASA's WISE mission has recently added another hundred BDs (Kirkpatrick et al., 2011). However, the typical thermal Jeans mass in molecular cloud cores is $\sim 1\ M_{\odot}$ (Larson, 1999, and references therein), which means that gravitational collapse of molecular clouds is expected to form stars and not BDs. Therefore, the formation mechanism of BDs and in particular that of PMOs, is still unclear.

Several theories for the formation of BDs have been suggested, including turbulent fragmentation (Padoan & Nordlund, 2004; Boyd & Whitworth, 2005), stellar embryo ejection through dynamical interactions (Reipurth & Clarke, 2001; Bate et al., 2002), disk fragmentation and scattering (Whitworth & Stamatellos, 2006a; Goodwin & Whitworth, 2007a) and photo-evaporation of embryos by nearby hot stars (Whitworth & Zinnecker, 2004). None of these theories have yet proven conclusive. Star forming theories also predict the existence of PMOs with a lowest mass limit of 0.001–0.010 $M_{\odot}$ related to the opacity of the contracting object, known as opacity-limited fragmentation (e.g., Low & Lynden-Bell, 1976; Rees, 1976; Boss, 2001; Whitworth & Stamatellos, 2006b).

Since they are not massive enough to sustain hydrogen burning and they become fainter with time, substellar objects are very faint in the Galactic field. Therefore, only a few PMOs have been reported in the field (e.g., Cushing et al., 2011). In contrast, substellar objects in star forming regions have much higher luminosities because of their gravitational energy release and therefore many BDs as well as isolated PMOs and planetary mass companion candidates have been identified (Tamura et al., 1998; Oasa et al., 1999; Lucas & Roche, 2000; Zapatero Osorio et al., 2000; Neuhäuser et al., 2008; Kuzuhara et al., 2011). Therefore, it is important for clarification of their formation processes to determine their properties, such as binarity, spatial distribution and especially initial mass function (IMF) in star forming regions.

In order to determine the low mass end of the IMF, we conducted a very deep large survey of BDs and PMOs in two well-known star forming regions, the Orion Nebular Cluster (ONC) and the Taurus Molecular Cloud (TMC). These regions are nearby rich, young stellar clusters and therefore are the most suitable for searching for BDs and PMOs.

We conducted a spectroscopic survey program in the ONC using MOIRCS mounted on the Subaru telescope and ISLE mounted on the Okayama 1.88-m telescope. We present 12 near-infrared spectra of BD candidates. We newly identify two BD candidates and a BD/planetary boundary mass object. We find that several young stellar candidates appear older in the HR diagram. The faintness can be explained by light

scattering from the central star due to the circumstellar structure, or episodic accretion. Previous studies (Kumar & Schmeja, 2007; Andersen et al., 2011) suggested that the substellar IMF in Orion depends on the distance to the central region, which means that the IMF in Orion is not universal locally. However, since previous works have been based on the photometric data, the radial dependence of the IMF could be explained by contamination of the Galactic field stars. Based on the spectroscopic data, we first show that the substellar IMF in the outer region ($r < 6'$) is consistent with the central region. The universal IMF reported around the central OB stars in Orion means that the impact of OB star's photo-evaporation process on the substellar formation is unimportant.

In the TMC, we obtained deep optical/infrared images using the Subaru/Suprime-Cam and the Okayama 1.88-m/ISLE. Since the Taurus region is widely spread in the sky, previous works have been incomplete and limited to sensitivities above 20 $M_{\rm Jup}$ (e.g., Briceño et al., 2002a; Guieu et al., 2006; Luhman, 2006; Luhman et al., 2009), where $M_{\rm Jup}$ is the mass of Jupiter. Combining our deep images with other infrared data, we achieved a sensitivity down to 6 $M_{\rm Jup}$ with a visible absorption of $A_V < 4$, the best sensitivity to date. Based on several color selections and proper motion analysis, we selected two PMO candidates and obtained spectra using the Subaru/IRCS. As a result, we did not find any PMOs in our field-of-view (FOV; 1.85 deg^2). In contrast to the abundance of PMOs of 10–20% in other star forming regions, our results suggest the abundance of low mass BDs and PMOs is quite low in the TMC. The lack of PMOs could be explained by PMOs being ejected out of the FOV, however it is unlikely that the low stellar density of Taurus promotes an ejection process from multiple stellar/planetary systems. Another explanation is that the minimum Jeans mass is higher in the TMC. However, since the previous theories predict the formation of 1–10 $M_{\rm Jup}$ objects in star forming regions, a different formation mechanism is required to explain the abundance of PMOs in the TMC.

Acknowledgement

First of all, I would like to send my special thanks to Prof. Motohide Tamura for supervising me for 5 years. He has always encouraged me to challenge new things, and given me many opportunities to start new collaborative research, to attend his leading observational projects (SEEDS; IRSF; IRD) and to access a lot of data taken by several telescopes. Without his continuous encouragement and stimulating discussion, I could have never finished this thesis.

I also deeply thank Dr. Masayuki Kuzuhara for initiating me into observational astronomy and near-infrared spectroscopy. He has taught me a lot of things from general skills for research (e.g., presentation; writing paper; programming) to various knowledge of astronomy (e.g., observational technique; data reduction; star/planet formation theories). Discussions with him are always exciting and large part of this thesis is based on discussion with him.

I would like to acknowledge Profs. Tomonori Usuda, Wako Aoki and Satoshi Mayama. They have also supervised me and supported my research. Their insightful comments have significantly improved this thesis and presentation for defense.

I would like to thank Dr. Miki Ishii for kindly providing me a chance of observing my targets using the Subaru telescope, whose spectroscopic data is absolutely necessary for discussion in this thesis. I'm also grateful to Dr. Tomoyuki Kudo for acquiring the spectroscopic data at the Subaru telescope instead of me.

I am indebted to Dr. Norio Narita who has kindly observed a lot of my targets using a part of his allocation times of the Okayama 1.88m/ISLE. Dr. Akihiko Fukui has also observed many objects of our targets, and provided me the reduction pipeline developed by himself for ISLE data. I thank Dr. Kenshi Yanagisawa for support to use ISLE since it was a PI instrument.

I would like to thank Dr. Michael W. McElwain for collaborating to apply the proposals to the Gemini telescope. His great efforts have significantly improved my observational strategy. Dr. John P. Wisniewski has kindly provided me a chance of observation with the 3.5-m telescope at Apache Point Observatory. I also appreciate Dr. Philip W. Lucas who has given invaluable comments on my first paper and helpful advices in applying proposal for a telescope.

I'm thankful to referees, Profs. Nobuharu Ukita, Yoichi Takeda, Fumitaka Nakamura, Koji Sugitani, and Masahiro Machida. I also would like to express my gratitude to the PhD students of NAOJ, Mr. Yoshifumi Ishizaki, Mr. Keisuke Imase, Mr. Yasuhiro Takahashi, and all of colleagues of NAOJ/GUAS. I am deeply grateful to my best friend, Asuka Murata for her strong encouragement. Finally, my heartfelt appreciation goes to my family, my young brother, Kazuya, my dog, Punch, and especially my mother, Kayoko for continuous support.

Contents

List of Tables

List of Figures

Chapter 1

Introduction

The IMF (initial mass function) has been first introduced by Salpeter (1955) as a convenient way of parameterizing the relative number of stars as a function of their mass. The IMF provides an essential observational input to many astrophysical studies, and various predictive theories of star formation have been proposed to explain its shape, as well as whether it is universal or is instead sensitive to environmental conditions. Nearly 60 years after being first proposed, Salpeter's IMF is still considered the standard for stars above 1 $M_{\odot}$, where $M_{\odot}$ is the solar mass. The development of observational instruments and techniques has enabled the substellar mass population below 1 $M_{\odot}$ to be revealed, and the analytical form of stellar IMF has been extended to explain the distributions of the substellar population. Recent deep observations have achieved a sensitivity below the mass of the hydrogen burning limit (0.075 $M_{\odot}$) in several young stellar clusters. In order to reveal the shape of the substellar IMF, as well as the population in the planetary mass regime ($< 0.013\ M_{\odot}$), we have conducted a large deep survey in very young star forming regions. In this chapter, we introduce the definition of the IMF, discuss previous works from the substellar to planetary mass regimes, present the formation theory of brown dwarfs (BDs) and planetary mass objects (PMOs) , and consider previous studies of star forming regions.

1.1 Form of the Initial Mass Function

In 1955, Salpeter (1955) suggested a power-law IMF to explain the stellar number distribution in Galactic field regions:

$$\Phi(\log(m)) = dN/d\log(m) \propto m^{-\Gamma} \tag{1.1}$$

where m is the stellar mass, N is the number of stars and $\Gamma \sim 1.35$. This single power law IMF is known as the Salpeter IMF.

In the period 1980–1990, observational technology developed significantly and the observable range of stellar masses was extended to below the solar mass. In order to explain the stellar distribution by the IMF of the extended mass range, Kroupa et al. (1993) suggested a multi-segment power law for the IMF:

$$\chi(m) = dN/dm \propto m^{-\alpha} \tag{1.2}$$

where $\alpha = \Gamma + 1$ is derived as follows:

$$\chi(m) = 1/m(\ln 10)\Phi(\log m) \tag{1.3}$$

This type of IMF is known as the Kroupa IMF, and the slope of the Salpeter IMF is described by $\alpha = 2.35$.

The log-normal IMF was suggested by Miller & Scalo (1979):

$$\Phi(m) \sim \exp(\frac{(\log m - \log m_c)^2}{2\sigma^2}) \tag{1.4}$$

where m_c is the mean mass and σ is the standard deviation of the mass distribution . Chabrier (2003, 2005) developed a form of the IMF to fit the substellar number distribution with a power-law tail above the solar mass. The log-normal IMF is called the Chabrier IMF. Another functional form was proposed by de Marchi & Paresce (2001) as a truncated exponential where $dN \propto M^{-\alpha}(1 - \exp[(-M/M_p)^{-\beta}])dM$.

Above $\sim 0.2\ M_\odot$, the multi-segment power law and log-normal agree very well, as shown by Figure 1.1. However, the form of the IMF at low masses is still relatively uncertain and subject to ongoing debate. For instance, Chabrier IMF assumes that the stellar IMF smoothly connects to the substellar IMF. On the other hand, Thies & Kroupa (2007) have proposed a discontinuity in the IMF at the stellar/substellar boundary and suggested that the discontinuity implies a difference in the formation processes in the two mass ranges.

1.2 Substellar IMF in Various Galactic Clusters

From the early stages of IMF study, a power-law IMF with $\alpha = 2.35$ is usually adopted to the Galactic field stellar population above 1 $M_\odot$. Between 0.1 and 0.8 $M_\odot$, the IMF is relatively well constrained due to recent studies based on local stars with Hipparcos parallax (Reid et al., 2002) and a much larger sample of field stars with less accurate photometric distances (Covey et al., 2008; Bochanski et al., 2010). The results of these studies suggest the single star IMF at low masses is well described by a power law with $\alpha \sim 1.1$.

Extending the study down to the BD mass regime requires observing these objects in young star forming regions, where these objects are young, since BDs and PMOs become fainter with time due to a lack of energy to burn hydrogen. The UKIDSS Galactic Cluster Survey is the deepest and largest survey covering nearby clusters with a wide range of age (1–600 Myr) using the WFCAM camera mounted on the 3.8-m UKIRT telescope. This survey has revealed the substellar IMF in several rich stellar clusters, including IC4665 (Lodieu et al., 2011a), Pleiades (Lodieu et al., 2007, 2012a), α Per (Lodieu et al., 2012b), Praesepe (Boudreault et al., 2012) and Upper Sco (Lodieu et al., 2007; Lodieu, 2013). The results are mainly based on infrared photometry and astrometric analysis, and agree well with previous studies of the Galactic field, indicating that the IMF is well represented by a power law with $\alpha \sim 0.6$ in the mass range 0.03–0.5 $M_\odot$

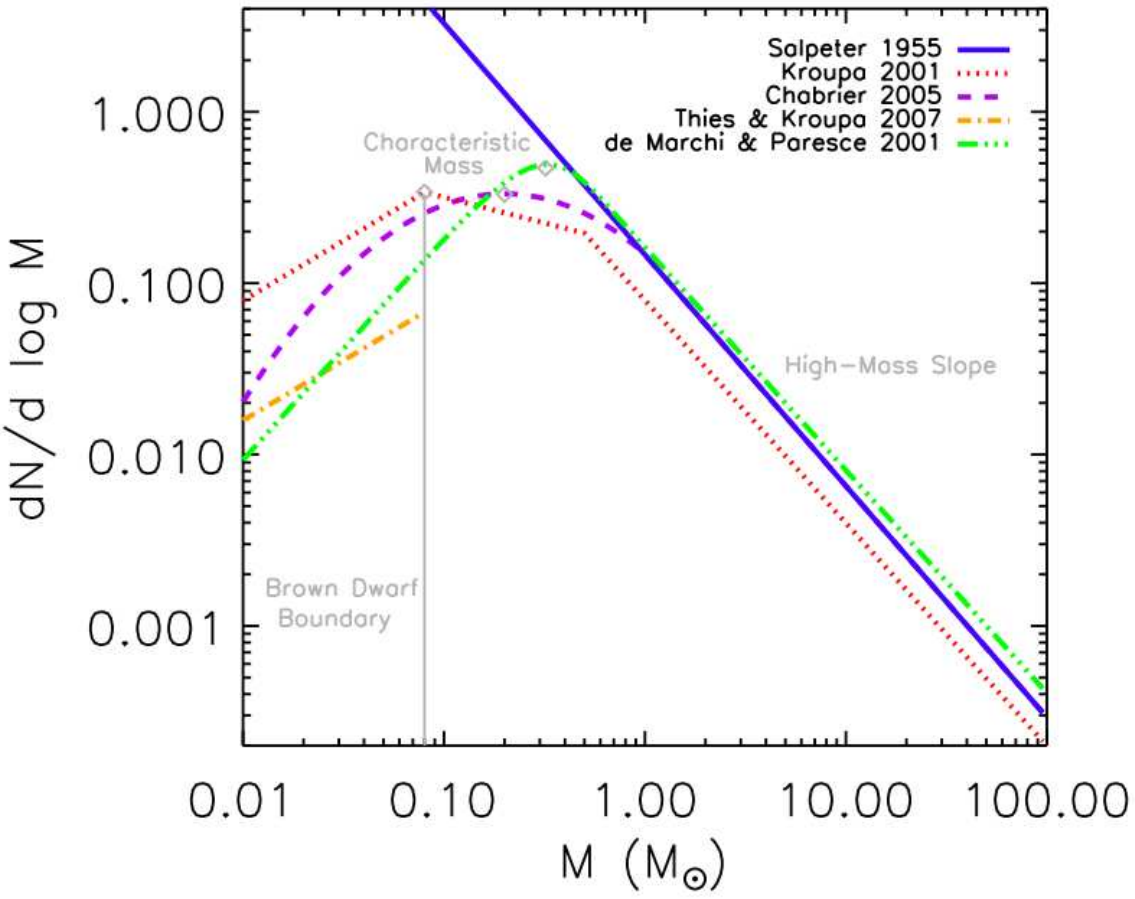

Figure 1.1: IMF functional forms proposed by various authors from fits to Galactic stellar data (Figure 1 of Offner et al., 2013). With the exception of the Salpeter slope, the curves are normalized such that the integral over mass is unity. When comparing with observational data, the normalization is set by the total number of objects, as shown in Figure 1.2.

or log-normal with a peak mass around 0.2–0.3 $M_{\odot}$ and $\sigma \sim 0.5$. Note, however, that in the lower mass range of Upper Sco below 0.03 $M_{\odot}$, an excess of low-mass BDs has been reported, which may result from uncertainties in the mass–luminosity relation at very low masses and cluster ages (Lodieu, 2013). A large systematic survey, called the Substellar Objects in Nearby Young Clusters (SONYC) project, has been conducted in several star forming regions, including NGC1333 (Scholz et al., 2009, 2012b,b), ρ Oph (Geers et al., 2011) and Cha I (Mužić et al., 2011, 2012). This project was established to study a large low-mass population from the BD to planetary mass regimes in young star forming regions (< 10 Myr) using a wide FOV camera (Suprime-Cam) and a multi-object slit spectrograph (MOIRCS; FMOS) mounted on a large telescope (Subaru; VLT). The project has made a significant effort in studying NGC1333 to achieve completeness down to several Jupiter masses It has been shown that the IMF of $\alpha = 0.61$ ($0.015 \leq M/M_{\odot} < 0.7$) is consistent with the Kroupa IMF. For σ Orionis, which is a well-studied field of PMOs (e.g., Caballero et al., 2007; Bihain et al., 2009), Peña Ramírez et al. (2012) have conducted wide (~ 0.78 deg^2) and deep (translated masses down to ~ 0.004 $M_{\odot}$) optical/infrared imaging based on VISTA Orion survey data (Petr-Gotzens et al., 2011). They have reported that the σ Orionis cluster contains as many BDs (69 sources, $0.012-0.072$ $M_{\odot}$) and PMOs (37 sources, 0.004–0.012 $M_{\odot}$) as low-mass stars (104 sources, 0.072–0.25 $M_{\odot}$), and the IMF in the cluster could be flatter than the Galactic field IMF , similar to the case for Upper Sco. A more comprehensive review has been presented in Bastian et al. (2010) and Jeffries (2012).

1.3 Our Research Motivations and Focuses

Our main goal is to provide new insights into the fields of low-mass star formation: the universality of IMF; the bottom of IMF; formation of BDs and PMOs. In this section, we introduce the recent studies related with theses topics.

1.3.1 Universality of IMF

It is critically important to reveal whether the IMF is universal or is instead sensitive to environmental conditions is of critical importance. Although the shape and universality of the IMF is still under investigation, studies of the Galactic field, star forming regions, young open clusters and old globular clusters suggest that the vast majority were drawn from a universal IMF, as seen in Figure 1.2. Andersen et al. (2008) have suggested that the ratio of stars to BDs (> 30 $M_{\rm Jup}$) in seven young clusters can be explained by a log-normal IMF. Also, the characteristic mass of the IMF is very shallow ($\sim$ 0.1–0.4 $M_{\odot}$) in spite of the various initial conditions (Bastian et al., 2010), except for the Taurus Molecular Cloud (TMC) in which the characteristic mass is higher (~ 0.8 $M_{\odot}$) and a lack of substellar mass objects has been reported (e.g., Briceño et al., 2002a). Luhman et al. (2009) has updated the Taurus IMF based on Spitzer, X-ray data and follow-up spectroscopy, and found a 0.04% chance from a Kolmogorov–Smirnov test that the Taurus IMF could be drawn from the same parent distribution as the IC348 and Chameleon I IMFs. Previous explanations for the unusually high peak mass in Taurus have generally involved a higher average Jeans mass compared to other regions (Briceño et al., 2002a; Goodwin et al., 2004). A recent numerical simulation by Bonnell et al.

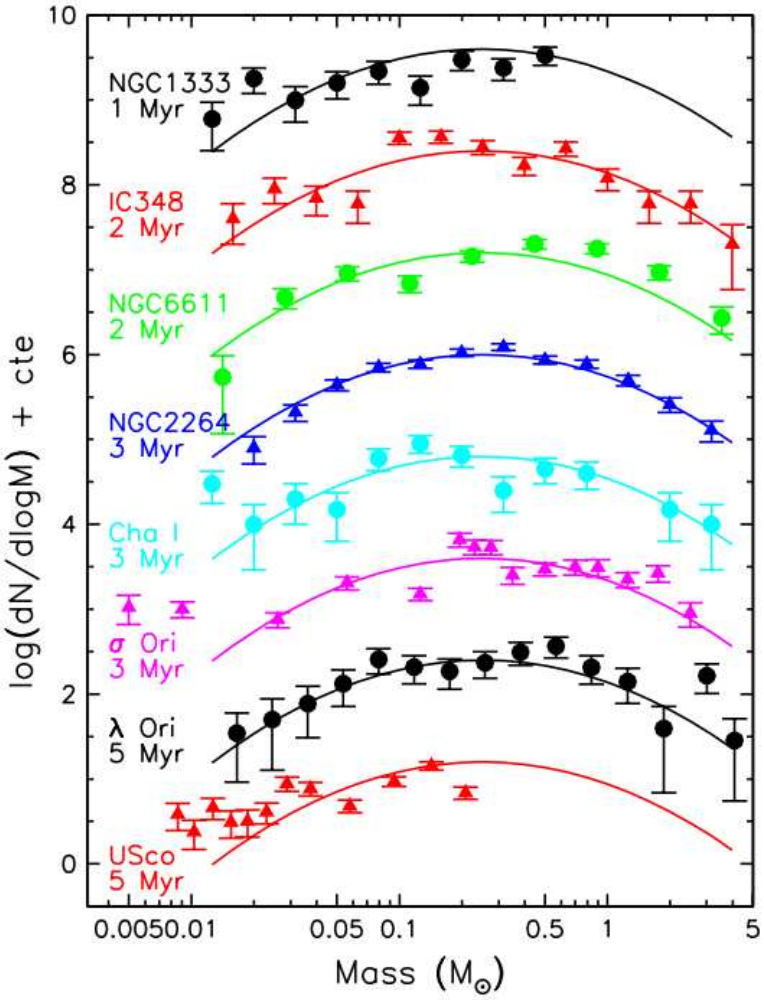

Figure 1.2: Recent IMF estimates for eight star forming regions (Figure 2 of Offner et al., 2013): Scholz et al. (NGC1333, 2012a); Alves de Oliveira et al. (IC348, 2013), Oliveira et al. (NGC6611, 2009); Sung & Bessell (NGC2264, 2010); Luhman (Cha I, 2007); Peña Ramírez et al. (σ Ori, 2012); Bayo et al. (λ Ori, 2011); Lodieu (Upper Sco, 2013). The error bars represent the Poisson error for each data point. The solid lines are not a fit to the data, but are a log-normal form proposed by Chabrier (2005) for the IMF, normalized to best follow the data.

(2011) has also reproduced the variations in the peak mass and shape of the IMF between Taurus and other clusters. They included gravitational fragmentation of infalling gas into a stellar cluster and therefore the gravitational potential, and thus the object density, in the cluster might also be a critical parameter for the formation of substellar mass objects.

To date, the substellar population has been determined for several young clusters. However, since many observations of substellar objects are still spatially limited, such studies are biased to the central regions or high stellar density regions in the clusters. Reipurth & Clarke (2001) suggested that proto-BDs ejected from multiple protostellar systems generate different velocity and spatial distributions from the massive stars. These predictions provide valuable motivation for a wide range of observational studies distinguishing the formation processes of star and substellar mass objects. Note that the typical ejection velocities are at most a few km/s, and therefore comparable with the velocity dispersion between neighboring cores and the velocity dispersion for more massive stars (Bate et al., 2003). However, there should be a high-velocity tail in the distribution of ejection velocities, yielding an extended halo of BDs. Therefore, in order to reveal the whole population and their formation , analyses based on the data with a wider FOV have been conducted for several young clusters. The Orion Nebular Cluster (ONC) is a rich and compact stellar cluster, which is expected to exhibit frequent ejection due to dynamical interactions. Andersen et al. (2011) have conducted wide FOV imaging using HST/NICMOS and revealed the spread in the population of the BD mass regime for massive stars. A different spatial distribution has been suggested by Kumar & Schmeja (2007), whose analysis generated distributed BD mass populations of both ONC and IC348. Their analysis indicated that the BDs appear slightly more centrally concentrated for the 1 Myr old ONC than for the 3 Myr old IC348, which implies that the ejected BDs spread away from their birth place with time. In σ Orionis, the radial profiles of stars and BDs are similar, but an underabundance of planetary mass candidates in the central region has been reported (Caballero et al., 2007; Peña Ramírez et al., 2012). In contrast, Luhman (2006) observed the entire region and found no spread in the BD population to the massive stars . However, these results should be treated carefully due to observational incompleteness. Wide FOV surveys of ONC and IC348 have not yet been completed spectroscopically, and contamination from Galactic field stars could be dominant in the outer regions where the background nebulosities become faint. In the case of σ Orionis, previous works have probably missed planetary mass candidates at the center of the cluster since the bright OB stars at the cluster center could hide faint objects. Bouy et al. (2009) studied the core of σ Orionis using adaptive optics and found a relatively large number of planetary mass candidates. If confirmed to be true σ Orionis members, they would increase the central abundance of the planetary mass population. In the TMC, a recent spatial analysis (Parker et al., 2011) suggested a slightly different distribution of substellar mass objects to massive stars using the previous survey data. This result implies that the substellar objects are not spread to the massive stars , but the number of substellar mass samples is not statistically sufficient for a definitive conclusion. Thus, confirming the spatial universality of the substellar IMF has been controversial. In order to confirm whether the substellar IMF changes in different environments, a wider region must be studied to reveal the whole population in a cluster with a spectroscopic follow-up.

1.3.2 IMF Bottom Limit

Subsequent to their discovery (e.g., Tamura et al., 1998; Oasa et al., 1999; Lucas & Roche, 2000; Zapatero Osorio et al., 2000), the existence of isolated PMOs of below 0.013 $M_{\rm Jup}$ has been reported in young star forming regions. The largest survey of NGC1333 to date has determined the spectroscopic census of the IMF down to 6–8 $M_{\rm Jup}$ (Scholz et al., 2012b). This survey shows that the planetary mass population is largely consistent with a monotonic continuation of the power law with $\alpha = 0.61$ ($0.015 \leq M/M_{\odot} < 0.7$). The compiled results for other regions (σ Ori; Upper Sco; ρ Oph) demonstrate that the slope of the mass function for the planetary domain is $\alpha \lesssim 0.6$ in star forming regions. The current census of star forming regions therefore supports the idea that PMOs are an extension of the population of stars and BDs and form through the same mechanism. Note however that spectroscopic studies in star forming regions other than NGC1333 have not yet been completed below 0.013 $M_{\odot}$. In the lower mass regime, a microlensing survey has provided evidence of many objects of $M \lesssim 0.005\ M_{\odot}$ (Sumi et al., 2011). These results imply that a few such Jupiter mass objects have a different origin to the star forming process. They may have formed in the protoplanetary disks like planets. However, no spectroscopic observations to date have achieved sufficient depth to detect objects of a few Jupiter masses.

Many theoretical studies have analytically and numerically predicted the bottom limit of the IMF to be 0.001–0.010 $M_{\odot}$. Low & Lynden-Bell (1976) indicated that the minimum Jeans mass of a fragment depends strongly on the background radiation and weakly on the metallicity ($Z^{-1/7}$). Considering the typical temperature in molecular clouds to be 10 K, they have shown that the minimum mass is 0.007 $M_{\odot}$. Boss (2001) performed a hydrodynamical simulation including magnetic field effects, giving a central rebound and cooling that allows a multi-stellar system to form by fragmentation and an isolated PMO ($\leq 1 M_{\rm Jup}$) to be ejected from the system. Bate (2005) investigated the dependency of the IMF on the metallicity by setting the non-isothermal critical density to be a factor of 9 lower than the typical value, which is intended to mimic the thermal behavior of a molecular gas with a lower metallicity ($\log(Z/Z_{\odot}) = -3.3$). Their large-scale hydrodynamical simulation found that a low metallicity increases the minimum mass of a BD by a factor of 3 to 9 $M_{\rm Jup}$. Whitworth & Stamatellos (2006b) calculated the minimum mass based on various star forming scenarios: hierarchical fragmentation of a 3D medium, 2D fragmentation of a shock-compressed layer, and fragmentation of a circumstellar disc. Although these scenarios are very different from each other, the authors showed that the minimum mass is in a narrow range of 0.001 to 0.004 $M_{\odot}$. Therefore, at the limit of IMF, predicted to be 0.001–0.010 $M_{\odot}$, if BDs and PMOs are born as stars, the IMF will be consistent with the extrapolation of the stellar IMF. On the other hand, if they born as planets, the IMF may differ from the extension of the stellar IMF. An observation that determines the abundance of BDs and PMOs in various regions will uncover their formation process.

1.3.3 Formation of BDs and PMOs

Several mechanisms have been proposed for the formation of low-mass stars and BDs. They can be summarized as follows:

Turbulent fragmentation — The turbulent flow in a molecular cloud triggers compression and fragmentation of gas, which produces collapsing cores with a wide range of masses (Padoan & Nordlund, 2004; Boyd & Whitworth, 2005). The mass of each core determines the mass of the resulting star. Low-mass stars and BDs arise from the smallest cores. While this scenario predicts a large production of low mass stars and the lower typical mass of the IMF under conditions of higher turbulent velocity, it suggests that the general form of the IMF remains unchanged. Therefore, this scenario is consistent with the universality of the IMF observed in several star forming regions. However, high resolution is required to detect such small cores and they have a short dynamical timescale ($\sim 10^4$yr). In fact, although some studies have achieved sufficient sensitivity to detect such low-mass cores (e.g., André et al. 2010; $M \sim 0.01 M_{\odot}$), it has been found that these cores cannot gravitationally contract, with the exception of a study by André et al. (2012) who detected a possible BD mass core using an interferometer.

Dynamical ejection from proto-stellar or proto-planetary systems — In this theory, the existence of a few ($\lesssim 3$) objects is supposed in the proto-stellar or proto-planetary systems. As these objects dynamically interact with each other, the lowest mass object(s) will be ejected from the systems, which prematurely halts their accretion (Reipurth & Clarke, 2001; Bate et al., 2002). This process is a straightforward mechanism in multi-stellar systems. In fact, most protostars are born as binaries or even multi-stellar systems (Ghez et al., 1993; Leinert et al., 1993; Reipurth, 2000) and the dynamical interaction and ejection is enhanced in such an environment. This scenario is amenable to observational studies that allow low-mass stars and BDs to be distinguished from massive stars by their spatial or velocity distribution. However, to date no studies have identified clear differences between stellar and BD properties (White & Basri, 2003).

Fragmentation of infalling gas into a stellar cluster — The gravitational potential of a forming stellar cluster provides a focus that attracts gas from the surrounding molecular cloud. Filament structures formed into cluster centers attain high gas densities due to the combination of the cluster potential and local self-gravity. The resultant Jeans masses are low, allowing the formation of very low mass fragments (Bonnell et al., 2008). This theory predicts that the abundance of low mass populations like that of BDs depends on the stellar density in the cluster. Also, the dependency of the Jeans mass on the stellar density explains the variation of the IMF in Taurus (Bonnell et al., 2011).

Fragmentation of massive circumstellar disks — The gravitational fragmentation of massive circumstellar disks around central stars produces low-mass companions. Some of these objects are ejected through dynamical interactions with other companions or nearby stars (Whitworth & Stamatellos, 2006a; Goodwin & Whitworth, 2007a). In clusters, the gas interaction of two disks may promote BD and PMO formation (Shen et al. 2010). However, such massive disks ($\sim 0.1 M_{\odot}$) producing BDs and PMOs are rare in studies of star forming regions. Eisner & Carpenter (2006) observed infrared protostellar objects in the ONC and concluded that the abundance of massive discs ($> 0.1 M_{\odot}$) is less than 2 %.

Photo-evaporation of OB stars — Photo-ionizing radiation from OB stars halts accretion by removing much of the envelope and discs of nearby low-mass protostars (Whitworth & Zinnecker, 2004).

However, this scenario applies only in the vicinity of OB stars and cannot for example be adopted for the TMC.

Since the theories of BDs and PMOs have reached controversial conclusions so far, it is important to test these theories though observations in star forming regions and to investigate low-mass star properties, such as binarity, spatial distribution and especially the IMF, in star forming regions. Recently, a radial velocity survey has determined the frequency of extra-solar planets. By combining this planetary frequency data with stellar binary data, a clear difference in the mass functions between companions to G-type stars and planets has been determined. This difference is thought to be associated with the difference in their formation mechanisms. Therefore, we need to study substellar IMF, including binaries, to confirm whether there is a difference in their formation scenarios.

1.4 Instruments Used and Star Forming Regions Considered in This Thesis

In order to determine the substellar IMF, we observed two well-studied star forming regions using several instruments. In this section we introduce the instruments and previous works on the star forming regions.

1.4.1 Instruments

The Subaru telescope is an 8.2-m optical–infrared telescope at the summit of Mauna Kea, Hawaii, operated by the National Astronomical Observatory of Japan (NAOJ). The telescope is enclosed within a cylindrical dome, whose shape was designed to reduce air disturbance. The median image size (full width at half maximum; FWHM) of the Subaru telescope is 0.6″–0.7″ in the R band (∼6500Å) based on the seeing size statistics collected by the CCD camera of an auto guider during focus checks. The Subaru telescope has a number of common-use instruments for imaging and spectroscopy with a wide wavelength coverage from optical to mid-infrared.

The Okayama 1.88-m telescope is one of the largest telescopes in Japan, operated by the Okayama Astrophysical Observatory (OAO). The 1.88-m telescope is located at the top of Mt. Chikurin-ji, which is the best astronomical site in Japan. The astronomical seeing at OAO is fairly good and the image size of stars is typically 1.4″. The telescope has several open-use instruments for imaging and spectroscopy with wavelength coverage from optical to near-infrared.

The United Kingdom Infra-Red Telescope (UKIRT) has a 3.8-m primary mirror capable of optical–infrared photometry and spectroscopy, located at the summit of Mauna Kea. The UKIRT is currently being operated by the Joint Astronomical Centre (JAC) in a transitional phase toward new ownership. The median image size of the UKIRT is 0.4″–0.5″ in the *K*-band , which was systematically monitored and corrected for undersampling in February 1999. Since 1 January 2011, the UKIRT has been operating in a

"minimalist mode" and all available observing time has been used to complete the UKIDSS program.

The Spitzer Space Telescope is an infrared space observatory, and the final mission in NASA's Great Observatories Program. Spitzer has a 0.85-m primary mirror and three cryogenically cooled science instruments, which are capable of sensitive imaging and spectroscopy from mid to far infrared wavelengths. On the May 15, 2009, Spitzer used the last of the superfluid helium aboard the spacecraft. Subsequently, the two shorter-wavelength modules of the IRAC camera have been operated in the Spitzer Warm Mission.

The Wide-field Infrared Survey Explorer (WISE) is a NASA-funded Explore mission that is designed to conduct an all-sky survey with a 0.4-m primary mirror and a mid–far infrared detector. WISE has provided an all-sky map of the infrared wavelength. This spacecraft had been in hibernation without ground contact from February 17, 2011, but was restarted for a new mission to search for asteroids in 2013.

1.4.2 Star Forming Region 1: Orion Nebular Cluster

The ONC is the most suitable star forming region for IMF studies. It is nearby, $\sim$ 450 pc (Muench et al., 2008), and young, $\leq$1 Myr (Hillenbrand, 1997; Riddick et al., 2007). Previous studies of the ONC have concentrated on the central part of the ONC region. Hillenbrand (1997) conducted an optical imaging survey and spectroscopic follow-up, including collecting spectra for $\sim$ 900 stars, and measured the stellar masses down to $\sim$ 0.1 $M_{\odot}$ within 4.5 pc $\times$ 4.8 pc ($34' \times 36'$) of the Trapezium cluster. Luhman et al. (2000) conducted infrared imaging at the central region of the Trapezium cluster ($140'' \times 140''$; 0.3 pc $\times$ 0.3 pc) and $K-$ band spectroscopy for $\sim$ 100 sources. Slesnick et al. (2004) performed 97 J- and K-band spectroscopy measurements of the inner $5.1' \times 5.1'$ region of the ONC (Hillenbrand & Carpenter, 2000). Although they confirmed the presence of many low-mass cluster members and even BDs of masses down to 0.02 $M_{\odot}$, the bright nebulosities made it difficult to extend the measurements to lower masses. In order to cover a larger area of the ONC, deep and wide imaging surveys have been conducted (Robberto et al., 2010; Andersen et al., 2011; Da Rio et al., 2012). Andersen et al. (2011) have discontinuously covered a large area ($26' \times 33'$) using HST/NICMOS Camera 3. Over the observed area, they have shown that the IMF in the whole of the ONC become fatter in the substellar mass regime, and the relative abundance of BDs to stars increases from the center to the outer regions. Meanwhile, Da Rio et al. (2012) have also covered a large FOV ($32' \times 33'$) with a WFI camera mounted on the 2.2-m MPG/ESO telescope. They have determined the IMF down to 0.02 $M_{\odot}$, finding that it declines steeply with decreasing mass, and they have found no evidence of IMF flattening toward the substellar mass regime. The inconsistency between Andersen et al. (2011) and Da Rio et al. (2012) may be explained by different estimates of the background contamination. In order to confirm the validity of these studies, a wider coverage area spectroscopic study with multi-object spectrographs is required. However, no spectroscopic observations of the targets have yet been made. Lucas et al. (2005) have made observations focused on the outer regions of the ONC, where fainter nebulosities enable the observation of fainter objects. They detected 33 faint planetary mass candidates. To confirm their cluster membership, spectroscopic observations were conducted and about 10 PMO candidates were identified as young stellar objects (Lucas et al., 2006; Weights et al., 2009). However, many of the photometric candidates have not yet been spectroscopically examined. It is important to observe the candidates for

characterization of the BDs and PMOs in this region.

Aim to observe the ONC

We therefore have conducted spectroscopic follow-up observations of the Lucas et al. (2005) candidates, and found two new young BDs and a BD/planetary-mass boundary object.

The universality of substellar IMF in the ONC — In previous works, the authors have conducted spectroscopy to concentrate on the central regions in the ONC, however the spectroscopic follow-up have been uncompleted on the outer regions. We identify several stellar and substellar members with spectroscopy from the candidate list of Lucas et al. (2005), and compile the spectroscopic sample of the outer regions in the ONC. In comparison of our sample with the previous works in the central regions, we can first discuss the universality of substellar IMF in the ONC based on the spectroscopic sample.

The impact of OB star's photo-evaporation process on the substellar formation — The ONC is a well-studied massive star forming region and has some OB stars, Trapezium stars at the central regions. Therefore, if the process of photo-evaporation of OB stars was dominant for the substellar formation, we would find the central concentration of the substellar mass objects for the stellar mass members. Since our observed region is located away from the center, we can check the impact in comparison of our sample with the sample of the central regions.

1.4.3 Star Forming Region 2: Taurus Molecular Cloud

The TMC is one of the best star forming regions to study the origin of PMOs because of its proximity (140 pc) and youth ($\sim$ 1 Myr) (see Kenyon et al. 2008 for a review). Several surveys have been conducted in the Taurus region to investigate its IMF down to the substellar regime. Briceño et al. (2002a) have combined their optical photometry of several clustered regions with near-infrared data from 2MASS, and identified some low-mass members from optical spectroscopy. They constructed the Taurus IMF with $A_V < 4$ samples covering $\sim$ 8 deg^2 and determined the deficit of BD mass members in the TMC, compared with the Orion Trapezium cluster. Luhman (2004) have conducted optical imaging covering $\sim$ 4 deg^2 and combined the data with the 2MASS catalogue. They identified new low-mass members from optical spectroscopy, and added the data to the previous studies (Briceño et al., 2002a; Luhman et al., 2003a). They constructed the IMF totally covering $\sim$ 12 deg^2 and found that the relative ratio of substellar mass to stellar mass is slightly higher than those determined by Briceño et al. (2002a) and Luhman et al. (2003a). Since there are no observations from which to fully generate the census of low-mass population (M2–M6) in TMC, their IMF could be overestimated. However, since Slesnick et al. (2004) revised the number of BDs per star downwards, the difference in the BD/star number ratio might be small between the TMC and Trapezium. Guieu et al. (2006) have conducted a wider survey ($\sim$ 28 deg^2) with CFHT and the optical large FOV camera CFHT12k (Cuillandre et al., 2000) and MegaCam Boulade et al. (2003), and obtained optical spectra of selected low-mass candidates. Their work is not complete in the spectral range M2–M4, but they were able to estimate the BD/star number ratio to be higher than the result of Luhman (2004). However, Luhman

(2006), who covered the entire area of the TMC ($\sim$ 225 deg^2) with an all sky survey catalogue (2MASS and USNOB-1.0), has indicated that the incompleteness of Guieu et al. (2006) is worse than originally thought by appropriately considering the missed known members in their selection procedure. As a result, Luhman (2006) found a BD/star number ratio of Guieu et al. (2006) similar to that of Luhman (2004). Luhman et al. (2009) have conducted optical and infrared spectroscopy for low-mass candidates selected using 2MASS, *Spitzer*, and XMM-Newton Observatory data Scelsi et al. (2007). They have determined the substellar population down to 20 $M_{\rm Jup}$ covering 5 deg^2 in Taurus, and updated the IMF previously constructed by the authors. The IMF closely resembles those they previously reported. Moreover, they have found the first probable PMO candidate, 2MASS J0437+2331 in their TMC survey. Since they determined that the optical SpT is L0 and the object shows no infrared excess, they have concluded that the object is a young disc-bearing L-type member. Alves de Oliveira et al. (2012) have obtained the near-infrared spectrum with Gemini/GNIRS as a young L0-type template. The spectrum shows strong water absorption, which means it is probable that the object has a very cool temperature as an L-type object. In summary, many authors have investigated the population in TMC, but it nevertheless remains difficult to measure a reliable BD/star ratio due to the wide spread of TMC in the sky and the observational incompleteness for early M-type members. In addition, the previous surveys were only sensitive to substellar objects down to 20 $M_{\rm Jup}$ due to limitations in the survey depth, and hence the planetary mass population has not been fully revealed.

Recently, some deep surveys have achieved a sensitivity capable of detecting even PMOs. Quanz et al. (2010) have performed deep near-infrared imaging covering 1 deg^2 with OMEGA2000 mounted on the Calar Alto 3.5-m telescope. They found six planetary mass candidates and obtained the *J*-band spectra. Although they conclude that some candidates may be Galactic giant stars or carbon stars, one candidate (CAHA Tau 1) seems to be a young planetary mass object. However, Luhman & Mamajek (2010) have concluded that the candidate is a high mass member through their obtained near-infrared spectrum. The completeness of Quanz et al. (2010) is limited for the SDSS data, which is used as an optical counterpart for their infrared data. Therefore, when they combine their infrared data with deeper optical data, they may find other planetary mass candidates. Todorov et al. (2010) have found a very faint object as a companion to a central BD 2MJ04414489+2301513 (SpT$\sim$M8.5; Luhman 2006) using HST and Gemini with the AO instrument. They have converted the K_s-band magnitude to the luminosity with a bolometric correction, and the luminosity indicates that the object has 5–10 $M_{\rm Jup}$by comparing with the predicted luminosity from theoretical evolutionary models for an age of 1 Myr. Luhman et al. (2009) have found the first probable PMO candidate 2MASS J0437+2331 in their TMC survey. Since they determined that the optical SpT is L0 and the object shows no infrared excess, they have concluded that the object is a young disc-bearing L-type member. Alves de Oliveira et al. (2012) have obtained the near-infrared spectrum with Gemini/GNIRS as a young L0-type template. The spectrum shows strong water absorption, which means it is probable that the object has a very cool temperature as an L-type object. A few PMOs have been found so far in TMC, but the sensitivity and completeness of the previous surveys is still limited.

Aim to observe the TMC

In order to reveal the planetary mass population, we need to conduct much deeper and wider observations.

The bottom of IMF in the TMC — Previous observations have achieved the sensitivity down to 20 $M_{\rm Jup}$, however the IMF of lower (planetary) mass regimes have never been revealed. Our ultra-deep imaging with the Subaru/Suprime-Cam allows us to first study the bottom of the IMF in the TMC. In some star forming regions (e.g., ONC; Cha I; σ Ori), recent deep observations have found several PMO candidates. However, there is no large spectroscopic observations except NGC1333 (Scholz et al., 2012b). Therefore, we can first compare it with our result based on the deep imaging/spectroscopy data.

The impact of several substellar forming theories on the PMO formation — Scholz et al. (2012b) have suggested that the frequency of PMOs can be explained by the extrapolation of a monotonic power law of the substellar IMF. Thus their result supports for the idea that PMOs are an extension of the population of stars and BDs and form through the same mechanism. Therefore, if it was true for other star forming regions, we would find some PMOs in the TMC. On the other hand, since current star forming theories do not distinguish between PMOs and massive stars, if we found many or few PMOs in the TMC, we would need additional scenario to explain the result.

1.5 Originality and Outline of This Thesis

We have previously introduced the IMF, performed observations of BDs and PMOs in various star forming regions, in particular the ONC and TMC, and formulated the formation theories for BDs and PMOs. In this thesis, we develop a form for the low mass end of the IMF, and determine the formation mechanism and properties of BDs and PMOs. In this respect, the ONC and TMC are the most suitable locations because of their proximity, young age, and rich stellar abundance. Several noteworthy points of this thesis can be summarized, as follows:

1. We observed a very faint object of the ONC using a multi-object slit spectrograph, Subaru/MOIRCS. The ONC is a rich compact cluster and the best field for statistical investigation of BDs and PMOs. However, it takes a long time to observe a large number of very faint BDs and PMOs with a long slit spectrograph. Therefore, we used the Subaru/MOIRCS, which enabled us to obtain many spectra of faint substellar objects simultaneously.

2. We developed a reduction pipeline and algorithm to derive the physical parameters . After the observation with MOIRCS, we needed to conduct a reduction of many raw frames. Therefore, we developed a pipeline which enabled us to obtain 1-D spectra from 2-D raw images semi-automatically. We also developed an algorithm for determining the physical parameters and to evaluate the uncertainty using the programming language Python.

3. We obtained a huge number of deep images in the TMC using a large FOV camera mounted on the Subaru telescope, Suprime-Cam. The TMC is the best location for studying PMOs, but it is widely spread in the sky and the coverage by previous studies has been insufficient. Our wide ultra-deep imaging with Subaru/Suprime-Cam can reveal very low mass populations, even of PMOs, in this region.

4. We adapted the optical filters of the Suprime-Cam to select PMOs efficiently. Usually, studies observing star forming regions use IR instruments because they exhibit the advantage of visual extinction of the molecular cloud. However, as shown in Figure 1.3, since the fluxes at the optical wavelength are clearly different between host massive stars and cool substellar objects, we can distinguish substellar objects from massive stars by combining the deep optical data with near IR data.

In Chapter 2, we describe a spectroscopic study of the ONC using Subaru/MOIRCS and the OAO 188-cm telescope + ISLE. We identify three new BD candidates from 12 spectra. We derive their physical parameters using χ^2-fitting and the HR diagram. We discuss the properties of each object and the star forming history in Orion. In Chapter 3, we show the results of wide and ultra deep optical imaging with Subaru/Suprime-Cam, an infrared imaging follow-up with OAO/ISLE, and infrared spectroscopy of BD and PMO candidates. By combining these data, we achieved a sensitivity down to several planetary masses at optical to infrared wavelengths. We select two PMO candidates and obtain their spectra using Subaru/IRCS. Finally, we discuss the ratio of PMOs to BDs in the TMC. In Chapter 4, we end with a summary and conclusions of this thesis.

[a] See http://pono.ucsd.edu/~adam/browndwarfs/spexprism

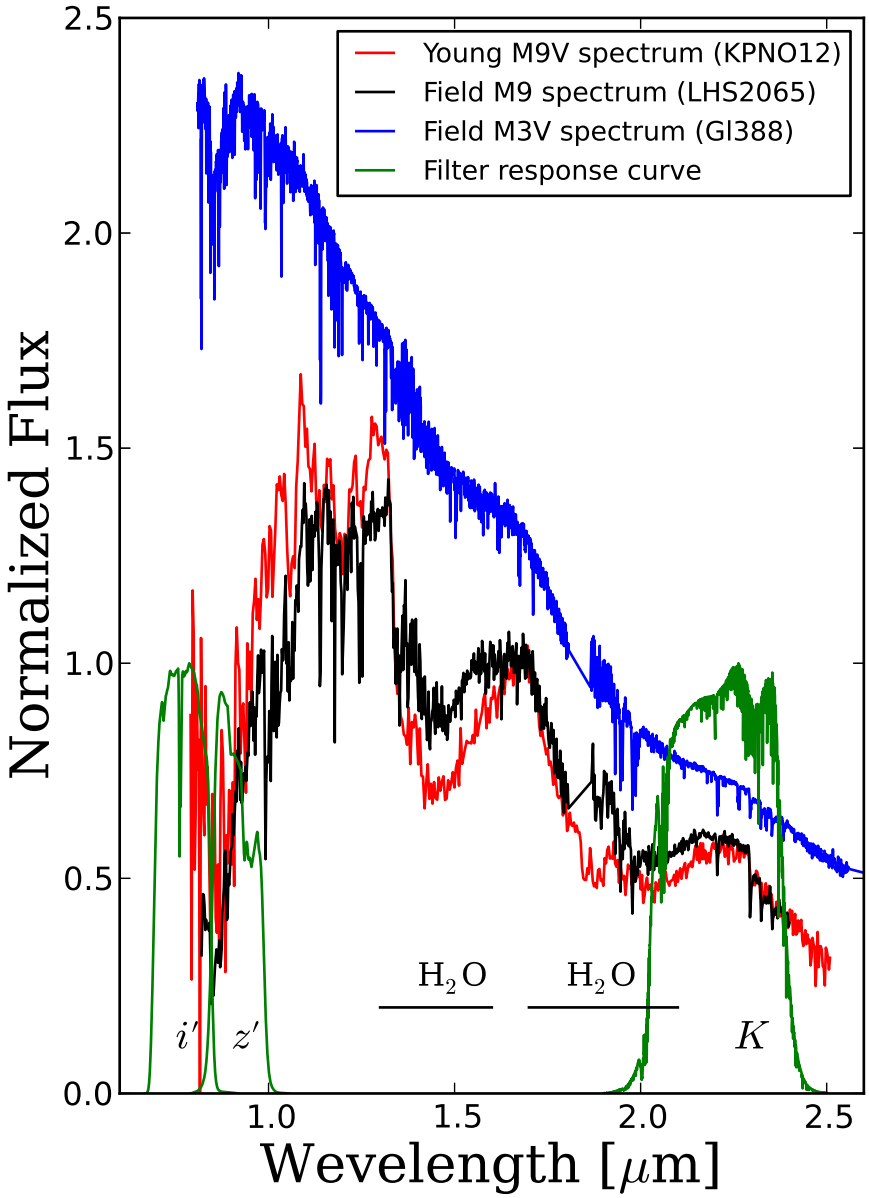

Figure 1.3: Comparison of a spectrum of a young M9-type BD spectrum (red: KPNO12; Muench et al., 2007) with that of a field M9-type dwarf with much higher gravity (black: LHS2065; Rayner et al., 2009). In addition, a spectrum of the field M3-type dwarf (blue: Gl388; Rayner et al., 2009) is shown. The spectra are available at the SpeX Prism Spectral Libraries[a]. The filter response curves used in our imaging data (Suprime-Cam i'- and z'-band; UKIDSS K-band) are shown at the bottom of this figure. As clearly shown in this figure, hotter objects like M3-type dwarfs have "bluer colors" in i'–z' or i'–K color, while the cool late-type objects have redder colors. **These clear differences in i'–z' or i'–K color diagrams (i.e., use of "optical" wavelength) provides a great benefit in efficiently removing the hotter objects, while preserving the cooler objects like PMOs.**

Chapter 2

Spectroscopy of Very Low Mass Brown Dwarfs in Orion Nebular Cluster

(Based on a paper by Suenaga et al., accepted for publication in PASJ)

In order to investigate the formation of substellar mass objects in the ONC, we obtained near-infrared spectra of BD candidates through two observing programs. The first data set was acquired on November 30, 2007, using the Multi-Object InfraRed Camera and Spectrograph (MOIRCS; Suzuki et al. 2008) mounted on the 8.2-m Subaru telescope (f/12.2 at the Cassegrain focus). The second data set was obtained during December 3–7, 2010, using ISLE (Yanagisawa et al., 2006, 2008), a near-infrared imager and spectrograph for the Cassegrain focus (f/18) of the 1.88-m telescope at OAO. Unfortunately, we could only observe relatively bright candidates because auto-guider problems and high-humidity conditions prevented a full observing program with MOIRCS. Therefore, we focus on the good signal-to-noise ratio (S/N) candidates for MOIRCS in this paper. In total, 12 BD candidates were selected, with eight of these objects obtained by MOIRCS and four obtained by ISLE (Table 2.1).

2.1 Observation and Data

2.1.1 Target Selection

The target sources for the spectroscopy were selected from the catalogue of Lucas et al. (2005), which presents the *JHK* photometry of the BD candidates obtained by Gemini-South/Flamingos. The selection criteria were as follows. (1) All sources have prospective masses ranging from the hydrogen-burning limit ($< 0.075\ M_{\odot}$) down to the deuterium-burning limit of $0.013 M_{\odot}$. (2) Sources that were close to or embedded in bright nebulosity were avoided. For optimum sensitivity, objects located in areas of faint nebulosity were chosen (Figure 1 in Lucas et al. (2005)). (3) Sources were only chosen if they exhibited fairly low visual absorption ($A_V < 7.5$), which is the same value as the recent spectroscopic study (Weights et al., 2009).

Since Lucas et al. (2005) suggested that there is a significant number of background stars with $A_V > 10$ and $K > 16$ among the BD candidates, the $A_V < 7.5$ limit reduces the background contamination. From 396 sources provided by Lucas et al. (2005), we selected 137 BD candidates within a extinction value $A_V < 4$, and observed 12 objects which include some previous observed objects. Although most of these objects have uncertainties ($\sim$ 0.1 mag) in their magnitude, two of them,208-736 and 215-652, have large errors ($>$ 0.2 mag) in their J and H magnitudes. Robberto et al. (2010) also observed these objects with ISPI, the facility infrared camera at the CTIO Blanco 4-m telescope, and achieved better quality for 208-736 in the H-band, and 215-652 in the J- and H-bands. Therefore, in our study we used the magnitudes of Robberto et al. (2010) instead of Lucas et al. (2005) for these objects: $H = 17.37 \pm 0.10$ for 208-736 and $J = 17.87 \pm 0.17$, $H = 17.23 \pm 0.09$ for 215-652.

2.1.2 Multi-Object Spectroscopy

We obtained eight spectra using Subaru/MOIRCS whose $4' \times 7'$ FOV is covered by two HAWAII 2048×2048 HgCdTe arrays with a pixel scale of 0.117 arcsec/pixel. We took simultaneous spectra of eight of the BD candidates using the multi-object spectroscopy (MOS) mode of MOIRCS. We used a 1-arcsec slit width and the $HK500$ grism, optimized for 1.4–2.5 μm and low-resolution ($R \sim 500$) spectra. To eliminate the background noise, the objects were observed with slit nodding. Dome flats were obtained before a run. In order to calibrate telluric absorptions, we observed a standard star with an F-type spectrum (HD7386) in a similar air mass as the main observations for the BDs.

2.1.3 Long-Slit Spectroscopy

Four spectra out of the 12 BD candidates were taken by OAO/ISLE. The detector was a HAWAII 1024×1024 HgCdTe array that covered a $4.3' \times 4.3'$ FOV with a pixel scale of 0.25 arcsec/pixel. The ISLE observations were carried out in the long-slit mode. The slit width was 1 arcsec and nod dithering was performed. A low resolution mode was selected with $R \sim 350$ in the H-band and $R \sim 450$ in the K-band. The observations on Dec. 3 and Dec. 4 were photometric. The Dec. 7 observation, 065-207, was taken under a condition of thin clouds, and we carefully analyzed this source to reduce the effect of this condition. We employed a 1.5-arcsec slit width to obtain sufficient S/N. We obtained the dome flat before and after the observation. We selected an F-type star, HD24635, and a B-type star, HD34748, to measure the telluric absorption. When using a B-type star possessing primarily strong hydrogen recombination lines as a telluric standard star, we must carefully deal with the stellar intrinsic lines since such lines cause artificial features in the spectra. Therefore, we removed the intrinsic lines in the B-type stellar spectra by interpolating it with the nearby flux.

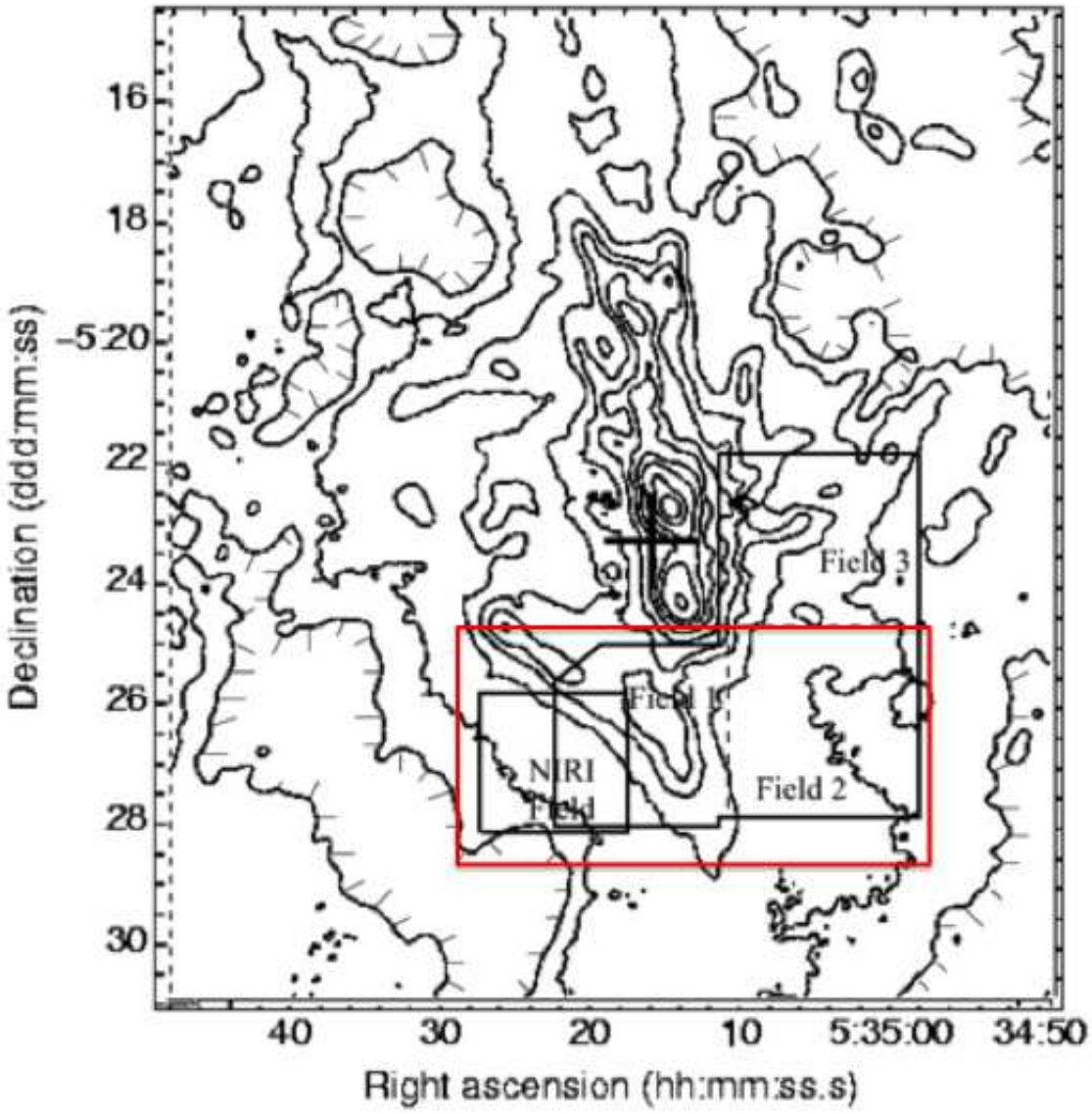

Figure 2.1: Our FOV overlaid with the dust continuum image (Figure 1 of Lucas et al., 2005). The field that we obtained for the spectra of BD candidates is shown as a red square box. The survey region of Lucas et al. (2005) is enclosed by solid lines and the locations of the three Gemini South/Flamingos fields are indicated. The location of θ_1 Ori C at the cluster center is indicated by a large + sign. The zero-flux contour is marked with short lines. Contour levels (in data numbers) are 0, 0.2, 1, 2, 3, 5, 8, 12, 20, 50 and 100. The 0.2 contour level corresponds to visual extinction of the order of $A_V = 5$.

Table 2.1: Summary of observed objects

Object	Data Set	J [mag]	H [mag]	K [mag]	A_V	Obs time H,K[min]	Reference[a]	ID(LRT05)[b]
030-524	MOIRCS	17.88	17.26	16.77	1.8 ±1.5	60,60	1,2	178
037-628	MOIRCS	18.52	17.66	16.99	4.4 ±1.5	60,60	2	94
061-400	MOIRCS	18.31	17.33	16.48	5.7 ±1.5	60,60	2	270
065-207	ISLE	13.47	12.81	12.24	$0.8\ ^{+1.5}_{-0.8}$	10,60	-	382
072-638	ISLE	15.39	14.80	14.29	$1.0\ ^{+1.5}_{-1.0}$	10,-	1	70
099-411	MOIRCS	17.08	16.40	15.99	2.3 ±1.5	60,60	-	256
104-451	ISLE	15.10	13.99	13.13	5.8 ±1.5	5,30	-	230
183-729	MOIRCS	18.05	17.38	17.24	2.3 ±1.5	60,60	1,2	18
208-736	MOIRCS	18.28[c]	17.37[d]	16.56	5.0 ±2.4	60,60	-	8
215-652	MOIRCS	17.87[d]	17.23[d]	17.15	2.0 ±2.0	60,60	-	56
216-540	MOIRCS	16.95	15.89	15.47	3.7 ±1.5	60,60	-	155
217-653	ISLE	14.99	14.26	13.32	2.4 ±1.5	5,30	1	55

Note. Object names are coordinate based, following O'dell & Wong (1996). 030-524 means that the coordinate of the object is (R.A., Decl.) = (05:35:03.0, -05:25:24). *JHK* magnitudes are taken from Lucas et al. (2005) with the exception of 208-736 and 215-652. Visual absorption (A_V) is estimated from a comparison between observed and synthetic J–H vs. H color-magnitude diagrams.

[a] The previous spectroscopic studies. 1. Riddick et al. (2007); 2. Weights et al. (2009)

[b] The running number is used in Lucas et al. (2005)

[c] The magnitude has a large uncertainty (> 0.2 mag)

[d] The magnitude is taken from Robberto et al. (2010) instead of Lucas et al. (2005)

2.2 Data Reduction

Both the multiple and long slit data were reduced using IRAF software. Standard techniques were used to reduce the MOIRCS multiple slit data. To subtract the sky background, the exposures for each BD candidate pair were separated into their relative nod positions (A or B). We subtracted the adjacent B frame from the A frame to reduce the residual. Flat fielding was corrected by using the dome flat frames. Note that channel 1 of MOIRCS was an engineering detector from Oct. 2007 to Jun. 2008 and had prominent, large, ring-like high dark noise. Therefore, we masked and did not use these regions in this data reduction. Cosmic ray cleaning was performed by L.A.Cosmic (Laplacian Cosmic Ray Identification; van Dokkum 2001). The array distortion was corrected by the MCSGEOCORR task in the MCSRED[a]. To calibrate the wavelength of the data, OH lines were identified as a function of wavelength. After performing 5-pixel binning along the wavelength directions of the data to improve the S/N ratio, we extracted the spectra with the APALL task in IRAF. We corrected spectral contamination due to telluric absorption using the standard star measurements. Extracted pairs from each nod position were combined. Finally, a dereddening procedure was conducted with an adopted reddening parameter of 3.1. We used the J–H vs. H color and magnitude of the objects and synthetic color-magnitude diagram (Allard et al., 2010) with age $\sim$ 1 Myr and distance $\sim$ 450 pc to derive the A_V values using the reddening law of Cardelli et al. (1989).

For the ISLE spectra, the reduction process was similar to that of MOIRCS. However, we did not correct the array distortion because the influence of the distortion was negligible. We obtained the H-band and K-band spectra separately. Therefore, the H-band and K-band spectra were scaled to the 2MASS magnitude of objects whose Vega magnitude and zero point magnitude were based on Cohen et al. (2003). The advantages of using 2MASS magnitudes are that the 2MASS magnitudes of our objects had low errors (< 0.1 mag) and the 2MASS Ks-band filter reduced the noise contribution from the thermal background beyond 2.3 μm.

2.2.1 Semi-Automatic Reduction Pipeline

In order to efficiently analyze the many spectra obtained from MOIRCS, we developed a semi-automatic reduction pipeline in the programming language CL-Script, with some procedures taken from external libraries. It is a simple pipeline for the standard reduction procedure. Using this pipeline, we can easily conduct each reduction step, though some manual operations are required. In particular, it is efficient to use a function to divide the 2-D MOS image into several 2-D spectral images. Also, optimization of background subtraction will minimize residual noise. We introduce the procedures briefly as follows:

1. Split the raw frame list. Before starting the data reduction, we need to split the raw frame list into objects, flat, comparison lists at each channel.

2. Subtract sky background (OH lines) optimally, perform flat field correction and correct for cosmic rays. When the sky background of a frame is subtracted, the reference frame for the subtraction is optimized to minimize the residual OH lines by combining the vicinity frames and multiplying the

[a]MCSRED was provided by Dr. Ichi Tanaka. See `http://www.naoj.org/staff/ichi/MCSRED/mcsred.html` for the software for MOIRCS imaging.

coefficient. In this procedure, the OH lines for minimizing the residual need to be selected manually. Next, flat fielding is conducted based on the split lists. The routine for cleaning cosmic rays provided from L.A.Cosmic is included in this pipeline.

3. Correct the array distortion. This routine is provided from the MCSGEOCORR task in the MCSRED.

4. Divide the 2-D MOS image into images. Before extracting the 1-D spectra, the 2-D MOS image needs to be divided into 2-D spectral images. This procedure needs an MDP file which is created during the preparations for observation to identify the position of each 2-D spectral image.

5. Wavelength correction and extraction of 1-D spectra. This procedure identifies OH lines for wavelength correction manually. Since the pipeline includes a detailed reference OH line list for MOIRCS, we need to identify at least three lines. The function for extracting 1-D spectra is included by using the APALL task in IRAF.

6. Combining frames, binning, correct telluric absorption and dereddening. After combining frames, binning, telluric correction and dereddening are optionally conducted.

2.3 Analysis

To derive the effective temperature and surface gravity, we compare our observed spectra to a grid of synthetic spectra and find the best-fit model in the χ^2 sense (e.g., Mohanty et al., 2007). First, we obtain the best-fit parameters (§2.3.2). We then conduct a Monte Carlo simulation to constrain the error range of the parameter estimates (§2.3.2) (e.g., Cushing et al., 2008; Bowler et al., 2009; Aller et al., 2013). We restrict the range of the stellar parameters in the fit to effective temperatures of 1800 K $\leq T_{\rm eff} \leq$ 4900 K and surface gravity 3.0 $\leq \log(g) \leq$ 5.5. We use the solar metallicity as the average for the low-mass members in the ONC.

2.3.1 BT-Settl model

We use the BT-Settl model atmosphere (Allard et al., 2010), which is available via the Phoenix web simulator. Allard et al. (2010) updated the BT-Settl model, applying the revised solar abundances determined by Asplund et al. (2009), the latest H_2O line list (Barber et al., 2008), a cloud model based on condensation and sedimentation timescales by Rossow (1978), the supersaturation computed from pre-tabulated chemical equilibrium, and mixing from 2D radiation hydrodynamic simulations by Freytag et al. (2010).

BDs have an atmosphere including water vapor, which causes strong absorption in the infrared regime. Because young BDs found in Trapezium are still gravitationally contracting, they have lower surface gravities than field dwarfs. Collision induced H_2 absorption (H_2-CIA) over the near-infrared wavelength regime is pronounced in environments of strong surface gravity. Therefore, young BDs have a triangular *H*-band shape due to deep H_2O and weak H_2-CIA absorptions (Kirkpatrick et al., 2006).

2.3.2 $\chi^2 - fitting$

Procedure 1 – Determine best fitting parameters

In order to determine the best fitting parameters, we conduct χ^2-fitting between the observed and BT-Settl model spectra. The results are shown in columns 3 and 4 of Table 2.2. The parameter ranges of the effective temperature and surface gravity are 1800 K $\leq T_{\rm eff} \leq$ 4900 K and 3.0 $\leq \log(g) \leq$ 5.5. The range of the surface gravity is predicted from BT-Settl evolutional tracks for an age ranging from 1 Myr to 1 Gyr. Although the determinations of the metal content in the Orion region are controversial, we use the solar metallicity as the average for low-mass members in the ONC based on D'Orazi et al. (2009). We seek the best $T_{\rm eff}$ and $\log(g)$ to minimize the reduced χ^2 value:

$$\chi^2 = \frac{1}{N-2} \sum^{N} \left(\frac{C f_{\rm mod} - f_{\rm obs}}{\sigma_{\rm obs}} \right)^2 \tag{2.1}$$

where N is the bin number of the wavelength, $f_{\rm mod}$ is the flux of the model spectra, $f_{\rm obs}$ is the flux of the observed spectra and $\sigma_{\rm obs}$ is the error of the observed spectra. The error is derived from the standard deviation of four combined spectra. C is the scaling coefficient of $f_{\rm mod}$ with $f_{\rm obs}$ and is derived from $d\chi^2/dC = 0$ for

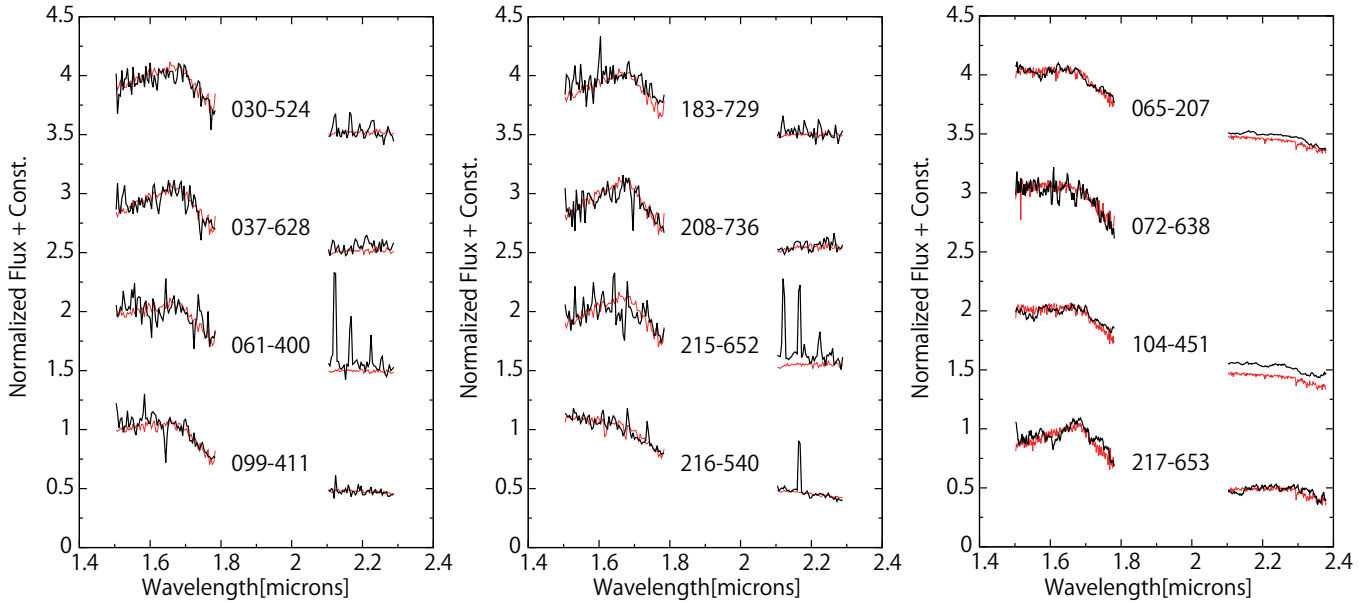

Figure 2.2: Near-infrared observed spectra. The left two panels show spectra obtained by MOIRCS and the right panel shows spectra obtained by ISLE. The observed (dereddened) spectra are shown by black solid lines while the best-fit model spectra are shown as red lines. The spectra of 061-400, 215-652 and 216-540 exhibit emission lines (H_2:2.12, 2.22μm; Brγ: 2.16μm).

Equation 2.1:

$$C = \frac{(\sum f_{\rm obs} f_{\rm mod}/\sigma_{\rm obs})^2}{\sum (f_{\rm mod}/\sigma_{\rm obs})^2}. \quad (2.2)$$

In order to minimize telluric contamination from water vapor, we restrict the regions for the fit to 1.50–1.78 μm and 2.10–2.29 μm in the case of MOIRCS, and 1.5–1.78 μm and 2.10–2.38 μm for the ISLE data. 061-400, 215-652 and 216-540 have emission lines in the *K*-band spectra (H_2: 2.12, 2.22 μm; Brγ: 2.16 μm), which degrades the χ^2 value when we include the *K*-band data in the fit. Therefore, we exclude the emission lines in the fitting process. Also, we can see spiky substructures in some *H*-band spectra. For example, there is a spiky bump around 1.7 μm in the spectrum of 208-736, which could be caused partly by a very low S/N ($\sim 1\sigma$). Such substructures affected by poor S/N worsen the χ^2 value. When both *H* and *K* spectra exist, we perform χ^2-fitting for two cases: using only the *H*-band and using both the *H*- and *K*-bands.

After performing the fit, we adopted the best-fit parameters that minimized the χ^2 value. We show the selected wavelength (*H* or *HK*) giving the best fit in column 5 of Table 2.2. In most cases we used both the *H*- and *K*-bands to increase the number of sampling points. 065-207, 072-638 and 104-451 were exceptions, where we only used the *H*-band. We adopted the result of fitting only using the *H*-band for 072-638 due to a lack of a *K*-band spectrum. We employed the results of the *H*-band for 065-207 and 104-451 because, in the fitting using only the *H*-band, we found a systematic offset between the observed and synthetic *K*-band spectra. This offset may be explained by the *K*-band excess from a circumstellar structure. Since the excess due to the circumstellar structure is more apparent for longer wavelengths, we checked the L'-band data of the objects, as presented by Lada et al. (2004), who determined $L' = 11.69$ for 065-207 and $L' = 12.27$ for 104-451 using VLT/ISAAC This enabled us to derive the dereddened photometric colors $H–L' = 1.02$ and $H–L' = 0.99$ respectively. We then estimate the synthetic colors $H–L'$ with theoretical spectra fitting with the *H*-band for 065-207 and 104-451, and with the *H* and L' filter response curves, which gives $H–L' = 0.71$ (065-207) and $H–L' = 0.70$ (104-451). The photometric colors of these objects are sufficiently redder than the synthetic colors ($\Delta(H–L') > 0.3$), which is strong evidence of a circumstellar structure.

Procedure 2 – Estimate the uncertainty

We perform parametric bootstrapping by a Monte Carlo simulation to determine the $T_{\rm eff}$ distribution, allowing us to determine the error range of $T_{\rm eff}$. In the simulation, we conducted several χ^2 fittings between the model spectra and a randomly generated mock spectrum. Uncertainty arises in the parameter estimate from the χ^2 fitting due to both the S/N of the observed spectra and the uncertainty of the visual absorption (A_V) estimate. Therefore, we separately evaluated the impact of these uncertainties on the derived $T_{\rm eff}$. We show the values of $T_{\rm eff}$ and errors in column 6 of Table 2.2. The procedures for deriving these values are as follows:

(1) In order to conduct a χ^2 fit, we simulated a mock spectrum by adding artificial noise to the theoretical spectrum. The parameters of the theoretical spectrum were determined based on the values derived in §2.3.2 and described in column 3 or 4 of Table 2.2. For example, in the case of 030-524, we use a theoretical spectrum with $T_{\rm eff} = 2600$ K and $\log(g) = 3.0$. The artificial noise is randomly generated based on the error

of the observed spectrum, which means that we model the artificial noise at each wavelength as drawn from a Gaussian distribution with a standard deviation adjusted to the 1σ error of the observed spectrum at the corresponding wavelength.
(2) We determine the best-fit parameters for the mock spectrum using χ^2 fitting.
(3) We repeat 10,000 iterations of steps 1–2, generating a distribution of $T_{\rm eff}$. We fit a Gaussian function to the distribution of $T_{\rm eff}$ measured in step 2. The error range of $T_{\rm eff}$ should be treated carefully since it is affected by the S/N of the spectrum and the uncertainty of the visual absorption A_V. By taking into account the S/N of the spectrum, we adopt the 1σ confidence range of the Gaussian distribution as the error range $\Delta T_{\rm eff,S/N}$.
(4) To evaluate the impact of the uncertainty ΔA_V on the error range of $T_{\rm eff}$, we conduct χ^2 fitting using three different A_V: the average value A_V, the upper limit $A_V + \Delta A_V$ and the lower limit $A_V - \Delta A_V$. For example, in the case of 030-524, we use three spectra dereddened with $(A_V - \Delta A_V, A_V, A_V + \Delta A_V) = (0.3, 1.8, 3.3)$. For the three spectra, we conduct χ^2 fitting as described in §2.3.2 to determine the best fitting parameters.
(5) We obtain three effective temperatures: $T_{\rm eff}(A_V)$, $T_{\rm eff}(A_V + \Delta A_V)$ and $T_{\rm eff}(A_V - \Delta A_V)$. To describe the error affected by ΔA_V, we define the upper error value as $\Delta T_{\rm eff,A_V,+} \equiv T_{\rm eff}(A_V + \Delta A_V) - T_{\rm eff}(A_V)$ and the lower error value as $\Delta T_{\rm eff,A_V,-} \equiv T_{\rm eff}(A_V) - T_{\rm eff}(A_V - \Delta A_V)$.
(6) We choose the larger of $\Delta T_{\rm eff,S/N}$ and $\Delta T_{\rm eff,A_V,\pm}$ as our $T_{\rm eff}$ uncertainty. In most cases, our error is dominated by the uncertainty in A_V.

Results

The obtained spectra and best-fit theoretical spectra from §2.3.2 are shown in Figure 2.2, and the estimated physical parameters are shown in Table 2.2. Most objects are well reproduced by the BT-Settl models. However, 216-540 required a change to the extinction value $\Delta A_V \sim 2$ to obtain better χ^2 values, which results in $T_{\rm eff} = 3320^{+760}_{-270}$ K.

Although some objects have slightly higher $T_{\rm eff}$ than those estimated by the previous works, namely 037-628 and 188-739, our result is largely consistent with those of previous works (Riddick et al., 2007; Weights et al., 2009). Note however that $T_{\rm eff} = 2750^{+250}_{-170}$ K of 061-400 is much higher than the previous result $T_{\rm eff} \leq 2400$ K (Weights et al., 2009). In Weights et al. (2009), the photometry and spectroscopy for this object were originally based on Lucas et al. (2001), in which they adopted $J = 18.250$ and $H = 17.706$. Adopting the same magnitudes, we obtain $A_V = 0$, which is lower than the adopted value $A_V = 5.7$ in this work, and the lower A_V results in a lower temperature. However, Robberto et al. (2010) provided a magnitude of $J = 18.35 \pm 0.20$ mag and $H = 17.46 \pm 0.10$ mag. Our adopted magnitudes are consistent with these more recent values. Thus, we use our result for 061-400 in the following discussions.

2.4 Discussion

Our observations have identified new very-low-mass objects in the ONC. Here we plot $T_{\rm eff}$ and absolute H magnitude on a synthetic HR diagram. We have discovered three new young BD candidates: 099-411 is an object with a boundary mass between stellar and substellar mass, 215-652 is a BD candidate with emission lines associated with youth, and 208-736 is a very low mass object which is even a BD/planetary-mass object . In this section we discuss the properties of each object based on the HR diagram, and then derive a number ratio for the stellar to substellar mass objects and discuss the star formation process in the outer region of the ONC.

2.4.1 HR diagram

We estimate the masses of the BD candidates by plotting the effective temperature and the absolute H magnitude on an HR diagram overlaid with theoretical isochrones (Figure 2.3). The error range of the mass corresponds with the error of the effective temperature in the HR diagram. We show the derived masses and the errors in Table 2.2. To convert the apparent magnitudes to absolute magnitudes, we use 450 pc (DM = 8.26) as the ONC distance. This value is the average distance determined in a previous investigation (Muench et al., 2008). The error of the distance is at most 50 pc (DM = 0.25), but the error is not significant compared with the error of the effective temperature in deriving the mass.

In Figure 2.3, it appears that there are several old objects ($\sim$ 10 Myr) even though the ONC is a very young cluster, $\leq$ 1Myr (Hillenbrand, 1997). We consider several scenarios to explain the old population. The first is that we are seeing contamination from another foreground population. It is known that the ONC is neighbored by several groups of stars. Alves & Bouy (2012) have investigated the surrounding populations of the ONC, and reported a contiguous population NGC 1980 which significantly overlaps the ONC. Since they have shown that NGC 1980 can make up for more than 10–20% of the ONC population, the projection of the foreground population may generate the age dispersion. However, its members are thought to be only $\sim$ 4–5 Myr old and therefore cannot account for the 10 Myr population on the HR diagram. Secondly, we consider the case that the older objects are foreground Galactic field stars. In particular, it is standing that 030-524 and 216-540 are older than 10 Myr. Since the local number density peaks at M3-M4 (Cruz, 2008), such objects are often contaminated. In contrast, it is unlikely the contamination is due to fainter objects since the local number density steeply decreases for the later spectral type ($\geq$ M5), and dense background molecular clouds prohibit penetration of the light of very cool stars. To confirm how frequently field stars can contaminate our sample, we calculated the probability of the contamination in the spectral type range of our interest.

Of the 12 objects observed in our work, eight have 2400 K $< T <$ 3000 K, corresponding to M6 to M9 (Luhman et al., 2003b). We first estimated the number of contaminating field stars of spectral type M6 to M9. For this purpose, we adopted the same method as Caballero et al. (2008) with the FOV of MOIRCS $\sim 4' \times 7'$[b]. We conservatively adopted a magnitude range of $12 < H < 18$ to include the brightest magnitude $H = 12.8$ mag (065-207) and the faintest magnitude $H = 17.7$ mag (037-628) in our work. For the ONC,

[b]Since Caballero et al. (2008) did not provide information for the H-band, we use the J–H color from West et al. (2008).

we used $E_{B-V} \sim 0.32$ from Lee (1968). Based on this, the number of contaminating field stars was found to be 0.23.

We estimated the probability of contamination by using a Poisson distribution with a mean of 0.23. The probability of detecting at least one contaminant was 20.3%. This means that one field BD having a similar temperature to 030-524 is likely to be observed in our small field, and thus the number of contaminants is not significant for M6–M9 dwarfs. However, when M3–M5 dwarfs are included, the expected number of contaminants increases to 11.5, so the probability of early M contaminant with a similar temperature to 216-540 is quite high. Therefore, we cannot make a strong statement about the membership of the M3–M5 objects from the contaminant probability.

Next, we verify whether the objects which appear older in photometry have any evidence of youth. Since protostellar objects are still experiencing gravitational contraction, they have a low surface gravity. 030-524 has a clear triangular *H*-band spectrum, which is evidence of low gravity and therefore evidence that it is a protostar undergoing gravitational contraction. 216-540 shows a Brγ emission in the *K*-band, which is associated with the mass accretion process and is a common mass accretion tracer (Muzerolle et al., 1998). 061-400 and 215-652 also have an emission line in their *K*-band spectra, which means that these objects are mass accreting protostars. As has been noted, several objects have spectral features consistent with being young objects although they seem to be old on our HR diagram. One explanation for this discrepancy is that these objects are protostars with edge-on discs which scatter light from the central star and decrease its apparent magnitude. In fact, the HST/ACS study of Ricci et al. (2008) reported that 037-628, 061-400, 215-652 and 216-540 have ionized discs seen in emission. The existence of such objects has been indicated by previous surveys not only in the ONC (Slesnick et al., 2004) but also in other regions (e.g., Briceño et al., 2002b; Luhman et al., 2003b). For example, in two T Tauri systems HH30 and HK Tau C with edge-on circumstellar discs, the *K*-band magnitude is more than 3 mag lower than expected for their age, distance and spectral type (Burrows et al., 1996; Stapelfeldt et al., 1998). Consequently, the apparently older objects can be explained as being young stellar objects with edge-on discs. Also, the episodic accretion process may explain the low luminosity of the apparently older objects, even without them being edge-on discs (Baraffe et al., 2009). However, to confirm the validity of their membership, we need further evidence of youth. For example, we should investigate the infrared excess due to the circumstellar discs at longer wavelengths.

2.4.2 Stellar to substellar mass number ratio

Here, we derive the stellar to substellar mass number ratio *R*, which can give information on the possibility of differences in the formation process between stars and substellar objects (e.g., Luhman et al., 2003b; Andersen et al., 2008). In previous works, two definitions of *R* have been used:

$$R_1 = \frac{N(0.08 < M/M_\odot < 1)}{N(0.03 < M/M_\odot < 0.08)} \tag{2.3}$$

$$R_2 = \frac{N(0.08 < M/M_\odot < 10)}{N(0.02 < M/M_\odot < 0.08)} \tag{2.4}$$

In this paper, we derive *R* following the above definitions. We measure R_1 and R_2 according to the following steps. (1) We choose objects with $A_V < 7.5$ from Lucas et al. (2005), whose observation was conducted for

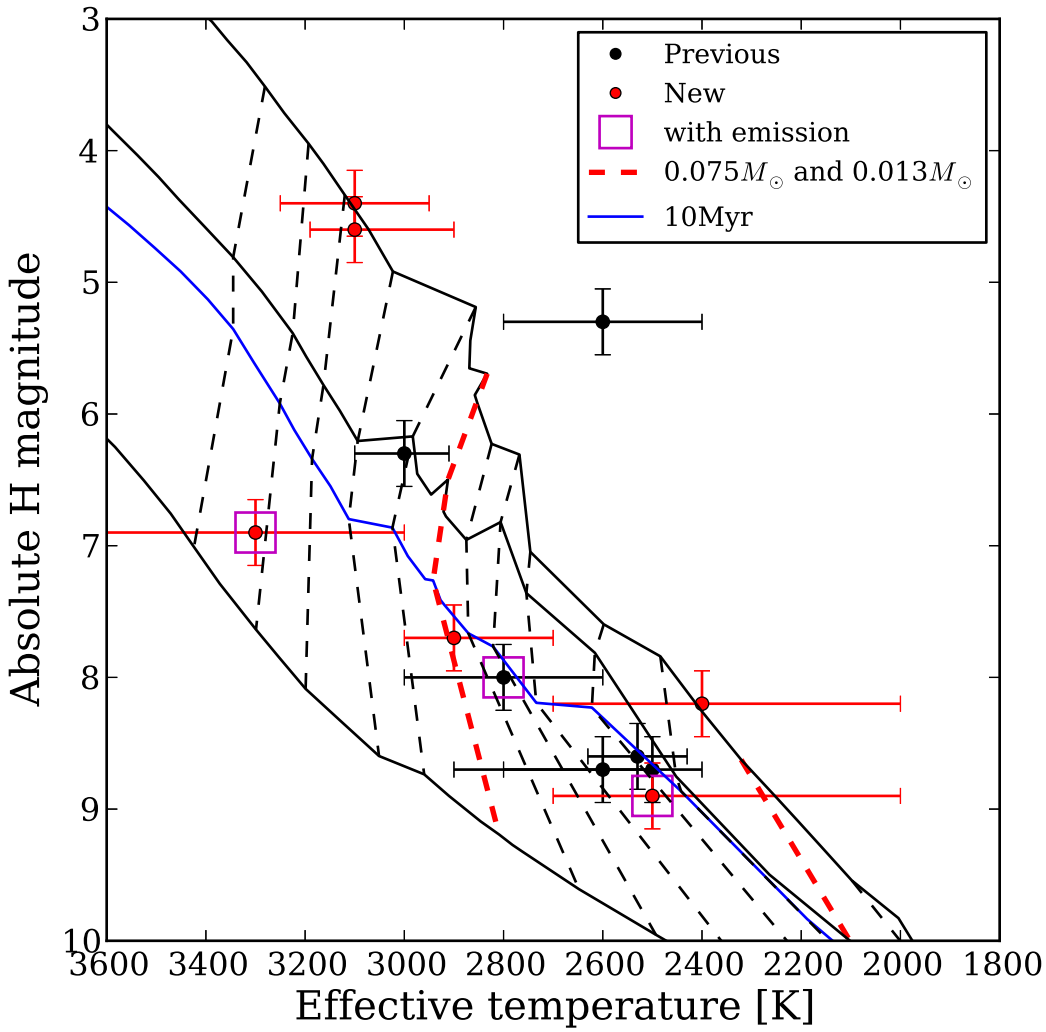

Figure 2.3: $T_{\rm eff}$ vs absolute H-band HR diagram for the 12 objects in our spectroscopic sample. The lines indicate the synthetic HR diagram (BT-Settl; Allard et al., 2010). The solid lines show the age isochrones 1, 5, 10, 100 Myr from top to bottom. The dashed lines show the mass isochrones 0.007, 0.013, 0.02, 0.03, 0.04, 0.05, 0.06, 0.075, 0.1, 0.11, 0.15, 0.2, 0.3 $M_\odot$ from right to left (the red dashed lines indicate 0.013 and 0.075 $M_\odot$). The red dots indicate newly observed objects and the black dots indicate follow-up objects from previous works (Riddick et al., 2007; Weights et al., 2009). The magenta squares represent objects with emission lines.

Table 2.2: The result of χ^2-fitting

		H[b]		HK[b]					Reference	Reference
Name	M_H[a]	$T_{\rm eff}$	log(g)	χ^2	$T_{\rm eff}$	log(g)	χ^2	Fit[c]	$T_{\rm eff}$ [K][d]	Mass [$M_\odot$][e]	SpT[f]	$T_{\rm eff}$ [K][g]
030-524	8.7	3000	3.0	0.9	2600	3.0	2.1	*HK*	2600^{+300}_{-100}	$0.037^{+0.049}_{-0.015}$	M8.0±0.75	2710^{+127}_{-233}
037-628	8.6	2700	3.5	1.7	2500	3.0	1.7	*HK*	2500^{+100}_{-100}	$0.022^{+0.006}_{-0.005}$	>M9.5	< 2400
061-400	8.0	3400	3.0	1.8	2800	3.5	3.0	*HK*	2800^{+200}_{-200}	$0.046^{+0.056}_{-0.018}$	>M9.5	< 2400
065-207	4.4	3100	4.5	0.3	2900	4.0	1.0	*H*	3100^{+150}_{-150}	$0.145^{+0.97}_{-0.039}$	-	-
072-638	6.3	3000	5.5	0.9	-	-	-	*H*	3000^{+100}_{-90}	$0.097^{+0.018}_{-0.019}$	M6.5±0.5	2935±55
099-411	7.7	2900	4.5	4.8	2900	4.5	3.1	*HK*	2900^{+100}_{-200}	$0.062^{+0.030}_{-0.026}$	-	-
104-451	4.6	3100	4.0	1.0	2500	3.0	2.8	*H*	3100^{+90}_{-200}	$0.134^{+0.078}_{-0.031}$	-	-
183-729	8.7	2800	3.0	1.9	2500	3.0	2.0	*HK*	2500^{+300}_{-100}	$0.022^{+0.035}_{-0.006}$	≥M9.5	< 2400
208-736	8.2	2500	3.0	1.4	2400	3.0	1.7	*HK*	2400^{+300}_{-400}	$0.016^{+0.022}_{-0.010}$	-	-
215-652	8.9	2900	3.5	2.8	2500	3.0	4.2	*HK*	2500^{+200}_{-500}	$0.022^{+0.027}_{-0.016}$	-	-
216-540	6.9	3300	5.0	3.8	3300	5.0	2.6	*HK*	3300^{+700}_{-300}	> 0.100	-	-
217-653	5.3	2900	3.0	2.3	2600	3.0	1.7	*HK*	2600^{+200}_{-200}	$0.031^{+0.028}_{-0.015}$	M7.75±0.5	2752^{+80}_{-120}

[a] Absolute M_H magnitudes.

[b] The values are derived from χ^2-fitting for seeking best fitting parameters (see §2.3.2). The $T_{\rm eff}$ and log(g) are used for simulating the mock spectrum (see §2.3.2).

[c] This column shows the wavelength used for determine best fitting parameters (see §2.3.2).

[d] The best $T_{\rm eff}$ and the uncertainty which is derived from the Monte Carlo simulation (see §2.3.2).

[e] Masses derived from the HR diagram (see §2.4.1 and Figure 2.3).

[f] The reference of spectral type (SpT) is shown in Table 2.1. When the object has been observed both in Riddick et al. (2007) and Weights et al. (2009), we use the SpT of Weights et al. (2009).

[g] These quantities were derived using the reference spectral type to effective temperature scale of Luhman et al. (2003b)

the 1.7′–5.7′ regions from the ONC center. The completeness limit for A_V is determined to be $A_V = 7.5$. (2) We consider that objects with spectroscopically known properties are fiducial samples for investigating R. However the sample which we spectroscopically observed is still insufficient for a statistical discussion. In order to increase the sample size, we compiled information on spectroscopic observations of the corresponding $A_V < 7.5$ sample from previous studies (Hillenbrand, 1997; Lucas et al., 2006; Riddick et al., 2007; Weights et al., 2009). Also, non-member stars are excluded from the sample based on previous studies. Hillenbrand (1997) conducted an optical imaging and spectroscopic survey of stellar mass objects in a large region of ONC, almost 80% complete down to 0.1 $M_\odot$. Lucas et al. (2006, infrared), Riddick et al. (2007, optical) and Weights et al. (2009, infrared) reported spectroscopic studies for the substellar mass candidates ($< 0.075\ M_\odot$) found by Lucas et al. (2001) and Lucas et al. (2005). (3) In order to avoid inconsistencies from different mass determinations, we recalculated the masses of individual samples using the HR diagram, as explained in §2.4.1, instead of using the masses derived in the previous papers. (4) We corrected for the bias due to sample incompleteness of the spectroscopic survey. As described above, Hillenbrand (1997) observed stellar mass objects, but the other studies concentrated on substellar mass objects. As a result, the spectroscopic completeness is 68% in the stellar mass regime and 58% in the substellar mass regimes as defined for the calculation of R_1. Also, the completeness is 72% in the stellar mass regime and 55% in the substellar mass regime used for R_2 . When we estimate the number ratio of the stellar to substellar mass, the bias of the completeness causes the number ratio to be overestimated. Therefore, in order to correct the bias, we added three hypothetical substellar objects to calculate R_1 and five hypothetical substellar objects to calculate R_2 according to the completeness of the stellar mass regime. Consequently, we determined $R_1 = 90/26 = 3.5 \pm 0.8$ and $R_2 = 110/34 = 3.2^{+0.7}_{-0.6}$ in 1.7′–5.7′ regions from the ONC center. The errors were estimated using the method of Scholz et al. (2012b), who used the confidence interval provided by Cameron (2011).

2.4.3 Sample completeness

In this section, we explore the possibility that we have incorrectly estimated the ratio of BDs to stars due to some bias.

A_V estimate — As discussed in §2.3.2, the uncertainty in A_V is estimated to have a high impact on the determination of physical parameters. We consider the uncertainty of the photometry, which has a relatively large impact ($\delta A_V \sim 1.5$ mag). As another error source, we calculate the impact of using a 10 Myr color isochrone instead of 1 Myr in determining A_V. As a result, we find that the mean difference inA_V between the 1 Myr and 10 Myr isochrone is 0.5 mag, which is insignificant in comparison with the impact of the photometric uncertainty.

Use of a limited A_V sample — We set a selection limit of $A_V < 7.5$ in the collecting sample. The A_V limit prohibits embedded massive objects from being counted disproportionally. In addition, the limit value $A_V < 7.5$ is the same as that used in previous works (Lucas et al., 2006; Riddick et al., 2007; Weights et al., 2009). Therefore, the use of an A_V limit has an insignificant bias on the sample selection.

Table 2.3: Star to substellar number ratio in the ONC

reference	R_1	R_2	r
This work	3.5[a] (2.7-4.3)	3.2[a] (2.6-3.9)	$1.7' < r < 5.7'$
Luhman et al. (2003b)	-	3.8	$r < 1.5'$
Slesnick et al. (2004)	3.3[b] (2.6-4.1)	5.0	$r < 2.5'$
Andersen et al. (2011) inner	7.2 (1.6-12.8)	-	$2.9' < r < 5.8'$
Andersen et al. (2011) cluster	2.4 (2.2-2.6)	-	$2.9' < r < 12.5'$

[a] The error range is estimated in the same manner as Scholz et al. (2012b).
[b] Andersen et al. (2008) have compiled the study of Slesnick et al. (2004) and shown this value.

Distribution bias of spectroscopic sample —- Some authors have suggested that the distributions in the ONC between stellar and substellar objects could be different. Therefore, if our spectroscopic sample has a bias in the distribution in the ONC, the ratio of substellar to stellar objects may be wrongly estimated. Since all of our sample is selected from the field observed by Lucas et al. (2005), we can check the distribution of our sample and have found no bias in it. Therefore, the observations in our work and previously published works have included no bias with respect to objects' positions.

Spectroscopic completeness — As discussed in §2.4.2, since the spectroscopic completeness of our sample is lower in the substellar mass regime than in the stellar mass regime, we have corrected the bias by adding some hypothetical substellar objects. This method is similar to that employed in (Slesnick et al., 2004)

2.4.4 Implications on the star formation in the ONC: Comparison of the measured number ratio with other studies

Scholz et al. (2012b) listed R values for various star forming regions. In comparison with the other star forming regions, our derived R_1 and R_2 are the second lowest values, which means that the number ratio of substellar mass objects in the ONC is relatively high compared with the other star forming regions. In the ONC, R has been investigated from the center to the outer edge. Andersen et al. (2011) have discontinuously covered a large area ($26' \times 33'$) using HST/NICMOS Camera 3. Over the whole observed area, they found $R_1 = 2.4 \pm 0.2$, which is a small value and suggests a flat IMF in the substellar mass regime. $R_1(\mathrm{Andersen}, \mathit{cluster})$ is lower than our derived $R_1(\mathrm{Suenaga}) = 3.5 \pm 0.8$, indicating that in a wide FOV the number of substellar objects is significantly high in the ONC. Da Rio et al. (2012) have also covered a large FOV ($32' \times 33'$) with a WFI camera mounted on the 2.2-m MPG/ESO telescope. They generated the IMF down to 0.02 $M_\odot$, which decreases steeply with decreasing mass. They found no evidence of IMF flattening toward the substellar mass regime. The inconsistency between Andersen et al. (2011) and Da Rio et al. (2012) may be explained by different estimates of background contamination. To confirm the validity of these studies, it is necessary to extend the coverage area of our spectroscopic study with multi-object spectrographs.

Considering the inner regions ($r < 2.5'$) of the ONC, Luhman et al. (2003b) have measured $R_2 = 3.8$. The properties of brighter objects ($K < 12$) in their sample were taken from K-band spectroscopy, however the fainter substellar objects were mostly based on photometric data with HST/NICMOS camera 3 (Luhman et al., 2000). On the other hand, the inner regions were spectroscopically investigated by Slesnick et al. (2004), who found R_2(Slesnick) = 5.0. Andersen et al. (2008) have compiled the study of Slesnick et al. (2004), and found R_1(Slesnick) = $3.3^{+0.8}_{-0.7}$ in this region. Our derived R_1(Suenaga) = 3.5 ± 0.8 is consistent with the value R_1(Slesnick), but R_2(Suenaga) = $3.2^{+0.7}_{-0.6}$ is lower than R_2(Slesnick). Since our observations focus on the outer regions of the ONC, in contrast with Slesnick et al. (2004), the central concentration of the high mass population ($> 1M_{\odot}$) found by Hillenbrand & Hartmann (1998) may explain the difference in measured R_2 values.

The outer regions ($2.9' < r < 12.5'$) were observed by Andersen et al. (2011). They reported that although it has a large error, $R_1(\mathrm{Andersen}, \mathit{inner}) = 7.2 \pm 5.6$ in the 2.9′–5.8′ area is consistent with the value R_1(Slesnick) of the inner part ($r < 2.5'$). In addition, Andersen et al. (2011) found that the number ratio R decreases as a function of radius. Our result suggests that R_1(Suenaga) = 3.5 ± 0.8 of the outer part ($1.7' < r < 5.7'$) is consistent with the R_1(Slesnick) of the inner area of the ONC ($r < 2.5'$). This result suggests that the cluster distribution does not decrease simply as a function of radius.

Our results imply that the substellar IMF is universal within 0.6 pc of the ONC. As a substellar formation scenario, the photo-evaporation of OB stars has been suggested and the effect might be dominant in the vicinity of OB stars (Kroupa & Bouvier, 2003; Whitworth & Zinnecker, 2004). For example, considering the photo-ionization of a O6 star (θ^1 Ori C) in the center of the ONC, a protostar initially with a mass of 0.3 $M_{\odot}$ and within a radius of 1 pc from the O star is reduced to one with a mass of 0.08 $M_{\odot}$ (Kroupa & Bouvier, 2003). Therefore, if this scenario was dominant for the substellar formation, we would find the different fraction of BDs to stellar populations between the central and outer regions of the ONC. However, based on our and previous spectroscopic samples, the universal IMF of the substellar regime implies that the scenario is unimportant in the ONC. Note that we cannot reject this formation scenario in the whole star formation. For very massive clusters (stellar superclusters), which may contain many stars with masses reaching to 150 $M_{\odot}$, the radius for producing photo-evaporated BDs from low-mass protostars may be similar to the radius of the whole cluster. Globular cluster may thus have a significant population of photo-evaporated BDs.

To be summarized, we conducted a spectroscopic survey program in the Orion Nebular Cluster using MOIRCS mounted on the Subaru telescope and ISLE mounted on the Okayama 1.88m telescope. We present 12 near infrared spectra of BD candidates. We newly identify two BD candidates, and a BD/planetary boundary mass object. We find that several young stellar candidates appear older in the HR-diagram. The faintness can be explained by the light scattering from the central star due to the circumstellar structure, or the episodic accretion. Our aims to observe the ONC are to confirm the universality of the substellar IMF in the ONC and the impact of OB star's photo-evaporation process on the substellar formation. Based on the spectroscopic data, we first show that the substellar IMF in the outer region ($r < 6'$) is consistent with the central one. In addition, we suggest that the impact of OB star's photo-evaporation process on the substellar formation is unimportant in the ONC since the substellar IMF is universal around the central OB stars.

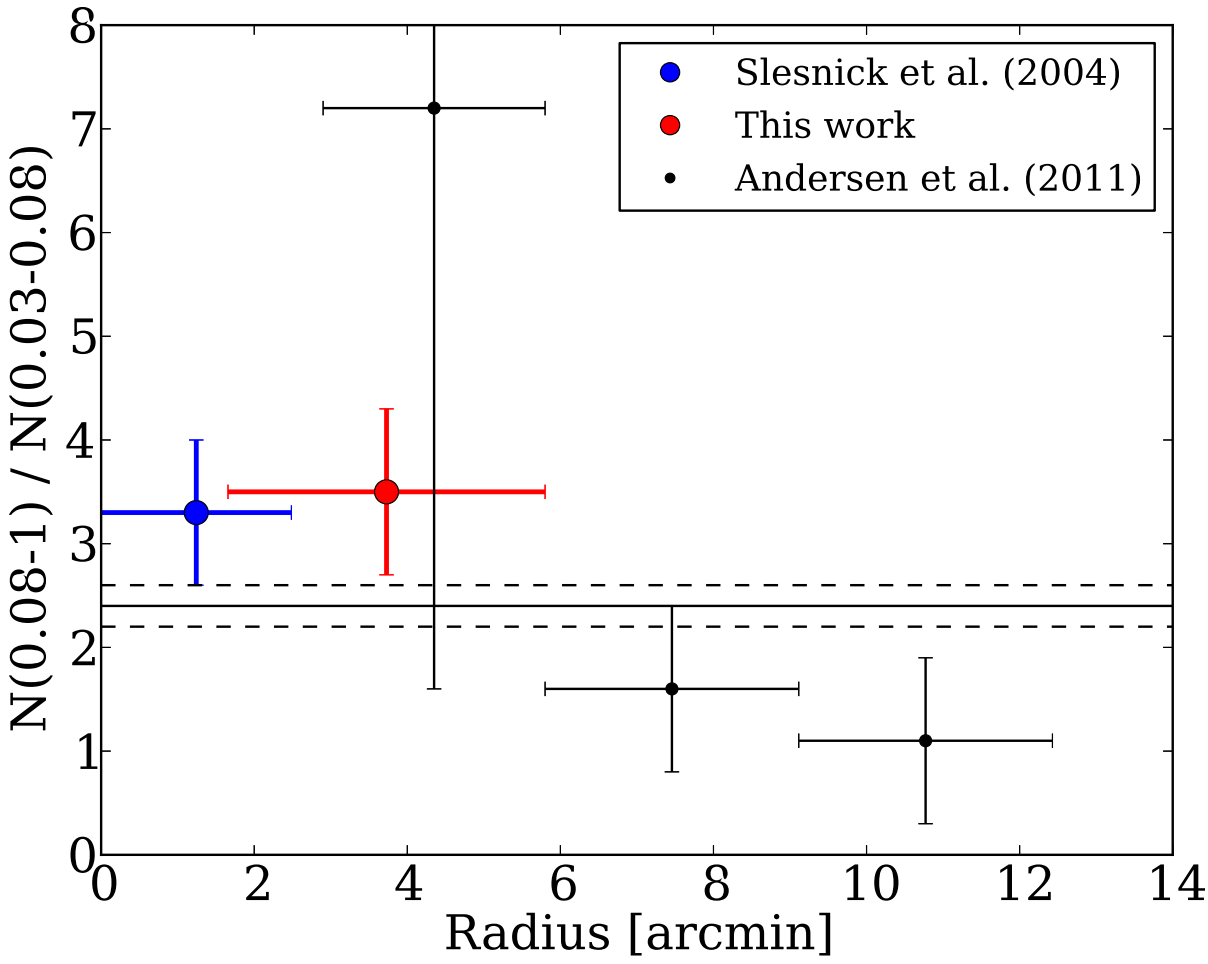

Figure 2.4: Ratio of low-mass stars (0.08–1.0 $M_{\odot}$) to BDs (0.03–0.08 $M_{\odot}$) for the ONC as a function of radius. The blue dot with error bars indicates the spectroscopic result of (Slesnick et al., 2004) and the red dot indicates our result. The black dots represent the photometric result of Andersen et al. (2011) and the horizontal line is the average ratio of the cluster, with the dashed lines showing the 1σ error interval (Andersen et al., 2011).

Chapter 3

Searching for Planetary Mass Objects in the Taurus Molecular Cloud

The TMC is a nearby, young star forming region. Therefore, it is one of the best places to investigate the population of PMOs. In order to find PMOs in the TMC, we conducted optical and infrared imaging with Subaru/Suprime-Cam and OAO/ISLE. We combined the imaging catalogue with other infrared photometry data sources , UKIDSS/GCS, UKIDSS/GPS, *Spitzer* and *WISE*. From several color selection criteria and proper motion analysis, we selected several PMO candidates and obtained three spectra from these candidates using Subaru/IRCS.

3.1 Observation and Data

3.1.1 Optical Imaging

In order to search for faint PMOs in the widely spread TMC, an instrument with high sensitivity and wide FOV is essential. The Suprime-Cam, on the Subaru Telescope, consists of 5×2 arrays of 2048×4096 CCD detectors and provides a FOV of $34' \times 27'$ with a pixel scale of $0.202''$ (Miyazaki et al., 2002). The Suprime-Cam is the best instrument for studying a wide area of TMC and can achieve a sensitivity down to a few $M_{\rm Jup}$.

We observed the TMC during November 20–21 in 2009. We used two optical band filters, i' and z' which enabled us to separate cool late-type stars from early-type stars by combining infrared data. In order to reduce the influence of bad pixels and cosmic rays, each frame was observed with telescope dithering. Before and after each run, we obtained the sky flat frames of blank fields. The observation was conducted under good conditions (seeing $< 1.0''$), except for the TAUII1 region, which was obtained at low air mass (~ 2.0). Also, we could not observe the TAUV3 and TAUV4 regions in the i'-band since the weather turned cloudy at the end of the Nov. 21 run. It is difficult to cover the entire region of the widely spread TMC and we therefore focused on the high stellar density region, as described in Fig.3.1.1. It is known that the region includes many stars and BDs, and thus we can expect to find PMOs. We observed several photometric

Table 3.1: Summary of the Suprime-Cam observations

Field Name	R.A. (J2000) [hh:mm:ss.s]	Decl. (J2000) [dd:mm:ss]	Exp. Time [sec](i'/z')	Seeing [$''$](i'/z')	Obs. Date [2009.mm.dd] (i'/z')	Completeness [AB,mag] (i'/z')	GCS coverage (J/K) [%]
TAUII1	04:18:35.3	+28:23:01	700/850	1.4/1.2	11.20/11.20	24.3/23.5	32/100
TAUIII1	04:39:05.5	+26:06:51	2310/2025	1.0/0.7	11.20/11.20	25.7/25.1	100/14
TAUIII2	04:39:06.5	+25:35:37	2730/2025	1.0/0.8	11.20/11.20	25.7/24.9	100/65
TAUIII3	04:40:32.4	+25:36:00	2080/1980	1.0/0.7	11.20/11.21	25.9/24.6	100/57
TAUIII4	04:40:32.2	+26:07:35	2210/1440	1.0/0.7	11.20/11.21	25.5/24.5	100/0
TAUV1	04:33:26.0	+23:00:32	2400/1800	0.6/1.0	11.21/11.21	25.9/24.5	0/100
TAUV2	04:33:26.0	+22:34:08	1925/1980	0.4/0.8	11.21/11.21	25.3/24.1	100/100
TAUV3	04:35:19.7	+22:34:09	/1650	/0.7	/11.21	/24.7	0/100
TAUV4	04:35:19.7	+23:00:36	/1700	/0.7	/11.21	/24.7	0/100

standard stars at the same air mass as the science frames, which were selected by Smith et al. (2002).

3.1.2 Near-infrared Imaging

The color–magnitude and color–color diagram combining optical and infrared data is a useful tool for distinguishing young stellar objects from Galactic field stars. We used optical data obtained with Subaru/Suprime-Cam and infrared data from the UKIDSS/WFCAM Galactic Cluster Survey and Galactic Plane Survey. However, since the UKIDSS/GCS and GPS are ongoing projects, the infrared data did not completely cover our optical data. Therefore, we conducted near-infrared imaging of some planetary mass candidates selected based on Suprime-Cam optical data.

We observed several PMO candidates during November 29 to December 4 in 2012 and September 23 to 29 and December 2 to 4 in 2013. First, we used a *K*-band filter to follow up the PMO candidates which were not observed in both UKIDSS GCS and GPS, and thus were selected based only on optical data. Combining the *K*-band data and optical data, we selected probable PMO candidates, and then we observed the candidates with *J*- and *H*-band filters. Also, we observed an L-type candidate in Taurus (2M0437+2331) to estimate the proper motion, although this object was out of our Suprime-Cam field. In order to reduce the influence of bad pixels and cosmic rays, each frame was observed with telescope dithering.

3.1.3 UKIDSS Galactic Cluster Survey / Galactic Plane Survey

For combination with our deep optical data, we used a huge amount of near-infrared data from the UKIRT Infrared Deep Sky Survey (UKIDSS; Lawrence et al. 2007), gathered with WFCAM (Casali et al., 2007) on the 3.8-m UK Infrared Telescope (UKIRT) in Hawaii. WFCAM has four 2048×2048 Rockwell devices, at 94% spacing. The pixel scale of 0.4 arcsec gives an exposed solid angle of 0.21 sq. degrees. The UKIDSS

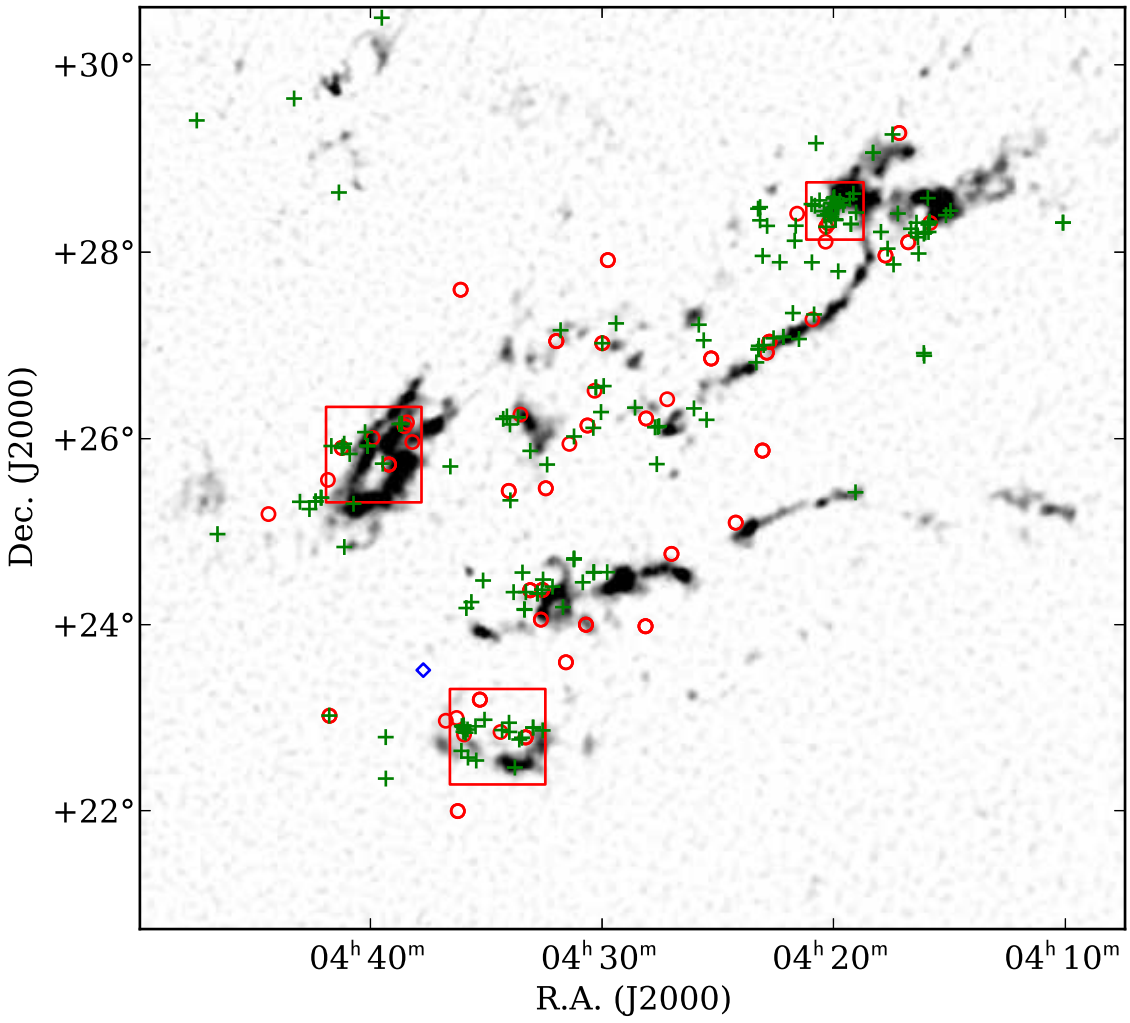

Figure 3.1: Our FOV in Taurus. The red square boxes represent our observational field, which focused on the high stellar density regions. The symbols indicate the known members in Taurus (Guieu et al., 2006; Luhman, 2006; Luhman et al., 2009, 2010; Kraus & Hillenbrand, 2007; Rebull et al., 2010, 2011), namely early type objects (SpT < M6; green crosses), late M type objects (SpT > M6; red circles) and 2MASSJ 04373705+2331080 (2M0437+2331), which is an L0 object reported in Luhman et al. (2009) (blue diamond). The background image is the visual extinction map (Dobashi, 2011).

Table 3.2: Summary of the ISLE observations

Object Name	R.A. (J2000) [hh:mm:ss.ss]	Decl (J2000) [dd:mm:ss.s]	Band	Exp. Time [min]	Obs. Date [yyyy.mm.dd]
tau1152	04:17:31.39	+28:16:21.6	*H*	90	2013.12.04
tau1907	04:17:49.18	+28:19:01.1	*H*	60	2013.09.23
tau2229	04:18:00.58	+28:25:48.6	*H*	28	2012.11.29
			J	36	2013.09.28
tau2370	04:18:05.65	+28:36:58.0	*J*	60	2012.11.29
			H	60	2012.11.29
			K	60	2012.11.29
tau4426	04:18:59.82	+28:24:12.4	*J*	60	2013.09.23
			H	60	2012.11.29
tau16696	04:32:40.28	+23:11:39.6	*K*	60	2012.12.04
tau17907	04:32:43.87	+23:13:12.5	*K*	60	2012.12.04
tau43800	04:33:51.72	+22:42:00.0	*J*	60	2013.09.28
tau49818	04:34:06.44	+23:17:33.0	*K*	60	2012.12.02
tau111618	04:38:07.47	+25:50:48.1	*K*	60	2012.12.04
tau113963	04:38:14.32	+26:05:45.9	*K*	30	2012.09.25
			K	60	2012.12.04
tau130655	04:39:14.62	+26:01:33.1	*H*	90	2013.09.24
tau136414	04:39:47.25	+26:17:32.9	*K*	60	2012.12.04
tau136525	04:39:48.10	+26:01:07.5	*J*	60	2013.09.28
tau136744	04:39:49.53	+26:09:14.7	*K*	60	2012.12.04
tau140677	04:40:14.41	+25:37:42.5	*H*	60	2013.09.23
tau145277	04:40:34.36	+26:04:34.2	*K*	10	2012.11.29
			K	60	2012.12.02
tau147881	04:40:46.67	+25:29:31.7	*H*	90	2013.12.04
tau151260	04:41:03.01	+25:29:40.6	*H*	90	2013.12.04
tau154866	04:41:20.59	+25:55:19.5	*H*	90	2013.09.24
2M0437+2331	04:37:37.05	+23:31:08.0	*K*	10	2013.12.02

is a set of five surveys and aims to study BDs, high-redshift dusty starburst galaxies, elliptical galaxies, galaxy clusters at redshifts $1 < z < 2$, and the highest-redshift quasars at $z = 7$.

The Galactic Cluster Survey (GCS) aims to cover ~ 1000 deg^2 in 10 star-forming regions and open clusters down to 0.03–0.01 $M_\odot$ to investigate the universality of the IMF. Each cluster is covered in $(Z, Y, J, H, K) = (20.4, 20.1, 19.6, 18.8, 18.2)$. We obtained data of observations of the TMC from the latest GCS data release (DR) to date, DR10 on January 14, 2013 through the WFCAM Science Archive (WSA; Hambly et al., 2008).

The Galactic Plane Survey (GPS; Lucas et al., 2008) is designed to cover the entire northern and equatorial Galactic plane that is accessible to UKIRT in a 10°-wide band around the sky. There is also a narrower southern extension to the Galactic Center and a 200 deg^2 survey of the Taurus–Auriga–Perseus molecular cloud complex. The 5σ depth is $(J, H, K) = (19.8, 19.0, 18.1)$ given by Warren et al. (2007) about DR2, whose depth is spatially variable. We use the latest GPS DR8 provided from February 17, 2012.

3.1.4 *Spitzer* and *WISE* Catalogue

The *Spitzer* catalogue data is referred to as the Taurus *Spitzer* Survey, and is described in Padgett et al. (2008). It covers ~ 44 deg^2 using the Infrared Array Camera (IRAC; 3.6, 4.5, 5.8, and 8μm; Fazio et al. 2004) and Multi-band Imaging Photometer (MIPS for *Spitzer*; 24, 70 and 160 μm; Rieke et al. 2004), and is a *Spitzer* Legacy Project. We obtained the catalogue data through the NASA/IPAC Infrared Science Archive.

WISE data acquisition and reduction are discussed in Wright et al. (2010) and Jarrett et al. (2012), and in the Explanatory Supplement to the *WISE* Preliminary Data Release Products. There are four *WISE* bands, with central wavelengths at 3.4, 4.6, 12 and 22 μm, and a spatial resolution of 6″ (12″ at 22 μm). The four bands are often referred to as W1, W2, W3 and W4. We obtain the data of *WISE* All-Sky Data Release (Cutri & et al., 2012) through the VizieR database (Ochsenbein et al., 2000)

3.1.5 Near-Infrared Low Resolution Spectroscopy

We selected PMO candidates from our photometry and observed three spectra out of these candidates. The spectra were obtained using Subaru/IRCS+AO188 which incorporates two 1024×1024 ALADDIN III arrays which are sensitive from 0.9–5.6 μm (Kobayashi et al., 2000). The IRCS provides two plate scales, 20 and 52 mas per pixel, producing FOV of 21” and 54”, respectively. We selected the 52 mode and 0.6” slit width for *HK* grism spectroscopy covering 1.4–2.5 μm with $R \sim 320$. We conducted grism spectroscopy using AO188 and the laser guide star (LGS) mode. The observation was conducted on October 5 in 2013 under a partly cirrus condition. In order to subtract the background noise, we nodded the telescope pointing (ABBA) at each exposure. We conducted 2–4 sets of 240-sec exposure on each science frame. Dome flat frames and comparison frames were acquired at the end of observation. We observed F-type stars to measure the telluric absorption at the interval of each science object acquisition.

Table 3.3: Summary of the IRCS observations

Object Name	Exp. Time
tau1907	240s × 4 dithering × 2
tau4426	240s × 4 dithering × 4
tau154866	240s × 4 dithering × 4
Other information	
Obs. Mode	Long-slit spectroscopy with LGS AO188
Obs. Date	2013.10.05
Slit Width	0.6″
Grizm	*HK*500 (1.4 – 2.5 μm)
Resolution	∼ 320
Pixel Scale	52 mas/pixel

3.2 Data Reductions

3.2.1 Optical Imaging Data

The raw data were processed using the pipeline software SDFRED dedicated to the Suprime-Cam (Yagi et al., 2002; Ouchi et al., 2004) in the usual manner. For the processed images, the PHOT and DAOPHOT in IRAF package was used for the aperture photometry and the point-spread-function (PSF) photometry of the resolved stars.

The raw data were reduced by the standard procedure using SDFRED. Each raw image was bias-subtracted and trimmed, flat-fielded by self flat image, distortion and atmospheric dispersion corrected, PSF checked and matched, sky-subtracted and combined in the usual manner. In order to get high accuracy photometry, we conducted PSF photometry for objects having neighbors within 5×FWHM, and conducted aperture photometry for the other isolated objects. The PSF model of each processed image was generated and fitted to the sources by using DAOPHOT in the IRAF package with scripts for semi-automatic PSF photometry, AUTODAO provided by Dr. Noriyuki Matsunaga. The procedure to produce a photometric catalogue of each object is as follows:

Photometry

1. Detect the peaks of flux above the local background from each processed image with a 4σ detection threshold, and perform aperture photometry on the objects with radius 2″.

2. Generate the PSF model template of each image from 30 bright isolated stellar objects selected from the aperture photometric catalogues.

3. Compute coordinates and magnitudes of initial objects by fitting the PSF model with goodness of fit

statistic *chi* and image sharpness statistic *sharpness* parameters.

4. Estimate the value of the aperture correction, which must be added to the fitted magnitudes to produce the total magnitude, by computing the mean magnitude difference between the fitted magnitudes and the aperture photometry magnitudes computed through the large aperture of several bright isolated stars.

5. The instrumental magnitudes of sources in the images were calibrated using the photometric standard stars of Smith et al. (2002), observed with same air mass as the science frame during each run.

6. As a photometric catalogue, we applied the magnitudes of the PSF photometry for objects having neighbors within 5×FWHM, and performed aperture photometry for the other isolated objects.

An astrometric calibration was performed using the 2MASS Point Source Catalogue as a reference catalogue (Cohen et al., 2003) since the quality of the world coordinate system (WCS) originally embedded in the science frames was poor. Aperture photometry with PHOT was conducted for brighter sources and, at first, the WCS correction with WCSTools was conducted through matching the coordinate catalogue of our science frames with the 2MASS catalogue. This process improved the astrometric precision to a few subarcsec. However, the WCSTools are limited in the number of available reference positions (< 50 points), which limits the precision of the astrometry. In order to improve the precision, we ran SCAMP (Bertin, 2006) to obtain a third order polynomial fit to the distortions with about 1,000 2MASS sources and corrected the WCS coordinate using this. As a result, we found the mean astrometric errors to be $\lesssim 100$ mas in both the right ascension (R.A.) and declination (Decl.) directions.

We estimated the completeness limit in the images from the histogram of the detected magnitudes in our photometry. From the histogram of the TAUIII1 field, shown in Figure 3.2, we found the completeness limits to be $i' = 25.7$ and $z' = 25.1$ in this field. We show all the results in Table 3.1.

3.2.2 Near-Infrared Imaging Data

The raw data were processed in the usual manner using pipeline software provided by Dr. Akihiko Fukui. For the processed images, the PHOT in the IRAF package was used for aperture photometry.

The raw data were reduced using the standard procedure. Each raw image was dark subtracted, flat fielded by a self-flat image, mode count subtracted, 3σ clipped and combined on average. We conducted aperture photometry with the PHOT in the IRAF package. We detect the peaks of the flux above the local background from each processed image with a 4σ detection threshold, and perform aperture photometry on the objects with radius 2.5″. The instrumental magnitudes of the sources in the images were calibrated using several bright 2MASS sources in the same FOV. We conducted astrometric calibration of the science frames in the same way as §3.2.1, but without the SCAMP procedure due to the small number of 2MASS objects in our FOV. As a result, we found the mean astrometric errors to be ~ 250 mas in both the R.A. and Decl. directions. To correct for reddening caused by the molecular cloud, we estimated the visual extinction value by comparing the observed and the intrinsic YSO color–magnitude isochrones. As an intrinsic YSO color–magnitude isochrone, we used a synthetic stellar evolutional isochrone (BT-Settl: Allard et al., 2010).

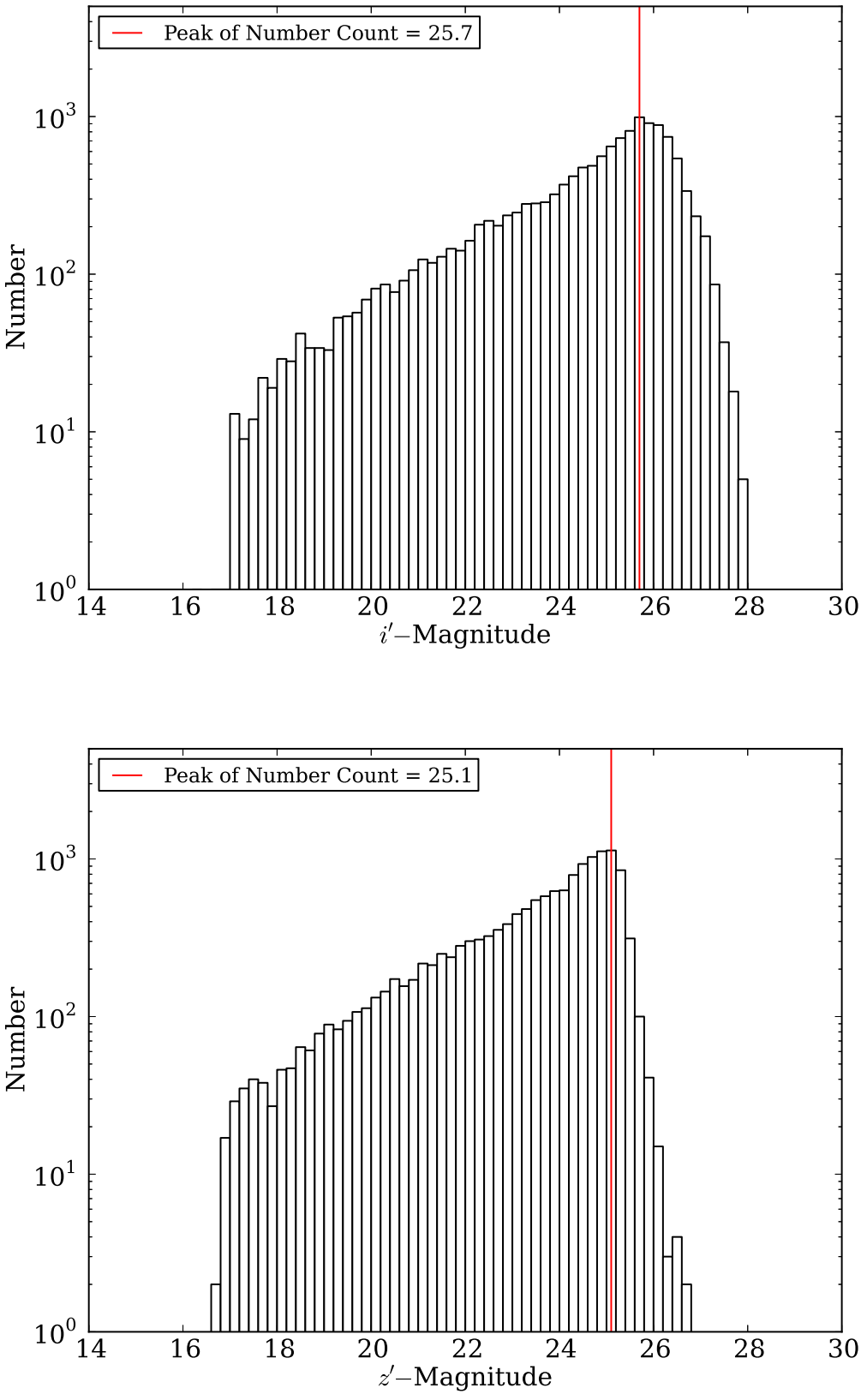

Figure 3.2: Histogram of the objects in the TAUIII1 field. The top panel shows the i'-band histogram and the bottom panel shows the z'-band histogram. The completeness limit of each FOV is determined from the peak of the histogram.

When an object had *J*- and *K*-band data, we applied a *J*–*K* vs *J* plane for an A_V estimate. Otherwise, when the object was not detected, we calculated the lower limit to use a 3 σ upper limit of the *J*-band magnitude. We assumed the extinction law $R_v = 3.1$, (A_J/A_V, A_H/A_V, A_K/A_V)=(0.282, 0.190, 0.114) (Cardelli et al., 1989).

3.2.3 Near-Infrared Spectroscopic Data

We reduced the near-infrared spectroscopic data in the standard manner as described in §2.2. In order to calibrate the wavelength of these data, we identified argon lines and determined the wavelength–pixel relation in the comparison frame. We then adopted the relation to the science frames. Since the influence of distortion was negligible, we did not correct the array distortion. We corrected the visual absorption of objects using the A_V value measured in §3.2.2 and the reddening law of Cardelli et al. (1989).

3.3 Analysis

In order to select PMO candidates before performing spectroscopy, we used color–magnitude and color–color diagrams. We conducted χ^2 SED fitting of the synthetic SED to the observed fluxes to derive these photometric parameters. To plot the parameters on an HR diagram, we selected young PMO candidates. For spectroscopic data, χ^2-fitting was conducted between the observed and synthetic spectra to derive their effective temperatures and surface gravity.

3.3.1 Sample Selection for Spectroscopy

We selected probable candidates for spectroscopic observation based on these colors as follows.

i', z', K Detection — We had access to multi-color photometric data from Subaru/Suprime-Cam, UKIRT/WFCAM, OAO/ISLE, *Spitzer* and *WISE*. We chose to use the i'-, z'- and K-bands from the data sets as the detection criteria because these three bands cover most of our FOV with high sensitivity. Therefore, we do not use the data for TAUV3 and TAUV4. In order to avoid non-linearity, we set the bright limit of the magnitude as $i' = 16.8$ and $z' = 16.6$. Also, we removed faint objects with large errors (> 0.2mag).

i', z', K Color Selection — We conducted color selection with the $i'z'K$ color to distinguish red embedded objects in the parent cloud from blue Galactic field stars. In star forming regions, young stellar objects become redder due to extinction from the parental molecular cloud and infrared excess from the circumstellar material. Therefore, we selected redder objects than the color predicted by synthetic isochrones of young stellar objects (BT-Settl model). As described in Figure 3.3, our criteria successfully distinguishes most of the known members from the population of field stars.

Color Selection Combining *Spitzer/WISE* Photometry — By using the *Spitzer/WISE* color, we removed early spectral type stars from our sample. We plotted known late-type members (>M6) and known M type field stars in the K-[4.5] vs i'–K plane, and we chose a border line along the A_V vector to select all late-type members. We removed bluer objects to the selection border line, whose uncertainty in *Spitzer* or *WISE* photometry is less than 0.2 mag.

A_V limitation — In order to our results with previous works in Taurus, we selected the sample within a extinction value $A_V < 4$, which is the same manner as the previous works (e.g., Briceño et al., 2002a; Guieu et al., 2006; Luhman, 2006) and reduces the background star contamination. Using the Taurus member list provided by Kenyon et al. (2008), we found that over 50% members have a lower extinction $A_V < 4$ in our FOV. Therefore this value is high enough to include a large number of members in our FOV.

In our FOV, there were 94 objects observed in previous studies (Guieu et al., 2006; Luhman, 2006; Luhman et al., 2009, 2010; Kraus & Hillenbrand, 2007; Rebull et al., 2010, 2011), and nine objects of these were late M-type objects. Since most of the known members were brighter than our bright limit of magnitude, only 10 objects were left before our color selection. We selected three red K-type objects and

three mid–late M-type objects, and removed early blue members. We cannot select late M-type members that are brighter (younger) than our limit, but we successfully removed only blue early type members.

Table 3.4: Astrometry data

Object Name	R.A. (J2000) [hh:mm:ss.ss]	Decl (J2000) [dd:mm:ss.s]	$\mu_\alpha \cos(\delta)$ [mas]	χ^2	μ_δ [mas]	χ^2	N_{fit}[b]	Baseline [year]
PMO candidates								
tau1907[a]	04:17:49.18	+28:19:01.1	13 ± 33	2.3	−146 ± 27	17.2	5	6.0
tau154866[a]	04:41:20.58	+25:55:19.5	−35 ± 49	0.6	−31 ± 44	0.0	4	5.0
Other substellar mass candidates								
tau677	04:17:22.77	+28:24:35.5	18 ± 34	7.6	−10 ± 34	2.8	4	4.0
tau1152	04:17:31.39	+28:16:21.6	−2 ± 38	0.4	31 ± 37	4.6	4	6.2
tau1835	04:17:47.36	+28:29:16.1	24 ± 35	1.3	31 ± 35	8.7	3	4.0
tau2751	04:18:16.53	+28:20:03.5	19 ± 9	0.1	−16 ± 9	0.3	5	13.9
tau4426[a]	04:18:59.82	+28:24:12.3	0 ± 28	0.2	6 ± 28	3.4	5	6.0
tau42771	04:33:49.12	+22:55:50.8	−67 ± 39	20.2	−168 ± 39	91.5	4	3.4
tau43800	04:33:51.72	+22:42:00.1	7 ± 32	3.7	−2 ± 32	1.3	4	3.9
tau112291	04:38:09.46	+26:16:05.8	−3 ± 11	3.2	2 ± 22	1.7	4	11.5
tau112603	04:38:10.42	+26:14:18.7	15 ± 11	2.3	−9 ± 23	1.6	5	11.5
tau128633	04:39:05.52	+25:51:42.0	−1 ± 10	0.3	1 ± 10	0.4	5	11.6
tau130655	04:39:14.62	+26:01:32.9	−16 ± 48	1.0	−16 ± 47	1.1	5	5.0
tau131362	04:39:18.37	+25:47:47.5	7 ± 14	0.1	−14 ± 15	3.2	5	11.6
tau131458	04:39:18.81	+25:33:53.2	46 ± 88	0.1	168 ± 88	2.6	4	1.6
tau133861	04:39:31.36	+25:43:13.1	127 ± 112	0.2	98 ± 112	1.0	3	1.1
tau134791	04:39:36.89	+26:23:07.6	−109 ± 93	6.1	84 ± 93	1.8	4	1.7
tau134902	04:39:37.56	+25:49:59.0	−11 ± 94	1.5	−124 ± 94	2.8	4	1.7
tau136525	04:39:48.09	+26:01:07.4	−14 ± 122	1.2	116 ± 122	0.1	3	1.1
tau136896	04:39:50.71	+25:36:56.3	26 ± 86	0.1	−24 ± 86	0.1	4	1.6
tau140677	04:40:14.41	+25:37:42.4	−25 ± 24	0.2	55 ± 45	6.1	5	5.0
tau141495	04:40:18.27	+25:23:06.7	−272 ± 97	3.0	7 ± 97	0.0	4	1.5
tau143361	04:40:26.40	+25:27:29.6	69 ± 90	1.2	263 ± 90	2.9	4	1.7
tau146563	04:40:40.02	+25:21:24.0	51 ± 20	0.5	−18 ± 24	0.1	5	11.6
tau147881	04:40:46.66	+25:29:31.6	30 ± 59	1.3	76 ± 30	0.1	5	5.2
tau151260	04:41:03.00	+25:29:40.5	−16 ± 44	1.0	−80 ± 36	13.7	5	5.2
tau156562	04:41:28.69	+25:34:12.8	−108 ± 89	1.3	−202 ± 89	7.1	4	1.6
Objects rejected by SED fitting due to the high effective temperatures								
tau1908	04:17:49.19	+28:24:30.7	0 ± 9	0.3	11 ± 9	1.8	5	13.9
tau2154	04:17:57.83	+28:19:59.0	23 ± 34	10.0	−7 ± 34	0.5	4	4.0
tau2229	04:18:00.58	+28:25:48.6	15 ± 34	5.5	27 ± 34	4.2	4	4.0
tau2605	04:18:12.72	+28:26:13.2	17 ± 34	0.2	−12 ± 34	1.1	4	4.0
tau112147	04:38:09.02	+26:08:01.4	20 ± 17	0.7	2 ± 25	0.3	5	11.5
tau115576	04:38:19.38	+25:55:26.1	−59 ± 94	0.6	−99 ± 94	1.1	4	1.7
tau128647	04:39:05.58	+25:51:29.7	−72 ± 95	0.0	6 ± 95	0.1	4	1.6
tau133247	04:39:27.89	+25:40:19.0	39 ± 93	0.2	−3 ± 93	0.3	4	1.7
tau135352	04:39:40.28	+25:49:07.1	9 ± 93	1.7	−125 ± 93	1.6	4	1.7
tau135992	04:39:44.58	+25:43:08.3	−1 ± 10	0.0	7 ± 10	0.0	4	11.1
tau140208	04:40:12.21	+26:05:33.2	−54 ± 112	0.3	−20 ± 112	0.6	3	1.1
tau150424	04:40:59.19	+26:08:44.7	−152 ± 93	4.7	157 ± 93	3.7	4	1.7
tau156932	04:41:31.32	+25:27:17.7	2 ± 13	2.6	−19 ± 13	0.0	4	11.1
Objects rejected from CM-diagram based on the data provided from our observation								
tau2370	04:18:05.65	+28:36:58.0	-	-	-	-	-	-
tau17907	04:32:43.87	+23:13:12.5	-	-	-	-	-	-
tau49818	04:34:06.44	+23:17:33.0	-	-	-	-	-	-
tau111618	04:38:07.47	+25:50:48.1	-	-	-	-	-	-
tau113963	04:38:14.32	+26:05:45.9	-	-	-	-	-	-
tau136414	04:39:47.25	+26:17:32.9	-	-	-	-	-	-
tau136744	04:39:49.53	+26:09:14.7	-	-	-	-	-	-
tau145277	04:40:34.36	+26:04:34.2	-	-	-	-	-	-

Note.

[a] Selected for spectroscopy.

[b] The number of data points used in measurement of the proper motion.

Table 3.5: Optical/near-infrared photometry data

Object Name	i' (AB)[mag]	z' (AB)[mag]	J [mag]	H [mag]	K [mag]	$I1$ [mag]	$I2$ [mag]
PMO candidates							
tau1907[a]	24.51 ± 0.15(1)	22.10 ± 0.03(1)	18.91 ± 0.18(4)	17.64 ± 0.04(1)	16.77 ± 0.04(2)	16.65 ± 0.13(6)	16.30 ± 0.34(6)
tau154866[a]	24.77 ± 0.06(1)	22.33 ± 0.02(1)	19.06 ± 0.13(2)	17.76 ± 0.04(1)	16.92 ± 0.06(2)	-	-
Other substellar mass candidates							
tau677	24.86 ± 0.19(1)	22.25 ± 0.03(1)	18.78 ± 0.16(2)	-	16.57 ± 0.03(2)	15.94 ± 0.06(5)	15.77 ± 0.11(5)
tau1152	24.51 ± 0.11(1)	22.07 ± 0.03(1)	19.11 ± 0.15(2)	17.62 ± 0.04(1)	16.76 ± 0.04(2)	15.95 ± 0.06(5)	15.91 ± 0.13(5)
tau1835	24.69 ± 0.18(1)	22.33 ± 0.04(1)	19.40 ± 0.28(4)	-	17.07 ± 0.05(4)	16.66 ± 0.14(6)	-
tau2751	22.28 ± 0.02(1)	20.29 ± 0.01(1)	16.86 ± 0.14(7)	14.99 ± 0.08(7)	13.92 ± 0.00(2)	13.28 ± 0.01(5)	13.09 ± 0.02(5)
tau4426[a]	23.94 ± 0.07(1)	21.75 ± 0.02(1)	18.61 ± 0.05(1)	16.66 ± 0.04(1)	16.06 ± 0.02(2)	15.70 ± 0.07(6)	15.24 ± 0.15(6)
tau42771	24.11 ± 0.08(1)	21.90 ± 0.04(1)	18.96 ± 0.11(2)	17.96 ± 0.50(3)	16.84 ± 0.04(2)	15.56 ± 0.03(5)	15.35 ± 0.06(5)
tau43800	25.14 ± 0.18(1)	22.70 ± 0.03(1)	> 21.71(2)	-	16.85 ± 0.05(2)	16.66 ± 0.13(6)	15.49 ± 0.19(6)
tau112291	22.38 ± 0.01(1)	20.34 ± 0.01(1)	16.75 ± 0.02(2)	14.59 ± 0.08(7)	13.70 ± 0.00(2)	12.96 ± 0.01(5)	12.75 ± 0.02(5)
tau112603	23.12 ± 0.02(1)	20.99 ± 0.01(1)	17.18 ± 0.03(2)	15.00 ± 0.09(7)	14.09 ± 0.00(2)	13.27 ± 0.01(5)	13.10 ± 0.02(5)
tau128633	23.56 ± 0.03(1)	21.20 ± 0.01(1)	17.28 ± 0.03(2)	15.27 ± 0.07(7)	14.30 ± 0.01(2)	13.77 ± 0.02(5)	13.47 ± 0.02(5)
tau130655	23.87 ± 0.04(1)	21.56 ± 0.01(1)	18.49 ± 0.07(2)	17.24 ± 0.03(1)	16.47 ± 0.04(3)	16.46 ± 0.14(6)	15.96 ± 0.29(6)
tau131362	24.99 ± 0.10(1)	22.69 ± 0.02(1)	17.98 ± 0.05(2)	15.67 ± 0.16(7)	14.59 ± 0.01(2)	13.88 ± 0.02(5)	13.70 ± 0.03(5)
tau131458	25.37 ± 0.13(1)	22.80 ± 0.02(1)	19.30 ± 0.15(2)	-	16.80 ± 0.05(2)	16.84 ± 0.15(5)	-
tau133861	25.56 ± 0.15(1)	23.09 ± 0.03(1)	19.12 ± 0.13(2)	-	16.15 ± 0.03(2)	15.30 ± 0.07(5)	15.19 ± 0.10(5)
tau134791	25.12 ± 0.14(1)	22.43 ± 0.02(1)	19.05 ± 0.14(2)	-	16.39 ± 0.04(2)	16.50 ± 0.13(6)	16.19 ± 0.38(6)
tau134902	23.72 ± 0.03(1)	21.43 ± 0.01(1)	17.99 ± 0.05(2)	-	15.65 ± 0.02(2)	14.93 ± 0.04(5)	14.81 ± 0.06(5)
tau136525	25.26 ± 0.14(1)	22.76 ± 0.02(1)	> 20.09(2)	-	17.09 ± 0.06(2)	16.87 ± 0.16(6)	-
tau136896	25.85 ± 0.18(1)	22.97 ± 0.03(1)	18.97 ± 0.11(2)	-	16.49 ± 0.03(2)	15.72 ± 0.08(5)	15.33 ± 0.10(5)
tau140677	25.53 ± 0.13(1)	22.93 ± 0.02(1)	19.71 ± 0.22(2)	18.12 ± 0.06(1)	17.27 ± 0.06(2)	-	-
tau141495	25.54 ± 0.14(1)	23.08 ± 0.03(1)	> 20.58(1)	-	17.29 ± 0.08(2)	-	-
tau143361	26.01 ± 0.08(1)	23.48 ± 0.01(1)	19.73 ± 0.19(2)	-	17.16 ± 0.06(2)	-	-
tau146563	22.89 ± 0.01(1)	20.91 ± 0.01(1)	17.59 ± 0.03(2)	15.89 ± 0.15(7)	15.08 ± 0.01(2)	14.49 ± 0.03(5)	14.21 ± 0.04(5)
tau147881	25.67 ± 0.01(1)	22.87 ± 0.02(1)	18.88 ± 0.09(2)	17.20 ± 0.07(1)	16.05 ± 0.02(2)	15.48 ± 0.06(5)	15.03 ± 0.07(5)
tau151260	26.01 ± 0.20(1)	23.37 ± 0.04(1)	> 19.32(2)	18.57 ± 0.10(1)	17.71 ± 0.10(2)	-	-
tau156562	24.97 ± 0.09(1)	22.48 ± 0.02(1)	19.04 ± 0.10(2)	-	16.43 ± 0.03(2)	15.55 ± 0.06(5)	15.20 ± 0.08(5)
Objects rejected by SED fitting due to the high effective temperatures							
tau1908	23.58 ± 0.07(1)	21.22 ± 0.01(1)	17.00 ± 0.03(2)	14.78 ± 0.07(7)	13.67 ± 0.00(3)	12.89 ± 0.01(5)	12.20 ± 0.01(5)
tau2154	24.85 ± 0.15(1)	22.50 ± 0.03(1)	18.65 ± 0.14(2)	-	15.72 ± 0.02(2)	15.03 ± 0.05(5)	14.86 ± 0.06(5)
tau2229	24.87 ± 0.19(1)	22.54 ± 0.03(1)	20.01 ± 0.11(1)	-	17.14 ± 0.06(2)	16.63 ± 0.12(6)	16.75 ± 0.50(6)
tau2605	24.82 ± 0.15(1)	22.27 ± 0.02(1)	18.64 ± 0.14(2)	-	15.66 ± 0.02(2)	15.17 ± 0.05(5)	14.96 ± 0.09(5)
tau112147	22.84 ± 0.02(1)	20.81 ± 0.01(1)	17.64 ± 0.04(2)	-	15.10 ± 0.01(2)	14.53 ± 0.03(5)	13.93 ± 0.03(5)
tau115576	22.67 ± 0.01(1)	20.68 ± 0.01(1)	17.69 ± 0.04(2)	-	15.42 ± 0.01(2)	14.78 ± 0.03(5)	14.86 ± 0.07(5)
tau128647	22.63 ± 0.01(1)	20.41 ± 0.01(1)	16.69 ± 0.02(2)	-	13.84 ± 0.00(2)	13.27 ± 0.01(5)	13.12 ± 0.02(5)
tau133247	24.60 ± 0.06(1)	22.23 ± 0.02(1)	18.52 ± 0.08(2)	-	15.31 ± 0.01(2)	14.60 ± 0.03(5)	14.53 ± 0.04(5)
tau135352	24.92 ± 0.09(1)	22.53 ± 0.02(1)	19.03 ± 0.12(2)	-	15.84 ± 0.02(2)	15.29 ± 0.05(5)	15.22 ± 0.08(5)
tau135992	22.20 ± 0.01(1)	20.10 ± 0.00(1)	16.30 ± 0.01(2)	-	13.33 ± 0.00(3)	12.07 ± 0.01(5)	11.93 ± 0.01(5)
tau140208	25.37 ± 0.10(1)	22.92 ± 0.02(1)	18.77 ± 0.11(2)	-	15.65 ± 0.02(2)	15.01 ± 0.04(5)	15.10 ± 0.09(5)
tau150424	25.71 ± 0.13(1)	23.16 ± 0.03(1)	19.15 ± 0.12(2)	-	15.93 ± 0.02(2)	15.06 ± 0.04(5)	14.72 ± 0.05(5)
tau156932	23.06 ± 0.02(1)	20.99 ± 0.01(1)	17.34 ± 0.02(2)	15.73 ± 0.14(7)	14.55 ± 0.00(2)	-	-
Objects rejected from CM-diagram based on the data provided from our observation							
tau2370	25.05 ± 0.20(1)	22.70 ± 0.04(1)	-	18.37 ± 0.11(1)	17.78 ± 0.10(1)	-	-
tau17907	25.72 ± 0.07(1)	23.27 ± 0.10(1)	-	-	> 18.25(1)	-	-
tau49818	25.74 ± 0.07(1)	22.23 ± 0.05(1)	-	-	> 17.95(1)	-	-
tau111618	25.46 ± 0.20(1)	23.01 ± 0.03(1)	-	-	> 18.25(1)	-	-
tau113963	25.04 ± 0.10(1)	25.01 ± 0.15(1)	-	-	> 18.25(1)	-	-
tau136414	26.07 ± 0.13(1)	23.56 ± 0.02(1)	-	-	> 18.25(1)	-	-
tau136744	25.70 ± 0.19(1)	23.26 ± 0.03(1)	-	-	> 18.10(3)	17.05 ± 0.20	-
tau145277	25.91 ± 0.17(1)	23.50 ± 0.03(1)	-	-	> 17.95(1)	-	-

Reference: (1) This work (2) GCS DR10 (3) GPS DR 8 (4) WSA(5)Spitzer (6) WISE (7) 2MASS

[a] Selected for spectroscopy.

Table 3.6: Selection status of previously known stellar and BD mass objects in our FOV

Object Name	Other Name	Spectral Type	Status
tau2968	V410 Anon-24	G1	Rejected from CC
tau3221	V410 Anon-25	M1	Rejected from CC
tau3334	IRAS04154+2823	M2	Rejected from CM
tau3408	V410 X-ray-2	K6, M0	Rejected from CC
tau3617	V410 X-ray-4	M3, M4	Rejected from CC
tau3648	LR 1	K4.5	all passed
tau13609	IRAS04295+2251	K7	all passed
tau53269	CFHT-Tau-1	M7	all passed
tau114134	2MASSJ 04381486+2611399	M7.25	all passed
tau130517	IRAS04361+2547	K2	all passed
tau134539	IRAS04365+2535	K2	Rejected from CM
tau138359	CFHT-Tau-17	M5.5, M5.75	all passed
tau2437	V410 X-ray-3	M6,M5.75	Too bright
tau4085	KPNO-Tau-2	M6.75, M7.5	Too bright
tau4357	IRAS04158+2805	M6	Too bright
tau27327	CFHT-Tau-12	M6,M6.5	Too bright
tau116212	GM Tau	M6.5	Too bright
tau128246	CFHT-Tau-6	M7.25	Too bright
tau136458	CFHT-Tau-4	M7	Too bright
tau152789	ITG34, CFHT-Tau-8	M6.5	Too bright
-	ITG2	M7.25	Saturated

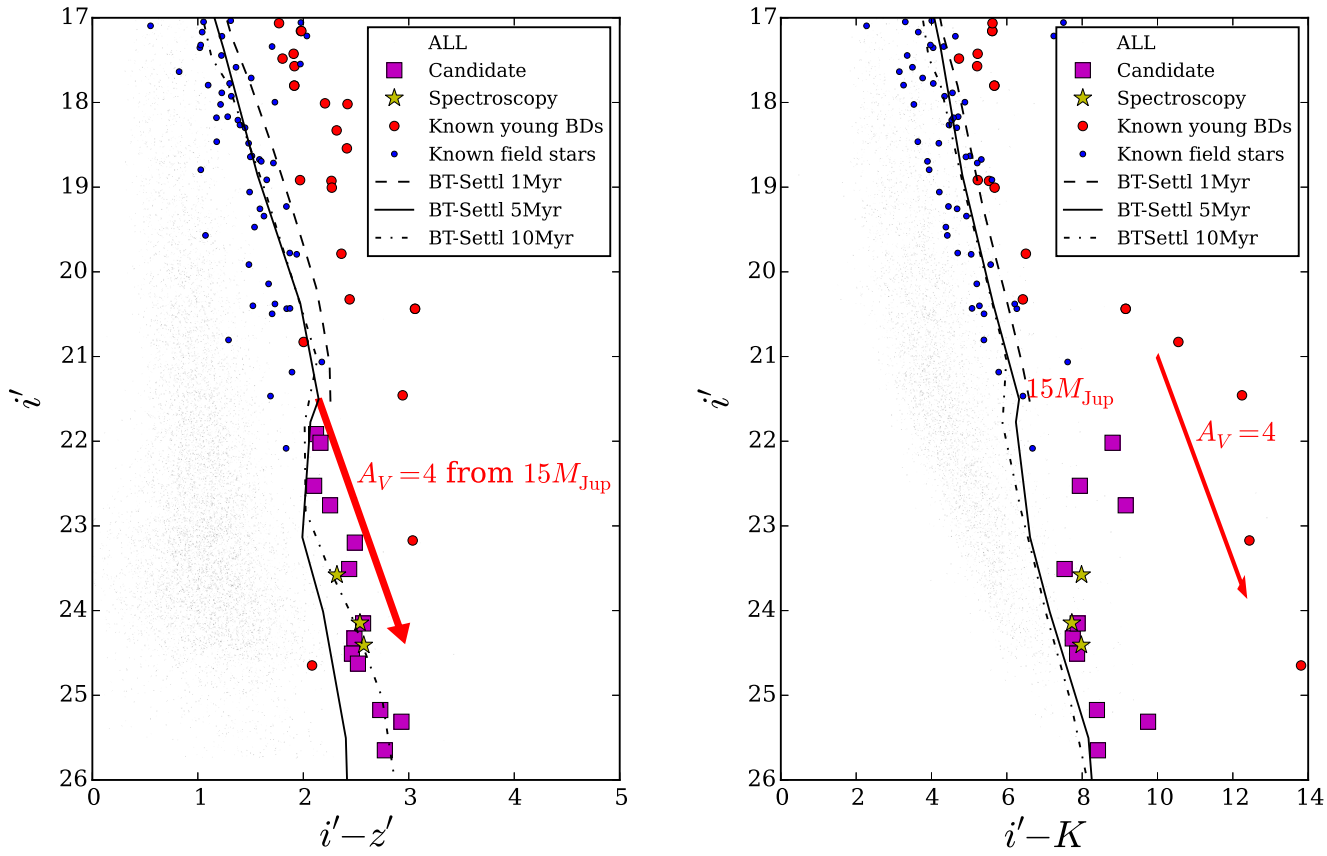

Figure 3.3: Color–magnitude diagram. The left panel shows the i'–z' vs i' diagram and the right panel shows the i'–K vs i' diagram. Black dots mean all observed objects, purple squares represent selected substellar mass candidates and yellow stars represent PMO candidates observed spectroscopically in this work. Known member and field stars are provided from Guieu et al. 2006 and Luhman et al. 2006, which are spectroscopic survey programs in Taurus. The theoretical isochrones (BT-Settl; Allard et al., 2010) are represented by the dashed line (1 Myr), the solid line (5 Myr) and the dash-dot line (10 Myr). The red arrow means the reddening vector with $A_V = 4$.

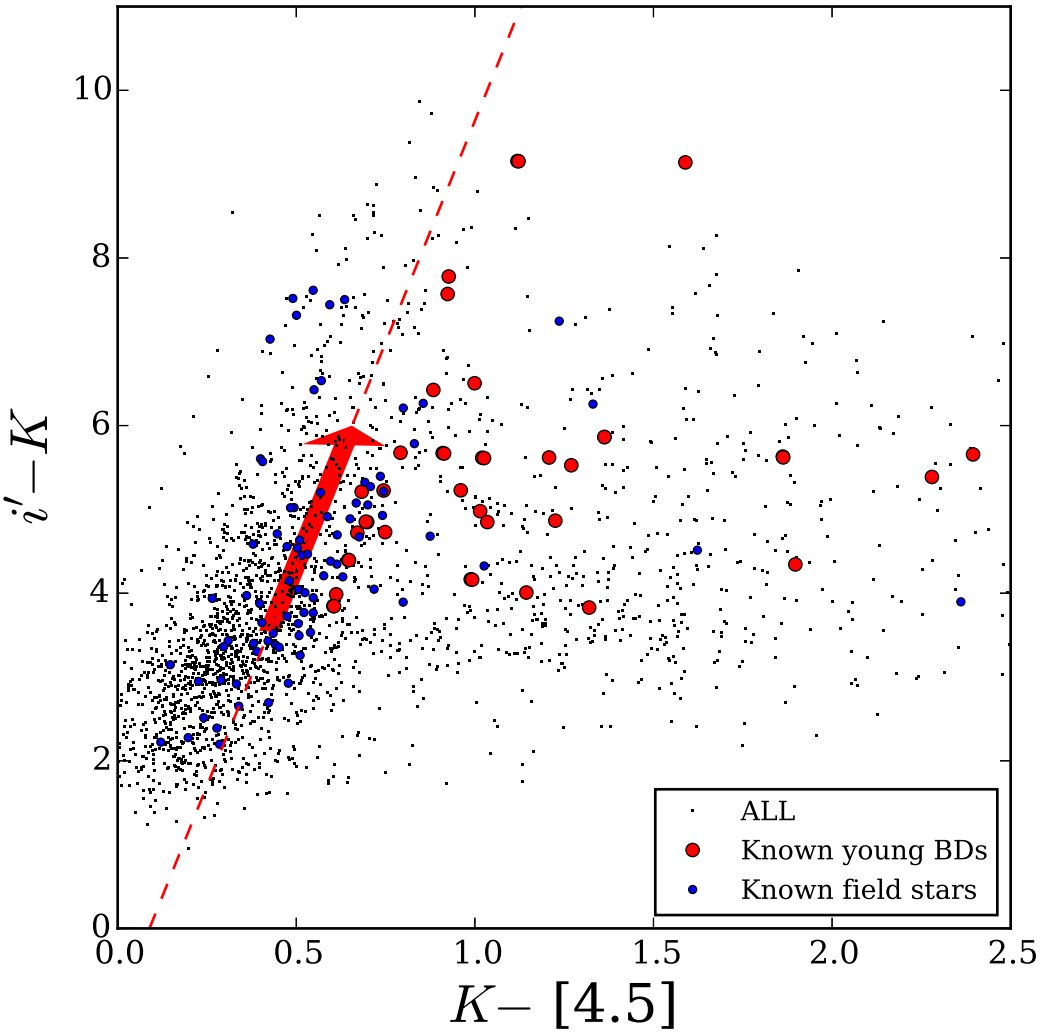

Figure 3.4: K–[4.5] vs i'–K diagram. All observed objects are represented by black dots. Known member (red circles) and field stars (blue circles) are provided from Guieu et al. (2006) and Luhman (2006). The red arrow means the reddening vector with $A_V = 4$. The dashed line means the selection border color.

3.3.2 Estimate of Photometric Physical Parameters

We estimate the photometric T_{eff} by SED fitting and estimate the age and mass from the HR diagram. We fitted our observed flux to the synthetic flux and found the best-fitting synthetic parameters. Along with the $T_{\rm eff}$ and luminosity calculated from the optical/infrared magnitudes, we plotted the photometric $T_{\rm eff}$ and luminosity on an HR diagram overlaid with the synthetic isochrone. By comparing the observed data with a grid of the synthetic HR diagram, we estimated the photometric mass and age of each object. Under this criteria, we removed older field star candidates (age >1 Gyr) from our sample data. The procedures of SED fitting and HR diagram plotting are explained in the next sub-section. In order to estimate the photometric physical parameters of our selected candidates, we conducted χ^2-fitting of synthetic SED to the observed flux. We restricted the fitting parameter ranges to 1800 K $\leq T_{\rm eff} \leq$ 4900 K and 3.0 $\leq \log(g) \leq$ 5.5. Also, we adopted solar metallicity as the average Galactic metallicity. The fit process minimizes the value of χ^2 defined as:

$$\chi^2 = \frac{1}{N-n}\sum^{N}\left(\frac{C\,f_{\rm mod} - f_{\rm obs}}{\sigma_{\rm obs}}\right)^2 \tag{3.1}$$

where N is the number of photometric points, n is the number of fitted parameters for the model, $f_{\rm mod}$ is the theoretical flux predicted by the model, $f_{\rm obs}$ is the observed flux and $\sigma_{\rm obs}$ the observational error in the flux. C is the scaling coefficient of $f_{\rm mod}$ with $f_{\rm obs}$, and is derived from $d\chi^2/dC = 0$ for Equation 3.1:

$$C = \frac{(\sum f_{\rm obs}\, f_{\rm mod}/\sigma_{\rm obs})^2}{\sum(f_{\rm mod}/\sigma_{\rm obs})^2}. \tag{3.2}$$

We show the result of this estimate of the photometric physical parameters in Table 3.7, and find several objects with very low temperature (< 2000 K). To derive the photometric mass, we convert $T_{\rm eff}$ to mass using the theoretical evolutional isochrones with an assumed age of $\sim$ 1 Myr. As a result, we find several PMO or BD candidates. In order to compare with previous works, we finally select two objects, tau1907 and tau154866, as PMO candidates based on their low $A_V < 4$ and magnitude of the i'-band above our completeness limit ($i' > 24.1$). In addition, we select a object, tau4426 as a low mass member for spectroscopy.

Table 3.7: Photometric physical parameters

Object Name	A_V [mag]	M_J [mag]	χ^2	$T_{\rm eff}$ [K]	log(g)	Age [Myr]	Mass [$M_\odot$]	IR ex.[a]	PM [b]
tau1907	2.7	12.42	5.3e-1	1800	5	80	0.023	no	-1
tau154866	4.2	12.14	1.5e+1	2100	5.5	> 100	0.070	no	-1
tau677	6.4	11.24	5.2e-1	2400	3.0	> 100	0.078	yes (SED)	-1
tau1152	7.0	11.41	2.4e-1	2700	3.5	> 100	0.094	no	-1
tau1835	5.2	12.20	3.8e+0	2400	3.0	> 100	0.080	no	-1
tau2751	9.3	8.51	2.1e+2	2800	4.0	10	0.046	no	1
tau4426	8.6	10.45	8.6e-1	3400	3.5	> 100	0.255	no	-1
tau42771	4.5	11.96	8.2e+0	2400	3.0	> 100	0.080	yes (SED)	-1
tau43800	> 20	-	-	-	-	-	-	-	-1
tau112291	10.5	8.06	2.2e+2	3000	4.0	20	0.098	no	2
tau112603	11.0	8.35	7.9e+1	2800	4.0	10	0.048	no	1
tau128633	10.1	8.70	8.1e+1	2600	4.0	9	0.028	yes (SED)	2
tau130655	5.3	11.26	5.3e+0	2500	3.5	> 100	0.084	no	-1
tau131362	13.0	8.58	1.2e+1	2600	4.0	7	0.028	no	1
tau131458	8.0	11.31	7.3e-1	2600	4.0	> 100	0.089	no	-1
tau133861	11.8	10.06	2.5e+0	3000	4.0	> 100	0.120	no	-1
tau134791	9.0	10.78	2.9e+0	2800	3.5	> 100	0.100	no	-1
tau134902	8.1	9.98	8.5e+0	2800	4.0	> 100	0.089	no	-1
tau136525	> 9.0	-	-	-	-	-	-	-	-1
tau136896	7.9	11.01	1.8e+0	2300	3.0	> 100	0.044	no	-1
tau140677	4.7	12.65	6.5e+0	1800	4.5	> 100	0.039	no	-1
tau141495	> 10.7	-	-	-	-	-	-	-	-1
tau143361	7.1	12.00	2.7e+1	2300	3.0	> 100	0.077	no	-1
tau146563	6.6	10.00	2.3e+2	2400	3.0	30	0.030	no	0
tau147881	7.2	11.12	4.3e+1	1800	3.5	< 1	0.006	yes	-1
tau151260	> 0.7	-	-	-	-	-	-	-	-1
tau156562	8.7	10.86	2.0e+0	2700	3.5	> 100	0.094	yes (SED)	-1

Note.
The values of A_V are measured from the $J-K$ vs J diagram. The χ^2- fitting provide χ^2, $T_{\rm eff}$, log(g). Age and Mass are derived from the HR-diagram.
[a] SED means IR excess confirmed from the SED.
[b] Indicating the status of the measured proper motion: 1. baseline $\geq$ 10 yr, $\chi^2 < 5$, consistent with the Taurus motion within 1 σ; 2. baseline $\geq$ 10 yr, $\chi^2 < 5$, consistent with the Taurus motion within 2 σ; baseline < 10 yr, or $\chi^2 \geq 5$

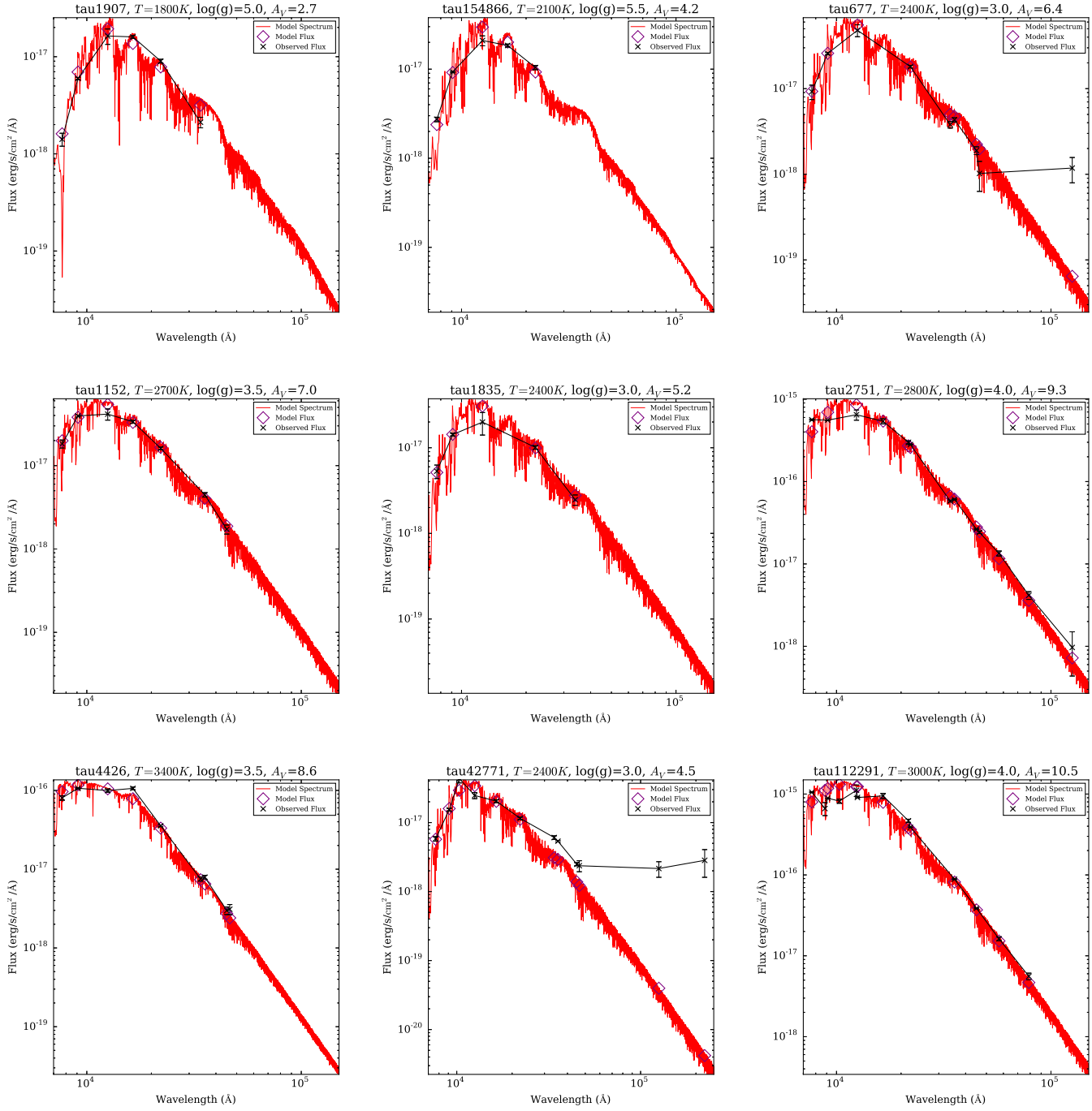

Figure 3.5: Result of SED fitting with two free parameters ($T_{\rm eff}$, log(g)). The observed flux (black crosses with error bars) is fitted by a model flux (purple diamonds) calculated from the model spectrum (red line). The fluxes at the longer than 3 μm obtained by the Spitzer and the WISE are not included in the fitting process. The effective temperature and the surface gravity are derived from a χ^2-fitting, and the visual extinction is determined in the color–magnitude diagram.

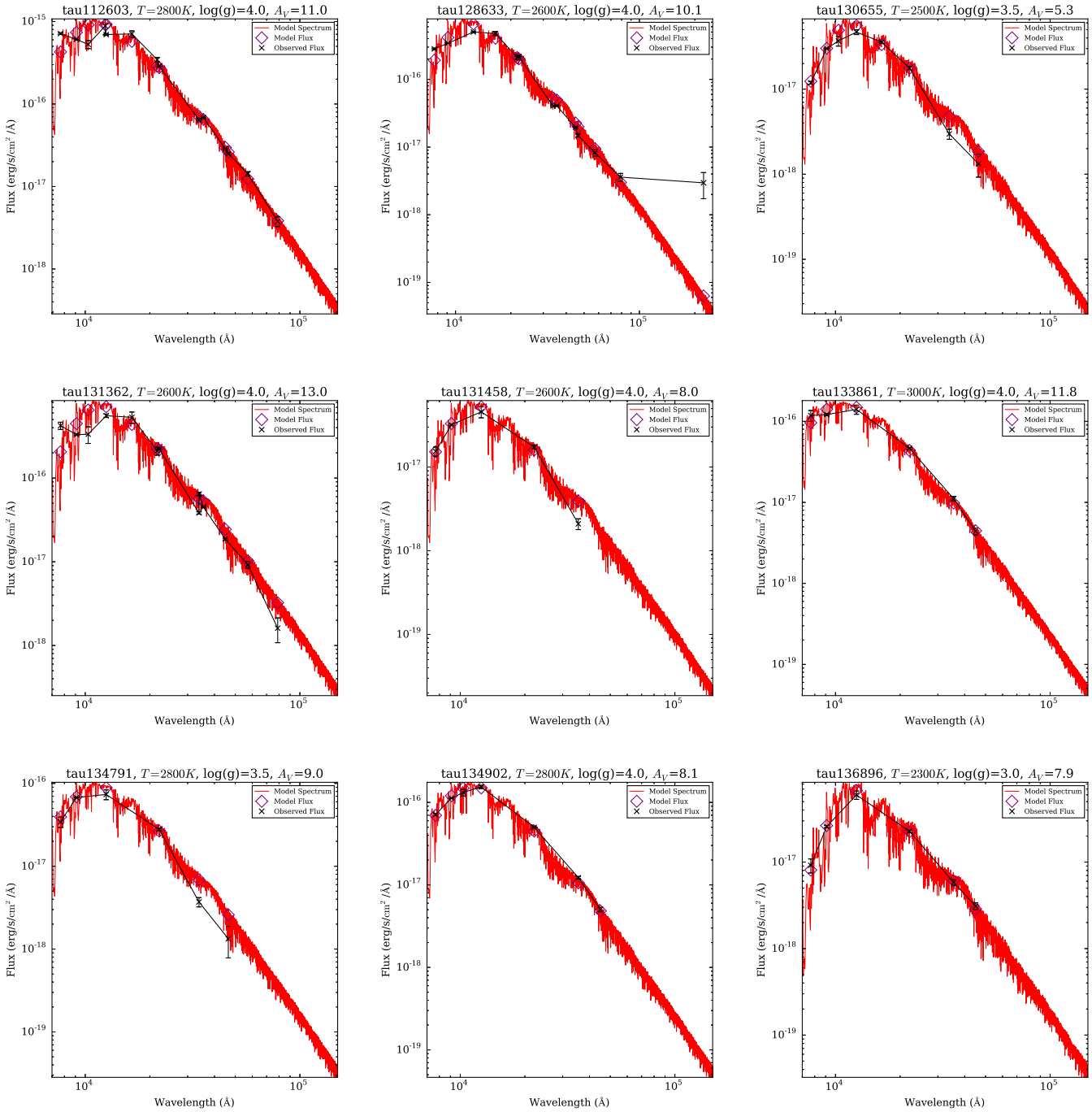

Figure 3.5: *Continued.*

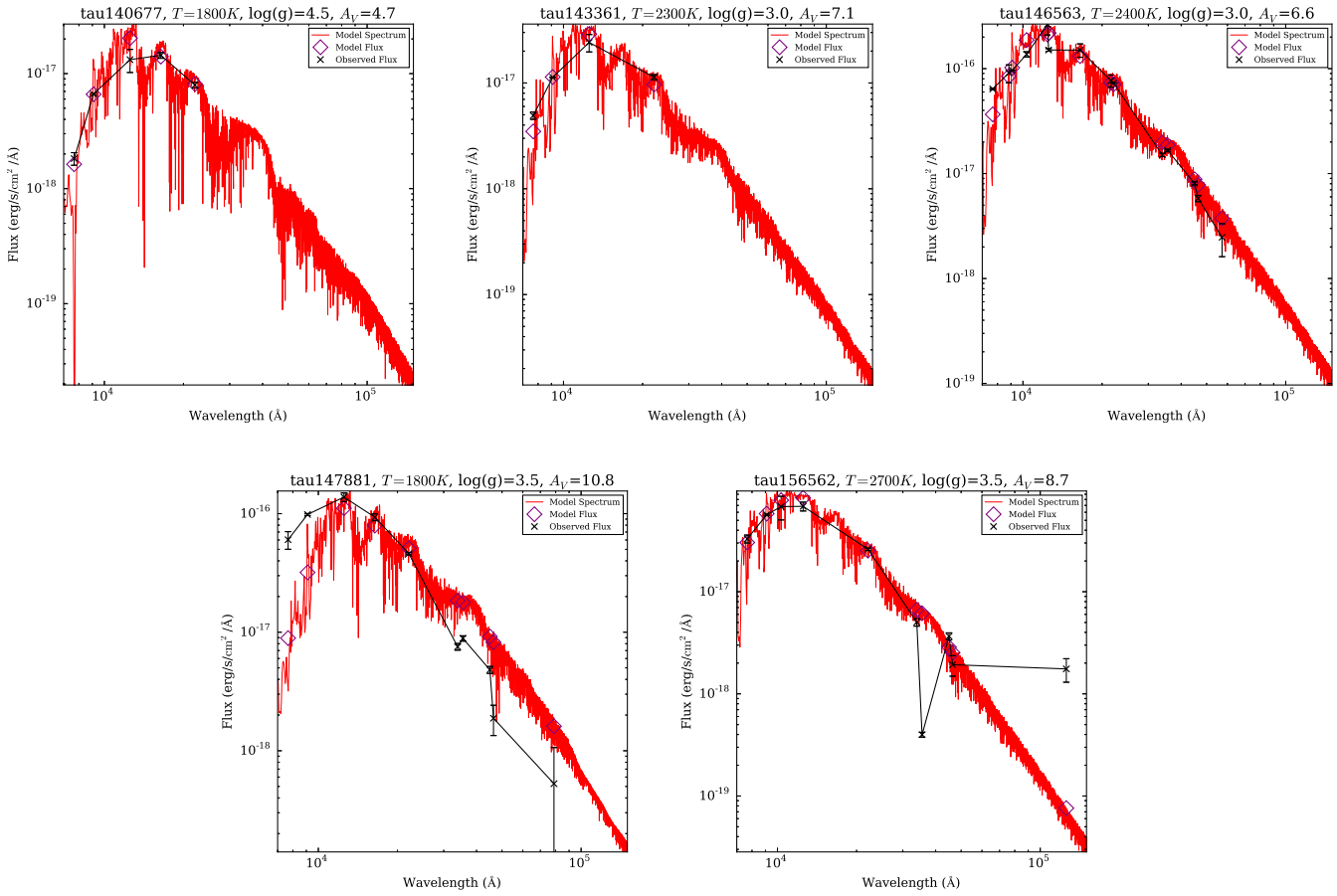

Figure 3.5: *Continued.*

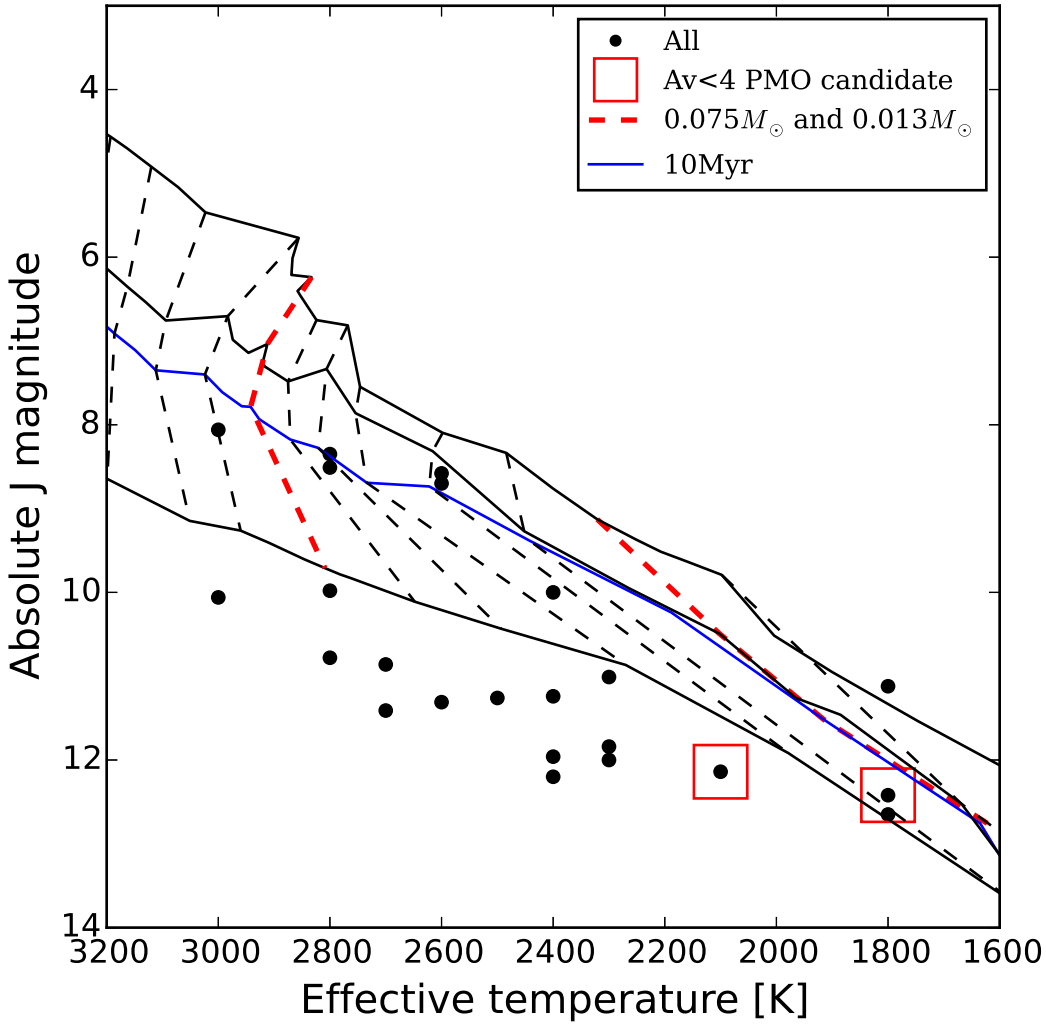

Figure 3.6: Photometric $T_{\rm eff}$ vs absolute $J-$band HR diagram. The lines indicate the synthetic HR-diagram (BT-Settl; Allard et al., 2010). The solid lines show the age isochrones 1, 5, 10, 100 Myr from top to bottom. The dashed lines show the mass isochrones 0.007, 0.013, 0.02, 0.03, 0.04, 0.05, 0.06, 0.075, 0.1, 0.11, 0.15 $M_\odot$ from right to left. (The red dashed lines indicate 0.013 and 0.075$M_\odot$.) The black dots indicate observed substellar candidates and the magenta squares represent the objects with $A_V < 4$.

3.3.3 Estimated Spectroscopic Physical Parameters

We obtained three spectra for our PMO and low mass candidates. In order to derive the spectroscopic physical parameters of the three objects, tau1907, tau4426 and tau154866, we compare our observed spectra to a grid of synthetic spectra and find the best-fit model in the χ^2 sense. The procedure is the same as that in §2.3, in which we used the BT-Settl model for the parameter ranges 1800K $\leq T_{\rm eff} \leq$ 4900K and 3.0 $\leq \log(g) \leq$ 5.5., We also used the solar metallicity as the average value in the TMC. In order to minimize telluric contamination from water vapor, we restrict the regions for the fit 1.5–1.78 μm and 2.10–2.38 μm.

We show the result in Table 3.8 and plot the observed and best-fit spectra in Figure 3.7. We find that the two best-fit spectra indicate a very low temperature ($T_{\rm eff} <$ 2000 K), even though the observed spectra lack water vapor absorption and clearly conflict with the best-fit model spectra. We therefore speculate that the uncertainty in the A_V estimate from the color–magnitude diagram degrades the fitting,, and we recalculate the A_V for a minimized χ^2 by using A_V as a free parameter in the SED fit. We show the result in Table 3.8 and Figure 3.7. We find that the χ^2 values improve and the best-fitting spectra reproduce the observed spectra well. However, since the recalculated A_V for our targets increases above the A_V estimated from their colors, the fitting result shows that these objects are not young PMOs, but rather are early-type field objects. We will discuss the details of this procedure in §3.4.1.

Table 3.8: Spectroscopic physical parameters: χ^2, $T_{\rm eff}$ and log(g) provided by the χ^2 fit.

Object	Color-magnitude diagram				SED fitting			
Name	A_V[a]	χ^2	log(g)	$T_{\rm eff}$	A_V[b]	χ^2	log(g)	$T_{\rm eff}$
tau1907	2.7	1.8	5.0	1800	7.0	1.0	5.0	3500
tau4426	8.6	1.3	5.0	3600	8.9	1.2	5.0	3700
tau154866	4.2	3.6	5.0	1800	6.8	2.4	5.0	3100

Note.
[a] The values of A_V are determined from a $J-K$ vs J diagram.
[b] The values of A_V are determined from the SED fitting.

3.3.4 Proper Motion Analysis

Another way to determine the cluster membership of our candidates is to analyze their proper motion. Proper motion studies of stellar members of the whole TMC show a wide dispersion in proper motion. Bertout & Genova (2006) provided average values and the standard deviation for the proper motions of the Taurus sample from Ducourant et al. (2005):

$$\mu_\alpha \cos(\delta) = 8.20 \pm 14.45 \text{ mas/yr}$$
$$\mu_\delta = -20.82 \pm 13.84 \text{ mas/yr}$$

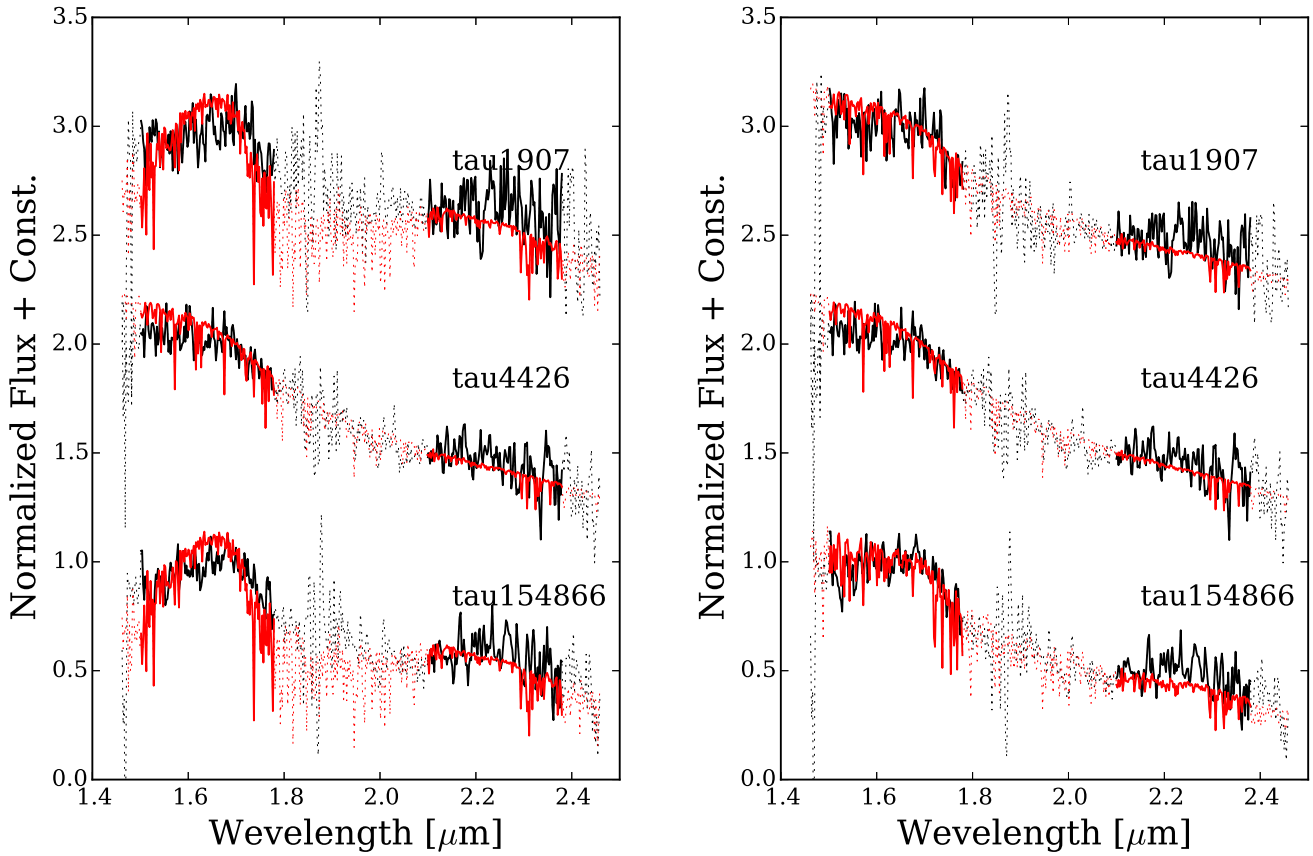

Figure 3.7: IRCS observed spectra (black) and best-fit synthetic spectra (red). The left panel shows the result with A_V determined from the color–magnitude diagram. The right panel shows the result with A_V determined from the SED-fit. In order to minimize telluric contamination from water vapor, we restrict the regions for the fit 1.5–1.78 μm and 2.10–2.38 μm.

This value is consistent with the median value of all Taurus members, ($\mu_\alpha \cos(\delta) = 6.1$ mas/yr and $\mu_\delta = -21.0$ mas/yr), provided by Luhman et al. (2009).

The proper motion space of Taurus members overlaps with that of the Galactic field objects. Quanz et al. (2010) simulated the proper motions of the Galactic disc and halo objects using the Besançon model (Robin et al., 2003, 2004). The simulation shows that most giant and sub-giant stars have a proper motion of $|\mu| < 5$ mas/yr, and the fraction of these objects with proper motion $\mu_\delta < -10$ mas/yr and $16 < J < 18$ is 3 ± 1 %. The fraction for bright M giants would be even smaller, and thus a proper motion measurement with a long time baseline would reject the giant hypothesis . However, because the proper motion space of disc dwarfs is more widely spread ($|\mu| > 10$ mas/yr) and overlaps with that of the Taurus members, the proper motion cannot completely remove the field dwarf contamination. A 5% fraction of field dwarfs with $16 < J < 18$ have a proper motion of $|\mu_\alpha| < 30$ mas/yr and $\mu_\delta < -15$ mas/yr.

Table 3.9: Astrometric properties in the catalogue used to derive proper motion

Catalogue	Mean epoch	Adopted error	Ref.	Mean offset	
	[year]	[mas]		R.A. [mas]	Decl. [mas]
2MASS	1997-2000	100	(1)	-	-
GCS	2005-2012	100	(2)	7	9
GPS	2005-2008	100	(2)	-12	14
WISE	2010	150	(3)	30	-16
Suprime-Cam	2009	100	(4)	-5	-1
ISLE	2012-2013	~ 200	(4)	33	10

Reference of adopted astrometric error : (1) Skrutskie et al. (2006); (2) Dye et al. (2006); (3)Cutri et al. (2012); (4) This work

We determine the proper motions of our candidates from a standard weighted linear fit (Teixeira et al., 2000). To check the procedure, we calculate the proper motions using the published data for the globular cluster 47 Tucanae (McLaughlin et al., 2006), and confirm to completely reproduce the published results . We determine the proper motions of our candidates over all available multi-epoch positions, including that of Suprime-Cam (assuming a 100 mas error), ISLE (with our estimated errors), 2MASS (assuming a 100 mas error; Skrutskie et al., 2006), UKIDSS positions (assuming a 100 mas error; Dye et al., 2006), and WISE All-Sky Database (assuming a 150 mas error; Cutri et al., 2012). For fainter objects, the astrometric errors increase due to their low S/N. Therefore, for 2MASS, if the error in the original catalogue is larger than the assumed error, we use the catalog error. We do the same for the WISE data, but we calculate the actual weighted mean position, epoch and standard deviation from the single exposure source table. For our Suprime-Cam data, we always use the assumed error value since the astrometry is based on the z'-band image, which shows all candidates with good S/N (> 10). For UKIDSS astrometry, we apply the same method since our candidates are sufficiently bright ($K < 18$) for UKIDSS sensitivity.

We present the measured proper motions in Table 3.4. Several objects with long time baselines (> 10 year) show good precision (~ 10 mas) in the proper motion. However, the majority have larger uncertainties

due to faintness and a short time baseline. In order to check our measurements, we calculated the proper motions of the samples whose membership have been confirmed as field stars or associated objects in Taurus in the previous work. We show the results in Figure 3.8, with the mean values and standard deviations of good solutions (time baseline > 5 years; $\chi^2 < 5$):

$$\begin{aligned} \mu_\alpha \cos(\delta) &= -0.25 \pm 12.64 \text{ mas/yr} \\ \mu_\delta &= 0.30 \pm 12.78 \text{ mas/yr} \quad \text{(Galactic field stars)} \end{aligned}$$

$$\begin{aligned} \mu_\alpha \cos(\delta) &= 5.24 \pm 7.66 \text{ mas/yr} \\ \mu_\delta &= -15.72 \pm 8.26 \text{ mas/yr} \quad \text{(Taurus member)} \end{aligned}$$

We use $\sim$ 900 field stars and $\sim$ 300 Taurus members in the calculation. We determine the proper motion of the field star samples to be nearly zero. The calculated proper motion of the Taurus members is consistent with the result of Bertout & Genova (2006), however the absolute value along the Decl. direction is slightly smaller than the previous calculated value. This difference might be explained by the coordinate offset of each catalogue. For confirmation, we measure the mean offset of the catalogue positions to the 2MASS counterparts. We used field star samples with $K_S < 14$ (resultant sample number $\sim$ 400), and show the result in Table 3.9. We find that most of the mean offset is sufficiently smaller ($\lesssim$ 10 mas) than the adopted error. We note though that the mean offset along the R.A. direction of WISE and ISLE is slightly larger than the others, but the offset has a smaller weight on the proper motion due to the large astrometric error. Also, we found that the proper motion of the field star sample was nearly zero, and hence the effect of the mean offset in the catalogue coordinate is not likely to contribute to the difference in the proper motions. Rather, the difference in the proper motions can be explained by the difference in the catalogues used in the calculation. Since all our astrometric data use the 2MASS position as the WCS reference, including additional astrometric catalogues in the calculation can change the result . Therefore, we recalculated the proper motion of Taurus members by including the USNO-A2.0 catalogue (Monet, 1998), which was also used in a previous proper motion study of Taurus (assuming 250 mass error; Ducourant et al., 2005). We used Taurus members including $K_S < 14$ and $B < 19$ with a long time baseline of > 20 years (with a resultant sample number of $\sim$ 150), and found that the measured proper motion of $\mu_\alpha \cos(\delta) = 5.15 \pm 4.02$ mas/yr, $\mu_\delta = -19.24 \pm 4.98$ mas/yr, which is closer to the results of Bertout & Genova (2006). Therefore, the difference in the catalogue used in the calculation can explain the difference in the measured proper motion.

Unfortunately, the USNO-A2.0 catalogue is largely unavailable for use as our Suprime-Cam counterpart owing to its sensitivity. Meanwhile, the mean proper motion of Taurus members without the USNO-A2.0 is still consistent with Bertout & Genova (2006). Therefore, while we compared the measured proper motions with that of Bertout & Genova (2006), we regard proximity only as one of the membership indexes, not a definite index. Since the proper motion space of Taurus members largely overlaps that of Galactic field stars, the method used in this work is relatively conservative. We add the index of the proximity to Bertout & Genova (2006) in Table 3.7.

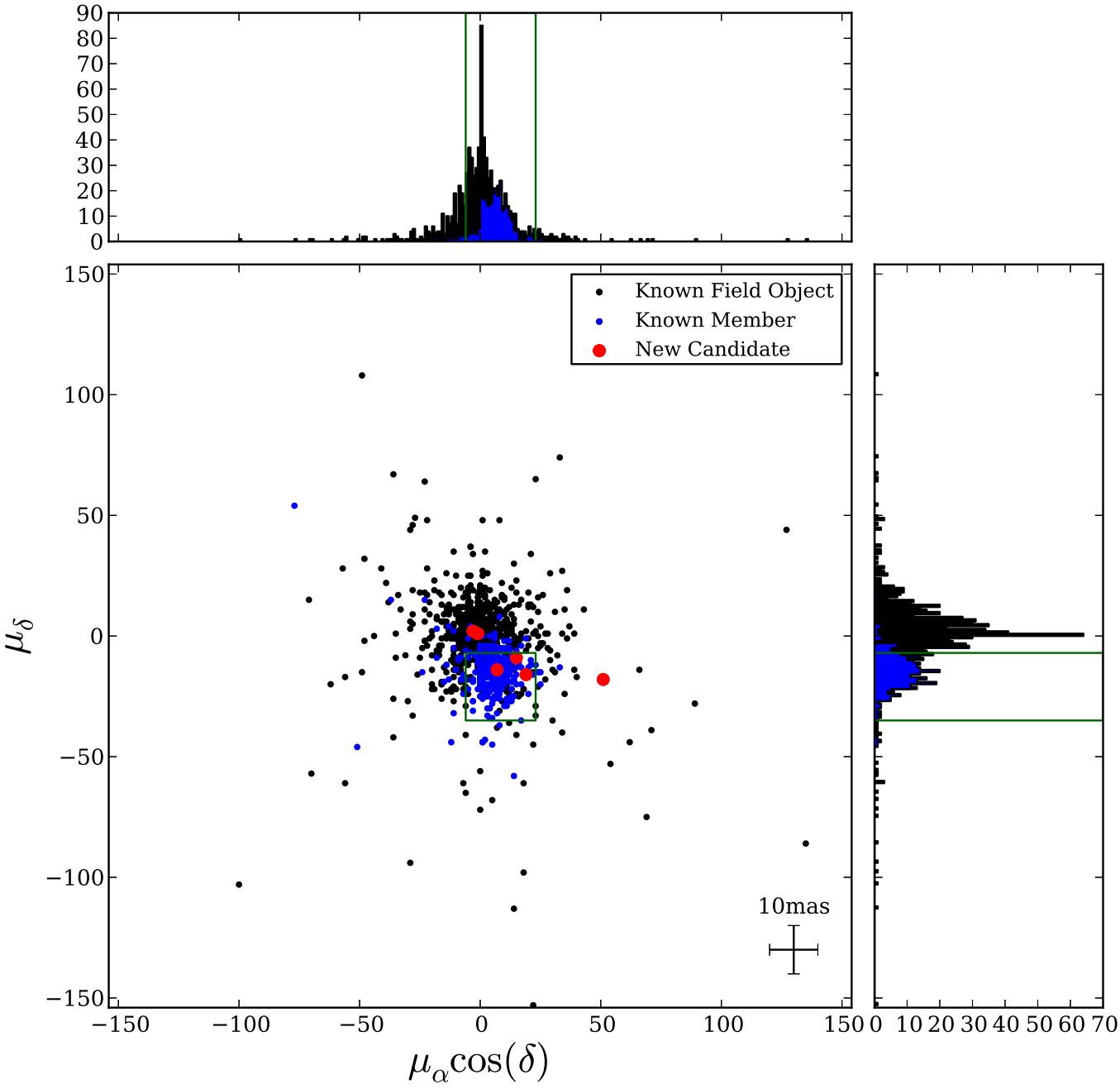

Figure 3.8: Proper motion distribution showing the proper motions of known field stars (black), known Taurus member (blue) and our substellar candidates (red), which have long baselines (≥ 10 yr) and good χ^2 values (< 5). The green square indicates the range of the proper motion reported by Bertout & Genova (2006).

3.4 Discussion

3.4.1 Survey Completeness

In this section we will consider the possibility that we have missed some PMOs due to biases in the color selection or in the parameter estimates.

Spatial coverage of Taurus member — We check the coverage of our FOV for the distribution of Taurus member. Using the average age of Taurus (∼1 Myr Kenyon et al., 2008) and the one-dimension velocity dispersion (∼1km/s Luhman et al., 2009), we can estimate that the moving distance of the Taurus members is $\sim$ 1 pc. Since our FOV is $\sim 1^\circ \times 1^\circ$ at most, we do not miss a large number of the stellar members. As shown in Figure 3.1.1, our FOV for the TAUIII group covers most members associated with the neighboring stellar group. Therefore, if the velocity dispersion of the PMOs was same as that of the stellar members, we would not miss many PMO members.

Color-magnitude diagram — We plot 1 Myr and 5 Myr theoretical isochrones in Figure 3.3. In addition, considering the age of Taurus (1–10 Myr; Kenyon et al., 2008), we compare the 10 Myr isochrone with the 1 Myr and 5 Myr isochrones. In the i'–K vs i' plane, we find that the 10 Myr isochrone is similar to the 5 Myr isochrone. On the other hand, in the i'–z' vs i' plane, the 10 Myr isochrone is similar to the 5 Myr isochrone, but becomes redder below $20M_{\rm Jup}$. Therefore, we have not missed any PMO candidates due to the model used in the selection. However, our selection misses two known Class I objects in the i'–z' vs z' plane due to their peculiar blue color. The high fraction of Class I objects is associated with a refraction nebular (Connelley et al., 2007), which scatters the light from a central star and causes a Class I object to appear bluer. We missed such blue objects in our selection, but Class I objects suffer from very high extinction ($A_V \sim 20$) and our interest is in very cool objects with low extinction ($A_V < 4$). Therefore, this limitation is unimportant for our conclusion.

Color–color diagram — In this plane, we set the border to select all known BD members (SpT≥M6) and reject many early-type stars. However, as seen in Figure 3.4, since there is a large scatter in the color of known background objects, we should check the SpT of the contaminants in our selection. We found that most of the objects with ≥ 4 (32/34) will contaminate our selection field, and half of the objects with M3–M4 (6/11) will become contaminants. For about ≤ M3, we reject most of such objects (2/35), but since there are few samples in the M1–M3 SpT range due to the completeness of previous research (Guieu et al., 2006; Luhman, 2006), the contribution to our selection is unclear. Therefore, we conclude that ≥M3 objects from the Galactic field contaminate our color selection.

A_V estimate — We indicate that the A_V estimate from SED fitting improves the χ^2 value above that from the color magnitude diagram in §3.3.3. As described in §3.2.2, we calculated the χ^2 using a value of A_V estimated from the J–K vs J diagram. The A_V estimate using the color–magnitude or color–color diagram has been adopted in many studies of star forming regions since the procedure is simple and the typical uncertainty is not significant ($\Delta A_V \sim 1$). However, the method depends on the model or experimen-

tal color used. For example, some authors might assume that the intrinsic stellar J–K color is unity for the A_V estimate, and this assumption is reasonable when we observe M9 or earlier objects whose J–K color is almost unity. However, if we focus on late M-type objects (SpT > M9), we overestimate A_V since M9 or late SpT objects clearly becomes redder than J–K = 1. On the other hand, if we use a synthetic isochrone of young low mass objects, we underestimate the A_V of Galactic field stars, which seem redder due to visual extinction. Therefore, in studies focusing on faint PMOs, we should more carefully estimate A_V. Then, as described in §3.3.3, we estimate the A_V in minimizing the χ^2-fit with three free parameters, $T_{\rm eff}$, log(g) and A_V (Alves de Oliveira et al., 2010). Hereafter, we call the A_V measured from the color–magnitude diagram as $A_{V,color}$, and the A_V measured from the SED fitting as $A_{V,SED}$. In this method, since we do not assume an intrinsic color of the object of interest, we expect that we can calculate A_V without any assumption. To confirm the validity of using $A_{V,SED}$, we checked whether we could reproduce the A_V value correctly using SED fitting from artificial photometric data. We generated artificial data from photometry on the synthetic spectra whose flux is scaled with the J-band magnitude set (J = 15 or 16), with the temperature and A_V given by 2000 K < $T_{\rm eff}$ < 4600 K and 0 < A_V < 20. We estimate A_V for the artificial data using the two A_V determination methods. We show the results in Figure 3.9 and Table 3.10. Our findings are: 1) $A_{V,color}$ has a systematic error such that it will be overestimated for lower $T_{\rm eff}$; 2) the systematic error becomes worse for fainter objects; 3) $A_{V,SED}$ has slightly larger dispersion, but no systematic error. Based on these findings, we choose the result using $A_{V,SED}$ in this thesis instead of the result using $A_{V,color}$.

$T_{\rm eff}$ estimate — In the same manner as for the A_V estimate, we checked the validity of the $T_{\rm eff}$ estimate. We compare the calculated $T_{\rm eff}$ from SED fitting with the input $T_{\rm eff}$, and show the results in Figure 3.10. For low visual extinction A_V < 10, we find a good agreement between the calculated and input $T_{\rm eff}$ except for input $T_{\rm eff}$ ∼ 3300 K. For high visual extinction $A_V \geq 10$, the dispersion of the calculated $T_{\rm eff}$ for the input value becomes worse, and the χ^2 value increases (> 10). In the comparison between the previously estimated $T_{\rm eff}$ from spectroscopy and this work, we find a good agreement for field dwarf stars, but a discrepancy for field giant stars since our adopted surface gravity (log(g) = 3.0–5.5) cannot cover that of giant stars (log(g) ∼ 0). Therefore, we conclude that our SED fitting procedure can successfully reproduce the effective temperatures of BDs and PMOs with $T_{\rm eff}$ < 3000 K and A_V < 10. On the other hand, we should carefully treat the case of $T_{\rm eff}$ > 3000 K since we might fail to estimate $T_{\rm eff}$ of such early type stars. However, it is unlikely that an object with an estimated temperature of $T_{\rm eff}$ > 4000 K is actually a very low mass object with $T_{\rm eff}$ < 2500 K.

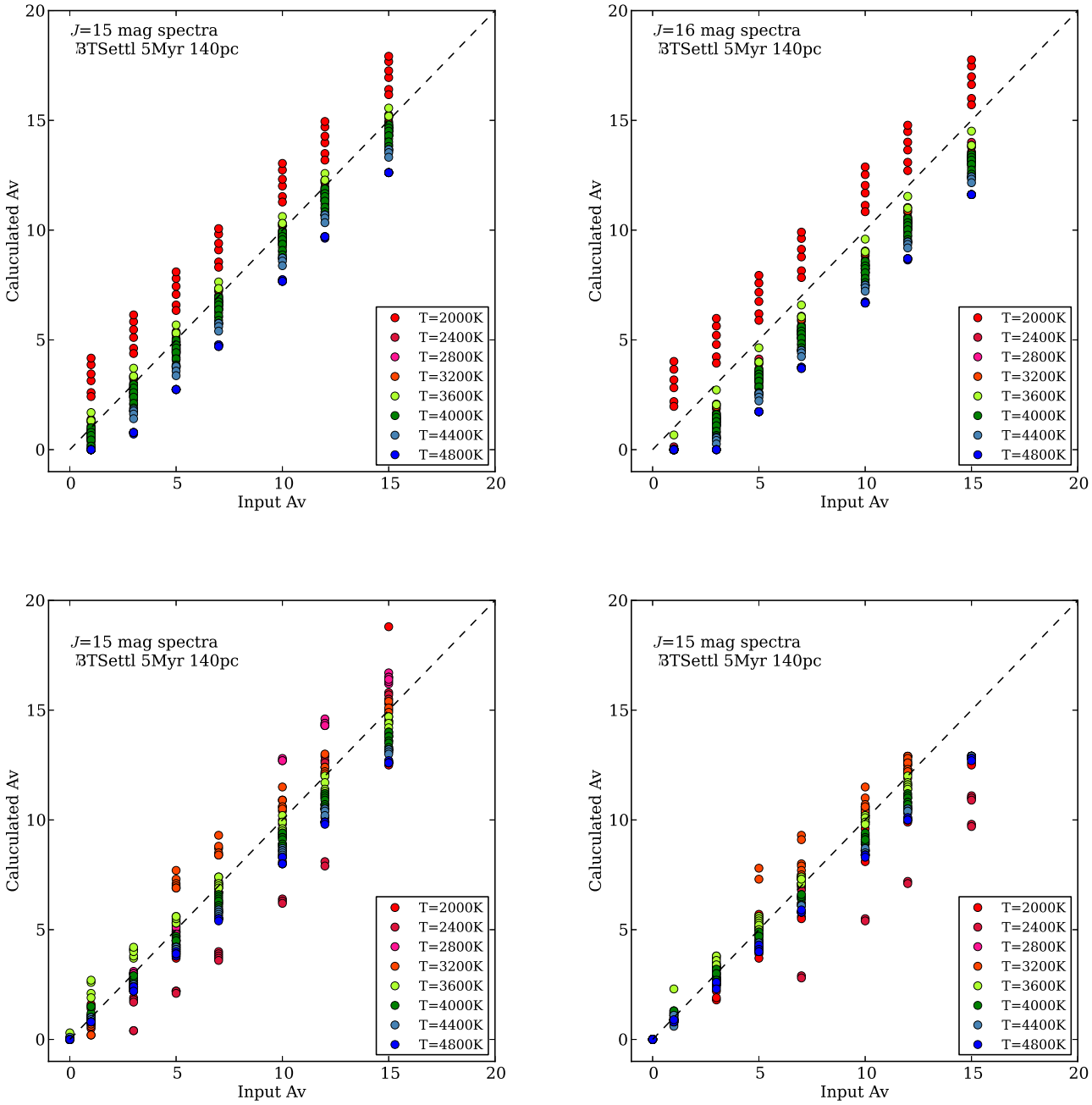

Figure 3.9: Input A_V vs calculated A_V. The calculated A_V is determined from the theoretical flux with the input A_V. The upper panels show the result for A_V calculated from the color–magnitude diagram. The bottom panels show the result of SED fitting. The upper left panel shows the case of the input magnitude $J = 15$. The upper right panel shows the case of $J = 16$. The bottom left panel shows the result with a four-filter set ($i'z'JK$) and the bottom right panel shows the result with a five-filter set ($i'z'JHK$).

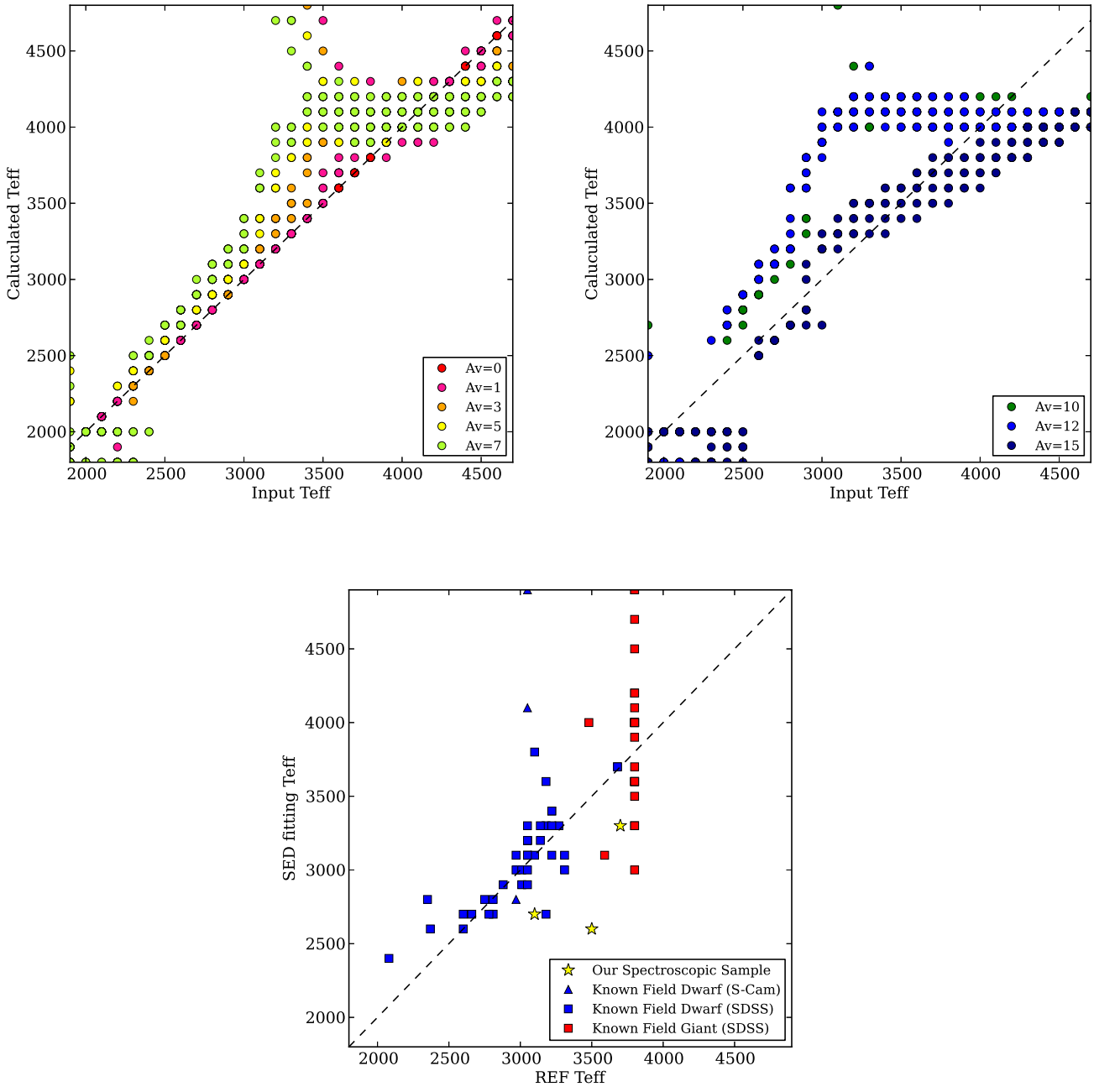

Figure 3.10: Input $T_{\rm eff}$ vs calculated $T_{\rm eff}$. The upper panels show the calculated $T_{\rm eff}$ determined from the theoretical flux with the input $T_{\rm eff}$. The bottom panel show the result calculated for the template flux. The upper left panel shows the case for $A_V < 10$ and the upper right panel shows the case for $A_V \geq 10$

Table 3.10: Calculated A_V from synthetic photometry given by the input A_V

Input A_V	Calculated A_V − Input A_V			
	$A_{V,color}$[a], $J = 15$	$A_{V,color}$, $J = 16$	$A_{V,SED}$[b], $J = 15, i'z'JK$	$A_{V,SED}$, $J = 15, i'z'JHK$
1	-0.2 ± 0.9	-0.7 ± 0.8	-0.0 ± 0.5	-0.0 ± 0.3
3	-0.3 ± 1.1	-1.4 ± 1.3	-0.2 ± 0.9	-0.1 ± 0.7
5	-0.4 ± 1.1	-1.5 ± 1.3	-0.5 ± 1.2	-0.4 ± 1.1
7	-0.4 ± 1.1	-1.5 ± 1.3	-0.4 ± 1.1	-0.2 ± 0.9
10	-0.4 ± 1.1	-1.6 ± 1.3	-0.6 ± 1.5	-0.6 ± 1.3
12	-0.4 ± 1.1	-1.6 ± 1.3	-0.7 ± 1.6	-0.9 ± 1.2
15	-0.5 ± 1.1	-1.6 ± 1.3	-0.8 ± 1.7	-2.4 ± 0.7

Note.
[a] The values of A_V are determined from a $J - K$ vs J diagram.
[b] The values of A_V are determined from the SED fitting.

3.4.2 Observational Features of Individual Objects

We compare the photometric parameters using $A_{V,color}$ with those using $A_{V,SED}$, and summarize the features of individual objects.

PMO candidates — We found that two PMO candidates and a low mass candidate can be identified as early type stars with spectroscopy. We show the photometric parameters of two PMO candidates estimated from $A_{V,SED}$ in 3.11 and find that the PMO candidates might be early type field objects.

Table 3.11: Photometric physical parameters of the PMO candidates

Object Name	A_V [mag]	M_J [mag]	χ^2	$T_{\rm eff}$ [K]	log(g)	Age [Myr]	Mass [$M_\odot$]	IR ex.[a]	PM[b]
tau1907	7.0	11.21	3.1e-2	2700	4.5	> 100	0.094	no	-1
tau4426	8.9	10.37	2.6e+0	3500	3.0	> 100	0.353	no	-1
tau154866	6.8	11.41	7.7e-2	2600	4.5	> 100	0.089	no	-1

Note.
The values of A_V are measured from the χ^2−fitting. The χ^2− fitting provide χ^2, $T_{\rm eff}$, log(g). Age and Mass are derived from the HR-diagram.
[a] SED means IR excess confirmed from the SED.
[b] Indicating the status of the measured proper motion: 1. baseline $\geq$ 10 yr, $\chi^2 < 5$, consistent with the Taurus motion within 1 σ; 2. baseline $\geq$ 10 yr, $\chi^2 < 5$, consistent with the Taurus motion within 2 σ; baseline < 10 yr, or $\chi^2 \geq 5$

From the analysis of Quanz et al. (2010), we should consider contamination from Galactic field dwarfs, giants and carbon stars. A proper motion measurement with a long time baseline would reject the giant

hypothesis. However, the short time baseline (< 10 yr) for our targets means that we cannot reject it. Therefore, based on the apparent K magnitude, we derived a range for the potential distance module ($m_K - M_K$) for our candidates. Using

$$d = 10^{0.2(m_K - M_K)+1} \tag{3.3}$$

we can estimate the physical distances d (in pc) for our candidates if they were indeed carbon stars or M giants. This shows that the minimum distances for these objects would be over 140 kpc for carbon stars, whose derived distances lie way beyond the currently known extent of our Galaxy. The minimum distances would be around 100 kpc for mid-late M giants, which is still reasonable. In the same way, if we assume that these objects are field M dwarfs, we could estimate the distances to be 500–1000 pc. Therefore, we can reject the carbon star hypothesis, but it is likely that these three objects are indeed background M dwarfs or distant M giants.

Table 3.12: Typical absolute K-band magnitude of carbon stars and M-type giants and the corresponding minimum and maximum distance module if our candidates were such objects.

			tau1907		tau4426		tau154866	
		M_K	$m_K - M_K$	Distance	$m_K - M_K$	Distance	$m_K - M_K$	Distance
		[mag]	[mag]	[kpc]	[mag]	[kpc]	[mag]	[kpc]
Object Type	Ref.	max/min	max/min	max/min	max/min	max/min	max/min	max/min
Carbon stars	(1)	-8.8/-5.7	24.79/21.69	908/218	23.89/20.79	600/144	24.94/21.84	972/233
M0 III – M7 III	(2)	-7.6/-4.0	23.59/19.99	522/100	22.69/19.09	345/66	23.74/20.14	560/107

Reference. (1) Tanaka et al. (2007); (2) SIMBAD Astronomical Database (2MASS catalog; Hipparcos catalog)

Other substellar mass candidates — We show the photometric parameters of other candidates estimated from $A_{V,SED}$ in 3.13. We found that most of the candidates might be early type field objects. However, we note that these objects do not always have $i'z'JHK$, which changes the resultant parameter from that of the SED fitting, although it is unlikely that these objects are actually low mass BDs or planetary mass members. In samples of highly embedded candidates with $A_V > 4$, tau136896 might be BD mass candidates. Therefore, a imaging follow-up with a long time baseline or a spectroscopic follow-up to confirm their membership is required. Five objects of our substellar candidates appear to have infrared excess in the SEDs. Two of them, tau2751 and tau128633, have similar proper motions as the Taurus members. Therefore, these objects might be young stellar objects. However, since our photometric $T_{\rm eff}$ has a relatively large uncertainty, these objects appear older in the HR diagram. To confirm their membership, a spectroscopic follow-up is needed.

L-type member candidate: 2M0437+2331 — 2M0437+2331 has been identified as the first isolated L-type member in the TMC (Luhman et al., 2009). The identification as an L-type object in the spectrum has been confirmed in the visual regime by Luhman et al. (2009) and the near-infrared by Alves

de Oliveira+2013. However, its location in the HR diagram indicates that the age of 2M0437+2331 might be > 100 Myr, which is too old for the age of Taurus (1–10 Myr). Therefore, to confirm its membership, we conducted the proper motion analysis of this object by adding a new data point taken with OAO/ISLE. Our analysis shows that the proper motion is ($\mu_\alpha \cos(\delta) = 4 \pm 18$ mas/yr, $\mu_\delta = -50 \pm 20$ mas/yr) using an $\sim$ 15-year time baseline from 2MASS (1998) to ISLE (2013). In comparison with the proper motion provided by Bertout & Genova (2006), the motion along the R.A. direction from our data is consistent, but the amount of proper motion along the Decl. direction is larger. We can explain this by assuming that 2M0437+2331 has been ejected from its birth place, since the location of 2M0437+2331 is relatively distant from the dense stellar groups of the TMC. If this is the case, it would be very interesting for the formation of PMOs since it might be direct evidence for the ejection scenario in PMO formation. On the other hand, there is a possibility that 2M0437+2331 is a contamination from a nearby association, namely the Pleiades moving group since the proper motion of 2M0437+2331 is nearer that of Pleiades ($\mu_\alpha \cos(\delta) \sim 19$ mas/yr, $\mu_\delta \sim -45$ mas/yr; Robichon et al., 1999) than Taurus, and the age estimated from HR diagram is consistent with Pleiades (125 ± 8 Myr; Stauffer et al., 1998). The location of 2M0437+2331 is actually far away ($\sim$ 10 deg) from the Pleiades center, but some distant Pleiades candidates have been reported by Frink et al. (1997). However, it is difficult to conclude the membership of 2M0437+2331 because of the large uncertainty in 2M0437+2331's proper motion ($\sim$ 20 mas/yr). Since the infrared magnitude of 2M0437+2331 ($K_s = 15.44$) is fainter than the detection limit of the 2MASS detector ($K_s = 14.3$), the uncertainty in the 2MASS position is worse, although the time baseline is sufficiently long for a precise determination of the proper motion (err < 10 mas). In addition, the faintness on the HR diagram could be explained by episodic accretion in the early stage of stellar evolution (Baraffe et al., 2009). Therefore, we must carefully consider the membership of 2M0437+2331. A more precise position determination of 2M0437+2331 will be useful for this discussion.

Table 3.13: Photometric parameters of other substellar mass candidates

Object Name	A_V [mag]	M_J [mag]	χ^2	$T_{\rm eff}$ [K]	log(g)	Age [Myr]	Mass [$M_\odot$]	IR ex.[a]	PM[b]
tau677	8.2	10.74	1.2e-2	2700	5.5	> 100	0.094	yes (SED)	-1
tau1152	7.8	11.18	3.0e-1	2900	5.0	> 100	0.108	no	-1
tau1835	7.6	11.53	1.6e-1	2900	5.5	> 100	0.108	no	-1
tau2751	11.5	7.89	1.2e+1	4000	3.0	> 100	0.631	yes (SED)	1
tau42771	6.6	11.37	4.8e-1	2800	3.5	> 100	0.100	yes (SED)	-1
tau43800	-	-	-	-	-	-	-	-	-1
tau112291	11.9	7.66	1.0e+1	4000	3.0	> 100	0.631	no	2
tau112603	12.9	7.81	5.6e+0	4000	3.0	> 100	0.631	no	1
tau128633	13.5	7.74	2.6e+0	4200	3.0	> 100	0.692	yes (SED)	2
tau130655	6.3	10.98	5.8e-1	2700	3.5	> 100	0.094	no	-1
tau131362	17.7	7.26	1.3e+0	4800	3.0	> 100	0.851	no	1
tau131458	9.5	10.89	1.8e-2	2900	4.5	> 100	0.108	no	-1
tau133861	14.2	9.38	4.1e-1	4500	3.0	> 100	0.767	no	-1
tau134791	10.0	10.50	2.9e-1	3000	5.5	> 100	0.120	no	-1
tau134902	9.2	9.66	6.4e-1	3100	3.5	> 100	0.136	no	-1
tau136525	-	-	-	-	-	-	-	-	-1
tau136896	9.2	10.64	5.1e-2	2500	3.0	> 100	0.063	no	-1
tau140677	8.4	11.61	2.2e-1	2800	5.5	> 100	0.100	no	-1
tau141495	-	-	-	-	-	-	-	-	-1
tau143361	10.4	11.07	1.7e-1	3300	3.0	> 100	0.196	no	-1
tau146563	10.5	8.90	6.1e-1	4200	3.0	> 100	0.692	no	0
tau147881	11.9	9.79	4.2e-2	3000	3.5	> 100	0.119	no	-1
tau151260	7.7	> 11.42	1.3e-2	2600	3.0	> 100	> 0.089	-	-1
tau156562	10.5	10.35	4.0e-3	3200	5.5	> 100	0.160	yes (SED)	-1

Note.
The values of A_V are measured from the $J-K$ vs J diagram. The χ^2- fitting provide χ^2, $T_{\rm eff}$, log(g). Age and Mass are derived from the HR-diagram.
[a] SED means IR excess confirmed from the SED.
[b] Indicating the status of the measured proper motion: 1. baseline $\geq$ 10 yr, $\chi^2 < 5$, consistent with the Taurus motion within 1 σ; 2. baseline $\geq$ 10 yr, $\chi^2 < 5$, consistent with the Taurus motion within 2 σ; baseline < 10 yr, or $\chi^2 \geq 5$

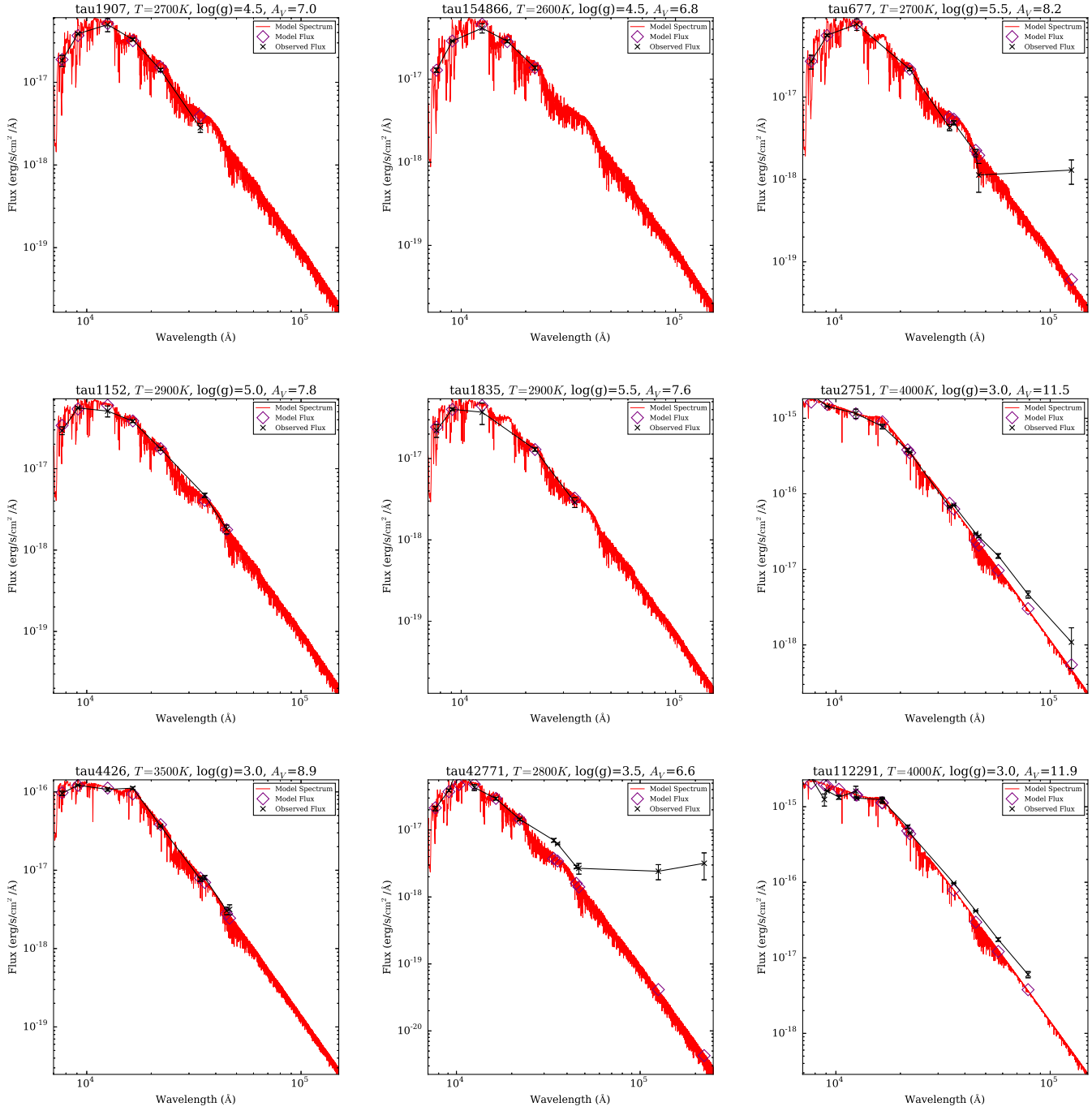

Figure 3.11: Result of SED fitting with three free parameters ($T_{\rm eff}$, log(g), A_V). The observed flux (black crosses with error bars) is fitted by the model flux (purple diamonds), which is calculated from the model spectrum (red line). The fluxes at the longer than 3 μm obtained by the Spitzer and the WISE are not included in the fitting process. The effective temperature, the surface gravity and the visual extinction are derived from a χ^2-fitting.

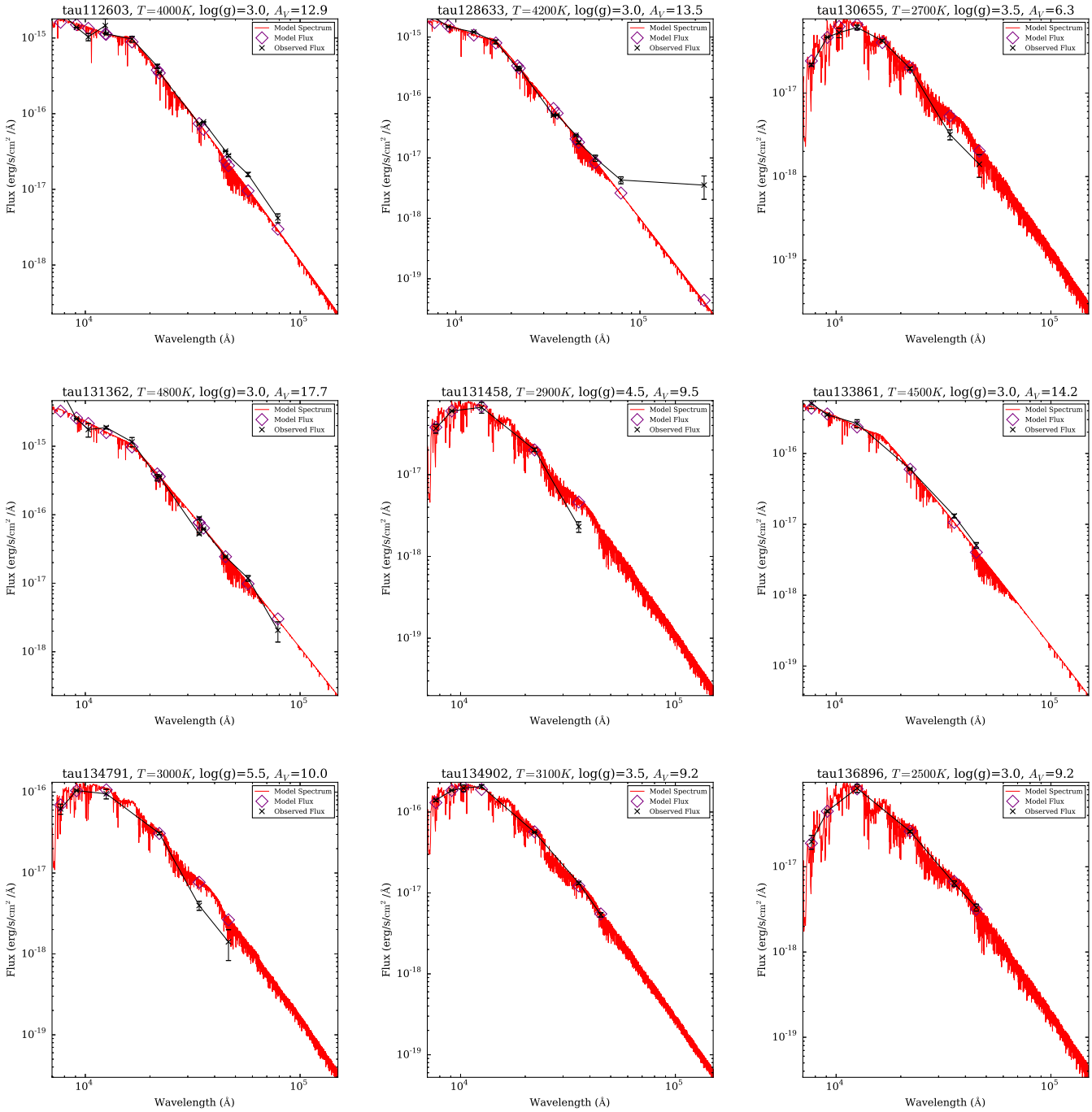

Figure 3.11: *Continued.*

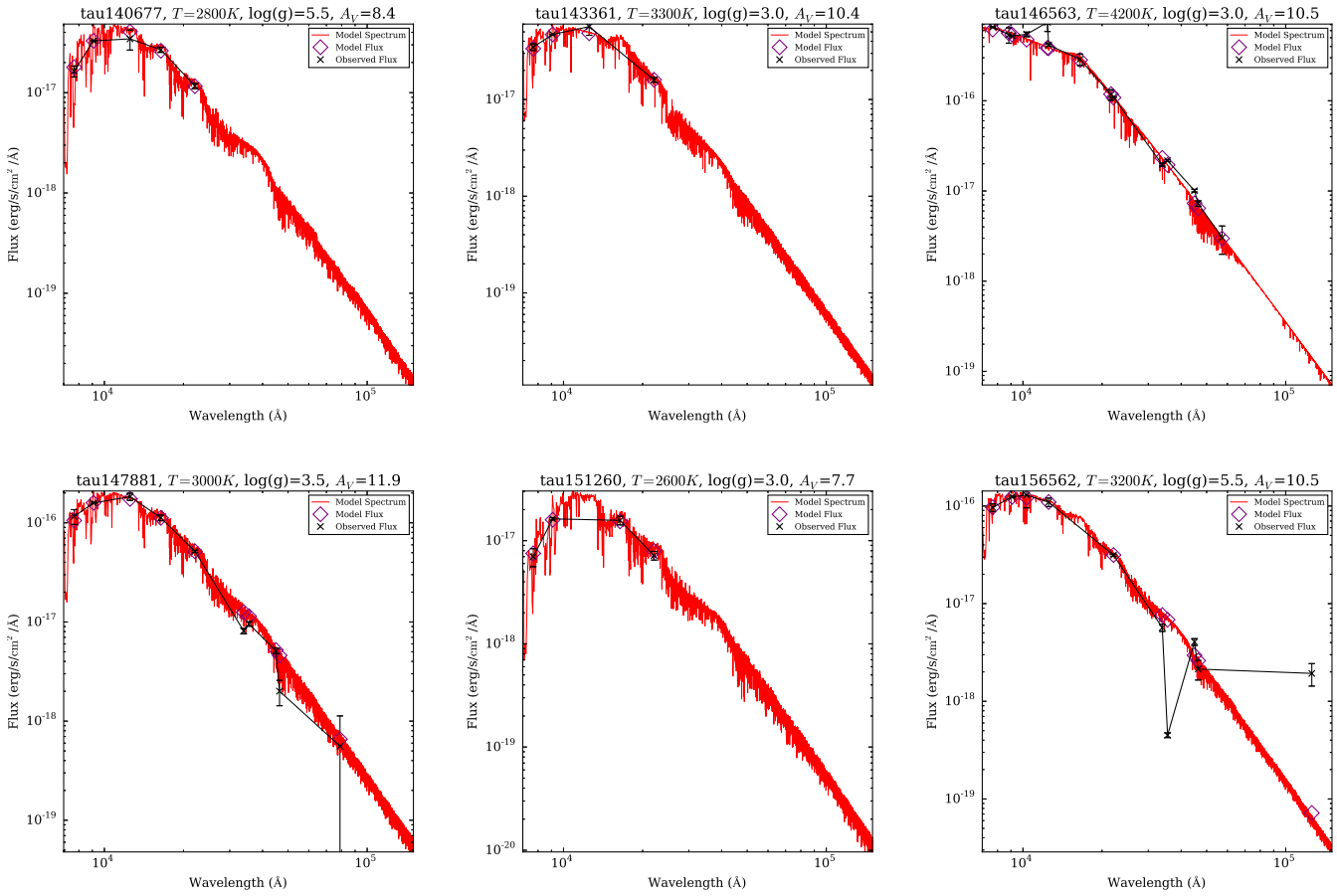

Figure 3.11: *Continued.*

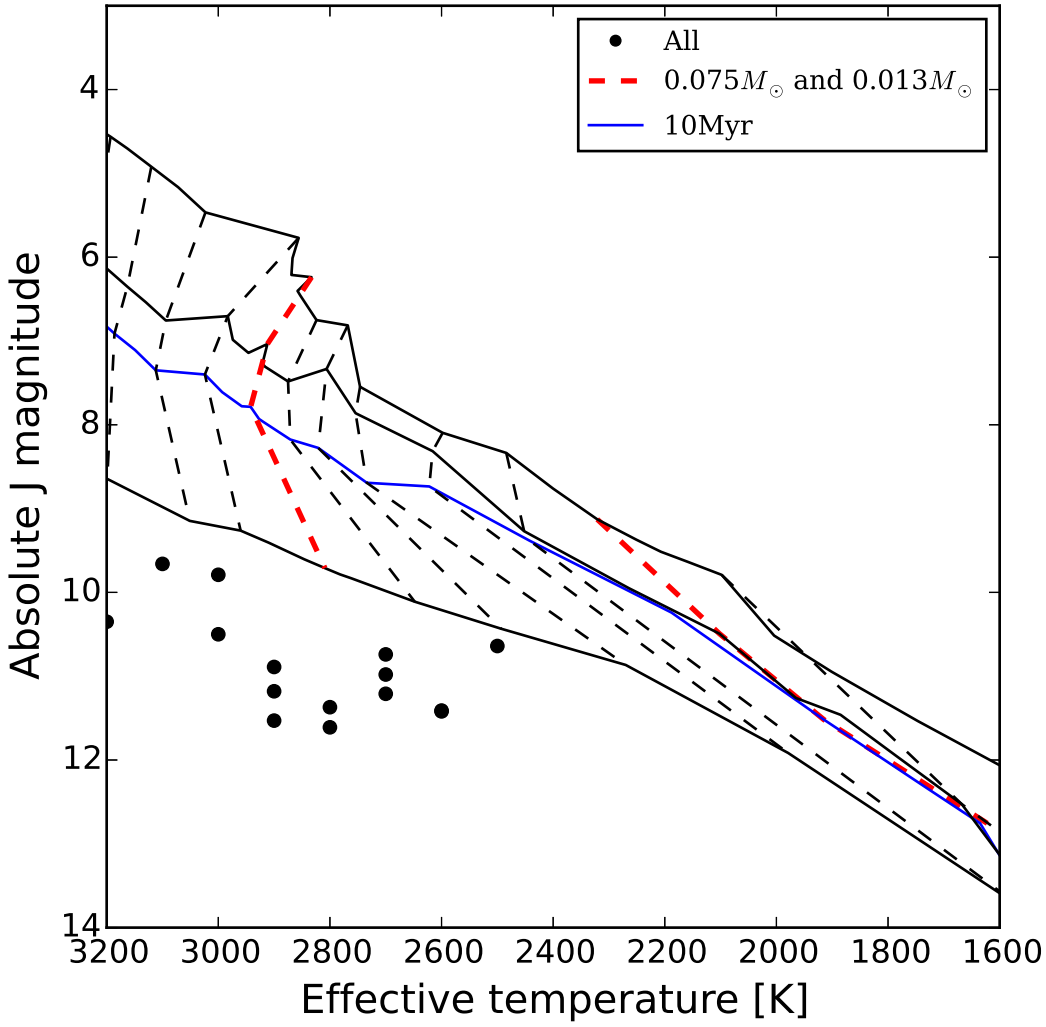

Figure 3.12: Photometric $T_{\rm eff}$ vs absolute $J-$band HR diagram. The lines show the synthetic HR diagram (BT-Settl; Allard et al., 2010). The solid lines show the age isochrones 1, 5, 10, 100 Myr from top to bottom. The dashed lines show the mass isochrones 0.007, 0.013, 0.02, 0.03, 0.04, 0.05, 0.06, 0.075, 0.1, 0.11, 0.15 $M_\odot$ from right to left (the red dashed lines indicate 0.013 and 0.075 $M_\odot$). The black dots indicate observed substellar candidates.

3.4.3 Comparison with Luhman et al. (2009)

We did not find any PMOs in our target regions. This means that the existence of PMOs may be rejected based on our comprehensive observations. Note that we select PMO sample within a extinction value $A_V < 4$, and thus we do not consider embedded objects with $A_V > 4$. We define our observational coverage in Taurus as 1.85 deg^2, except for the TAUV3 and TAUV4 fields due to a lack of i'-band data. Since the completeness depth varies with region, we conservatively adopt $i' = 24.3$ and $z' = 23.5$ as our completeness limit, which correspond with the predicted magnitudes of the masses 6 $M_{\rm Jup}$ and 4–5 $M_{\rm Jup}$ with distance $\sim$ 140 pc, age $\sim$ 1 Myr and $A_V < 4$. Therefore, our observation achieves a sensitivity down to 6 $M_{\rm Jup}$, covering 1.85 deg^2 regions, and did not find any PMOs.

Our coverage is smaller than that of Luhman et al. (2009), though we can compare our results with this study by scaling the results of Luhman et al. (2009) to the scale of our observation. The IMF in the Luhman et al. (2009) study extends down to 20 $M_{\rm Jup}$ in Taurus using the Spitzer and X-ray data, which are consistent with previous studies. The first PMO candidate was not included in the X-ray sample due to the lack of X-ray data, and the X-ray IMF also has no objects in the planetary mass regime. We recalculated the Salpeter slope to fit the power law to the IMF below 0.08 $M_\odot$ and found a slope of $\alpha = -0.47 \pm 0.10$, which is consistent with the value reported in the paper. Assuming a monotonic continuation of the power law, we would expect 14^{+7}_{-6} objects with $0.005 < M/M_\odot < 0.020$, which is detectable in our observation. Scaling the coverage of Luhman et al. (2009) ($\sim$ 5 deg^2) to our study ($\sim$ 1.85 deg^2), we expect 2–5 objects in our observation. Therefore, the lack of PMOs in our observation suggests that the IMF of Taurus may decrease sharply in the planetary mass regime. However, our result is based on a smaller FOV than that of Luhman et al. (2009), in which a PMO candidate has already been found. In order to appropriately compare these results, we need to extend our coverage in the TMC. Therefore, our result suggests that the IMF in the higher stellar density region of Taurus might lack objects in the planetary mass regime down to 6 $M_{\rm Jup}$.

3.4.4 Implications of the star formation in the TMC: Frequency of Planetary Mass Objects

We consider here the lack of PMOs in the TMC. In order to compare the TMC with other star-forming regions, we consider the fraction of BDs that have a mass in the planetary mass domain, $f_P = N_P/N_{\rm BD}$ (Scholz et al., 2012a). We show the fraction against our results in Table 3.14. (Scholz et al., 2012a) have conducted a large spectroscopic survey in NGC1333 to obtain spectra of substellar candidates. In other star forming regions, discussions in previous studies have been based on photometric data and partly followed-up spectroscopic data. Considering the incompleteness of the previous studies, Table 3.14 shows that most star forming regions are likely to have 10–20% PMOs to BDs. In contrast, our result shows an absence of PMO in our Taurus FOV.

We show that the abundance of PMOs is unaccountably lower for the massive members in the TMC and the frequency of PMOs in the TMC is also lower than that reported in the other star forming regions. We discuss the impact of our results on the substellar formation scenarios in the following paragraphs.

Table 3.14: Abundance of planetary mass objects in various star forming regions

Region	f_P [%]	Depth [$M_\odot$]	Reference
Taurus	~ 0	~ 0.006	This work
NGC1333	12 – 14	~ 0.006	Scholz et al. (2012a)
σ Orionis	~ 26	~ 0.006	Caballero et al. (2007)
Upper Scorpius	~ 10	0.01	Lodieu et al. (2011b)
ρ Ophiuchus	~ 20	0.03	Alves de Oliveira et al. (2012)
Chamaeleon I	~ 14	0.008	Mužić et al. (2012)

Turbulent fragmentation

This scenario can explain the formation of substellar mass objects as a simple extension of massive star and the universal IMF observed in several star forming regions. However, the universal IMF contradicts with the IMF of Taurus, which has higher typical mass and a long tail of substellar mass objects, although the Mach number of Taurus is rather consistent with other star forming regions (Kainulainen & Tan, 2013). Therefore this process is unimportant for the star formation in Taurus.

Dynamical ejection from proto-stellar or proto-planetary system

We report no PMOs in our FOV concentrated on the high stellar density regions. However, the L-type member candidate 2M0437+2331 is located apart from such regions. One scenario to explain the lack of PMOs in high stellar density regions is that PMOs which form through disk fragmentation are ejected away into the outer regions or Galactic field (Stamatellos & Whitworth, 2009). In fact, we found that the L-type candidate has a higher velocity in the proper motion, which might be caused by the ejection process. This mechanism can also explain the excess of free-floating PMOs in the Galactic field (Sumi et al., 2011). If this is a dominant process for PMO formation, we can identify the distributed planetary mass population for massive objects by observing a larger areas of Taurus. In this case, the IMF of Taurus extends down to planetary mass, which is consistent with the theory of opacity-limited fragmentation and the observational results for several star forming regions. However, it is unlikely that the low stellar density of Taurus promotes the ejection process from multiple stellar/planetary systems. For instance, stellar encounters could facilitate the ejection of bound BD companions from their host stars (Goodwin & Whitworth, 2007b). However, the frequency of the stellar encounters would become lower in low density regions.

Fragmentation of infalling gas into stellar cluster

We also suggest that the L-type member might be contamination from the nearby young cluster. Therefore, it is possible that no PMOs exists even in the larger areas of the TMC, and the predicted minimum mass is actually higher in the TMC. Based on the currently available census, the stellar density of Taurus is

significantly lower than that of other regions. Bonnell et al. (2008, 2011) have suggested that BDs in clusters form through gravitational fragmentation of infalling gas. The fact that larger clusters attract more gas from surrounding molecular clouds might explain the low abundance of BDs in diffuse cluster like Taurus. This scenario suggests that the abundance of low mass members in a cluster might depend on the number density of cluster objects, and BDs would be the extent of the low mass stellar members based on the similarity of the resultant physical properties. Extending this scenario to the planetary mass regime, if PMOs also could be regarded as an extent of low mass stellar and BD mass members, we would expect a lower abundance of PMOs in Taurus in comparison with other star forming regions. However, since the mass resolution of Bonnell et al. (2008, 2011) is limited to 0.0167 $M_{\rm Jup}$, they provide no values for the planetary mass regime.

Fragmentation of massive circumstellar disk

The disk fragmentation process also suggests a dependency of substellar formation on the stellar density. The disk fragmentation process is driven by stellar encounters (Thies et al., 2010) or disk–disk collisions (Shen et al., 2010). Since this encounter scenario depends on stellar density, the low stellar density of Taurus might cause low abundance of substellar objects in the TMC. The limitations of these processes could explain the low abundance of BDs and PMOs in diffuse clusters like Taurus. However, it is unlikely that these processes only suppress the formation of PMOs, though it is an important suggestion that the formation of the population at the bottom of the IMF might be affected by the surrounding environments.

Photo-evaporation of OB stars

Another way to explain the low abundance of PMOs in Taurus is the lack of OB stars which might produce BDs and PMOs through the photo-evaporation of the nearby prestellar cores . If this mechanism was dominant for the formation of substellar mass objects, we would find that the spatial difference in the abundance of BDs and PMOs is greater in the vicinity of OB stars. However, as shown in §2.4.2, the spatial distribution of BDs is constant or distributed with the stellar mass members in the ONC, which contradicts the central concentration predicted by this scenario.

In conclusion, the fragmentation of infalling gas in the clusters might explain the peculiar form of the IMF in Taurus, and the other formation processes might be unimportant in Taurus. Note that these theories consider PMOs as a extension of BDs and no different properties between PMOs and BDs. One can explain the lower abundance of PMOs by the higher minimum mass predicted in the star formation. The process of the infalling gas fragmentation might cause higher minimum mass in the diffuse stellar cluster, however it has not unveiled the planetary mass formation due to the resolution of the simulation. Therefore we need additional effects in order to explain the low frequency of PMOs in Taurus. As additional effects, the minimum mass has been predicted to depend on the metallicity. Bate (2005) investigated the dependency of the metallicity which increases the minimum mass of a BD to 9 $M_{\rm Jup}$. However, his hydrodynamical simulation assumes an extreme case of the metallicity, namely $\log(Z/Z_{\odot}) = -3.3$, which corresponds to that of an old globule cluster. Also, the analytical study of Low & Lynden-Bell (1976) suggested that the dependency of

the minimum mass of the metallicity is insignificant ($Z^{-1/7}$) and therefore is not applicable for nearby star forming regions. We can explain the higher minimum mass of star formation by considering the magnetic field. Magnetic field tends to quench the formation of BDs by disk fragmentation because they tend to suppress the formation of big massive disks at the class 0 phase and to stabilize them whenever they form (Hennebelle, 2012). However, there has been no large scale simulation resolving the planetary mass regime including the effect of magnetic fields. Therefore, our studies only confirm the trend of magnetic fields suppressing the formation of BDs and PMOs.

To be summarized, we obtained deep optical/infrared images using the Subaru/Suprime-Cam and the Okayama 1.88m/ISLE. Combining our deep images with the other infrared data, we first achieve the sensitivity down to 6 $M_{\rm Jup}$ with $A_V < 4$. Our aims to observe the TMC are to reveal the bottom of IMF in the TMC and the impact of several substellar forming theories on the PMO formation. Based on several color selections and proper motion analysis, we selected 2 PMO candidates and obtained these spectra using the Subaru/IRCS. As a result, we did not find any PMO in our FOV (1.85 deg^2). In contrast to the frequency of PMOs being 10 – 20% in other star forming regions, our results first imply that the frequency of low mass BDs and PMOs is quite low in the TMC. The lack of PMO could be explained by what the substellar mass objects are formed through fragmentation of infalling gas into cluster. Another explanation is that the minimum jeans mass is higher in the TMC. However, since the previous theories predict the formation of $1-10$ $M_{\rm Jup}$ objects in star forming regions, it needs different formation mechanisms to explain the frequency of PMOs in the Taurus molecular cloud.

Chapter 4

Summary and Conclusions

We have reported the results of a near-infrared multi-object and long-slit spectroscopic survey in the Orion Nebular Cluster, and the most sensitive optical/infrared imaging and spectroscopy in the Taurus Molecular Cloud. Our main results are the following:

Orion Nebular Cluster

1. We presented 12 near-infrared spectra of BD candidates. We confirm that eight of those show strong water absorption and have a very low temperature ($T_{\rm eff} < 3000$ K). We identify two of the cold objects as young BD mass members, and one of them as a BD/planetary-mass boundary object.

2. We report a spectroscopic estimate of the stellar to substellar ratio in the outer region ($1.7' < r < 5.7'$) of $R = 3.5 \pm 0.8$, which is consistent with that in the central region ($r < 2.5'$) derived by Slesnick et al. (2004). In a previous photometric study with a larger FOV ($r < 12.5'$; Andersen+2011), it was reported that the IMF in Orion is not universal locally, but that the stellar to substellar ratio decreases from the center to the outer region. However, determining the IMF based only on photometric data depends on the correction of the background contamination. We carefully discuss the membership of each object based on the spectroscopic sample, and conclude that the IMF is universal at least in the local area within $5.7'$ of the center of Orion. Observational studies in several star forming regions suggest that the substellar IMF could be universal. However, most previous studies have been based mainly on photometric data, and limited in the observational coverage. In order to check whether the IMF is universal, we need to investigate the IMF based on spectroscopic data for the whole of the cluster. Our study stresses this necessity.

3. Since the ONC has several OB stars in the central regions, the photo-evaporation would produce the small cores becoming the substellar mass objects around the OB stars if the effect was dominant. We report that the substellar IMF is universal between the outer and the central regions. Therefore our results rather support that the OB star's photo-ionizing process is unimportant in the ONC.

4. We found that several stellar and BD mass candidates appear to be older than 10 Myr on the HR diagram. Following a consideration of the probability of the Galactic field contamination, we concluded

that it is unlikely that the BD candidates are actually Galactic field stars, but that the stellar mass objects might be contamination from the Galactic field. We show that many candidates that appear older have spectral features of youth, which indicates that such objects are actually young stellar objects. The faintness on the HR diagram can be explained by light scattering from the central star due to the circumstellar structure, or by episodic accretion.

Taurus Molecular Cloud

1. We conducted an extremely deep optical imaging, and a near-infrared imaging/spectroscopy follow-up. Combining these measurements with near-infrared data (UKIDSS; Spitzer; WISE), we achieved a sensitivity down to 6 $M_{\rm Jup}$ for $A_V < 4$ sample with the large FOV covering a few square degrees, the best sensitivity achieved to date.

2. We calculated the proper motions of our candidates, previous known field stars and Taurus members. We found that the measured proper motion of Taurus members is slightly mismatched with previous reported values. Since our measured values are consistent with previous values using the UNSO-A2.0 catalogue, we suggest that mismatch might be caused by the difference in the catalogue used in the calculation.

3. Based on several color criteria and proper motion analysis, we found two PMO candidates with $A_V < 4$. We carried out a near-infrared spectroscopic follow-up for these candidates and found that the candidates are background field dwarfs. We found that some candidates have infrared excess in the SEDs and similar proper motions as the Taurus members, however we do not include the candidates in our PMO list because of the faintness or high visual extinction. To confirm the precise mass and membership, we need to conduct a spectroscopic follow-up.

4. We found no PMOs in our sample, which was complete down to 6 $M_{\rm Jup}$ and $A_V < 4$, covering 1.85 deg^2. In comparison with a previous study of Taurus (Luhman et al., 2009), our result clearly shows a lack of PMO members, although an extrapolation of the IMF would predict 2–5 PMOs in our FOV of Taurus.

5. We give the first demonstration that the IMF at the planetary mass regime is not always universal. In comparison with other star forming regions, our estimated abundance of PMOs is significantly lower than the 12–14% of NGC1333 and 10–20% of other star forming regions. Although the spectroscopic observation of NGC1333 is comparable with our study, we note that the results for other star forming regions might be modified in future since the majority of these studies were not completed with spectroscopy in the planetary mass regime.

6. Our results suggest that the lower limit of the IMF in Taurus is higher than in other star forming regions. Since the opacity-limited fragmentation predicts the existence of PMOs with a few Jupiter masses, we must consider a non-standard scenario to explain our result. In order to explain the lack of PMOs, we suggest the following scenarios, 1) Substellar object formation in a diffuse cluster Bonnell et al. (2008, 2011) might explain the lack of PMOs in Taurus; 2) The minimum Jeans mass is high in

the TMC for the predicted values. In order to explain it, we need to include additional effects (e.g., metallicity, magnetic force) in a large scale simulation.

Our results point the way for future works to develop the study of planetary mass formation. We have revealed the very low mass population below the hydrogen burning limit in two nearby rich star forming regions, the ONC and TMC. In the ONC, we added several new BD member to the spectroscopic sample. However, many photometric sample of BD and PMO candidates needs to be identified using a spectrograph. A multi-object slit spectrograph (e.g. MOIRCS; FMOS) would be quite useful for revealing the population down to several Jupiter masses and the distribution of BD members in Orion. On the other hand, since the sensitivity of recent observations is limited down to 5 $M_{\rm Jup}$ even in the most sensitive imaging (Lucas et al., 2005), we have not confirmed the population with a few Jupiter masses, whose existence has been suggested by opacity-limited fragmentation theories and the microlensing observation in the Galactic field (Sumi et al., 2011). In Taurus, we made the first demonstration of the lack of PMO in this region, which is at odds with other star forming regions since many authors have shown the existence of PMOs in star forming regions. In order to confirm this result in a larger FOV, we propose the use of Hyper Suprime-Cam (HSC), a powerful instrument whose FOV ($\sim$ 1.5 deg) can largely cover the star forming fields in Taurus. We intend to obtain the largest proper motion sample with a long time baseline in Taurus using HSC. Advanced telescopes with larger diameter are planned for the future (e.g., TMT; E-ELT), which will allow us to reveal the population at the bottom of the IMF. Since such telescopes have an extremely large power for gathering objects' light and high resolution power, but a relatively small FOV, they could detect a few Jupiter mass objects in a rich and compact cluster like the ONC, or very low mass BDs and even PMOs in a distant ($\gtrsim$ 1 kpc) young cluster (e.g., the W3 star forming region; Ojha et al., 2009). The James Webb Space Telescope (JWST) is suitable for detecting extremely cool PMOs or young substellar objects because of its capability of mid-IR wavelength (0.6–28.3μm) measurement with a mirror diameter ($\sim$ 6.5 m) comparable with recent large telescopes at the ground. In particular, open clusters are good sites for this study since they have various ranges of age ($>$ 10 Myr), abundant cluster members and negligible visual extinction. Pacucci et al. (2013) simulated the detectability of free-floating PMOs in open clusters, and found that JWST enables the detection of cool PMOs (T = 500 K) of the Pleiades in 1 hour using a 4.4 μm detector array.

Bibliography

Allard, F., Homeier, D., & Freytag, B. 2010, ArXiv e-prints

Aller, K. M., Kraus, A. L., Liu, M. C., et al. 2013, ApJ, 773, 63

Alves, J. & Bouy, H. 2012, A&A, 547, A97

Alves de Oliveira, C., Moraux, E., Bouvier, J., & Bouy, H. 2012, A&A, 539, A151

Alves de Oliveira, C., Moraux, E., Bouvier, J., et al. 2010, A&A, 515, A75

Alves de Oliveira, C., Moraux, E., Bouvier, J., et al. 2013, A&A, 549, A123

Andersen, M., Meyer, M. R., Greissl, J., & Aversa, A. 2008, ApJL, 683, L183

Andersen, M., Meyer, M. R., Robberto, M., Bergeron, L. E., & Reid, N. 2011, A&A, 534, A10+

André, P., Men'shchikov, A., Bontemps, S., et al. 2010, A&A, 518, L102

André, P., Ward-Thompson, D., & Greaves, J. 2012, Science, 337, 69

Asplund, M., Grevesse, N., Sauval, A. J., & Scott, P. 2009, ARA&A, 47, 481

Baraffe, I., Chabrier, G., & Gallardo, J. 2009, ApJL, 702, L27

Barber, R. J., Miller, S., Dello Russo, N., & Tennyson, J. 2008, LPI Contributions, 1405, 8147

Bastian, N., Covey, K. R., & Meyer, M. R. 2010, ARA&A, 48, 339

Bate, M. R. 2005, MNRAS, 363, 363

Bate, M. R., Bonnell, I. A., & Bromm, V. 2002, MNRAS, 332, L65

Bate, M. R., Bonnell, I. A., & Bromm, V. 2003, MNRAS, 339, 577

Bayo, A., Barrado, D., Stauffer, J., et al. 2011, A&A, 536, A63

Bertin, E. 2006, in Astronomical Society of the Pacific Conference Series, Vol. 351, Astronomical Data Analysis Software and Systems XV, ed. C. Gabriel, C. Arviset, D. Ponz, & S. Enrique, 112

Bertout, C. & Genova, F. 2006, A&A, 460, 499

Bihain, G., Rebolo, R., Zapatero Osorio, M. R., et al. 2009, A&A, 506, 1169

Bochanski, J. J., Hawley, S. L., Covey, K. R., et al. 2010, AJ, 139, 2679

Bonnell, I. A., Clark, P., & Bate, M. R. 2008, MNRAS, 389, 1556

Bonnell, I. A., Smith, R. J., Clark, P. C., & Bate, M. R. 2011, MNRAS, 410, 2339

Boss, A. P. 2001, ApJL, 551, L167

Boudreault, S., Lodieu, N., Deacon, N. R., & Hambly, N. C. 2012, MNRAS, 426, 3419

Boulade, O., Charlot, X., Abbon, P., et al. 2003, in Society of Photo-Optical Instrumentation Engineers (SPIE) Conference Series, Vol. 4841, Instrument Design and Performance for Optical/Infrared Ground-based Telescopes, ed. M. Iye & A. F. M. Moorwood, 72–81

Bouy, H., Huélamo, N., Martín, E. L., et al. 2009, A&A, 493, 931

Bowler, B. P., Liu, M. C., & Cushing, M. C. 2009, ApJ, 706, 1114

Boyd, D. F. A. & Whitworth, A. P. 2005, A&A, 430, 1059

Briceño, C., Luhman, K. L., Hartmann, L., Stauffer, J. R., & Kirkpatrick, J. D. 2002a, ApJ, 580, 317

Briceño, C., Luhman, K. L., Hartmann, L., Stauffer, J. R., & Kirkpatrick, J. D. 2002b, ApJ, 580, 317

Burrows, C. J., Stapelfeldt, K. R., Watson, A. M., et al. 1996, ApJ, 473, 437

Caballero, J. A., Béjar, V. J. S., Rebolo, R., et al. 2007, A&A, 470, 903

Caballero, J. A., Burgasser, A. J., & Klement, R. 2008, A&A, 488, 181

Cameron, E. 2011, PASA, 28, 128

Cardelli, J. A., Clayton, G. C., & Mathis, J. S. 1989, ApJ, 345, 245

Casali, M., Adamson, A., Alves de Oliveira, C., et al. 2007, A&A, 467, 777

Chabrier, G. 2003, PASP, 115, 763

Chabrier, G. 2005, in Astrophysics and Space Science Library, Vol. 327, The Initial Mass Function 50 Years Later, ed. E. Corbelli, F. Palla, & H. Zinnecker, 41

Cohen, M., Wheaton, W. A., & Megeath, S. T. 2003, AJ, 126, 1090

Connelley, M. S., Reipurth, B., & Tokunaga, A. T. 2007, AJ, 133, 1528

Covey, K. R., Hawley, S. L., Bochanski, J. J., et al. 2008, AJ, 136, 1778

Cruz, K. 2008, in Astronomical Society of the Pacific Conference Series, Vol. 393, New Horizons in Astronomy, ed. A. Frebel, J. R. Maund, J. Shen, & M. H. Siegel, 51

Cuillandre, J.-C., Luppino, G. A., Starr, B. M., & Isani, S. 2000, in Society of Photo-Optical Instrumentation Engineers (SPIE) Conference Series, Vol. 4008, Optical and IR Telescope Instrumentation and Detectors, ed. M. Iye & A. F. Moorwood, 1010–1021

Cushing, M. C., Kirkpatrick, J. D., Gelino, C. R., et al. 2011, ApJ, 743, 50

Cushing, M. C., Marley, M. S., Saumon, D., et al. 2008, ApJ, 678, 1372

Cutri, R. M. & et al. 2012, VizieR Online Data Catalog, 2311, 0

Cutri, R. M., Wright, E. L., Conrow, T., et al. 2012, Explanatory Supplement to the WISE All-Sky Data Release Products, Tech. rep.

Da Rio, N., Robberto, M., Hillenbrand, L. A., Henning, T., & Stassun, K. G. 2012, ApJ, 748, 14

de Marchi, G. & Paresce, F. 2001, in Astronomische Gesellschaft Meeting Abstracts, Vol. 18, Astronomische Gesellschaft Meeting Abstracts, ed. E. R. Schielicke, 551

Dobashi, K. 2011, PASJ, 63, 1

D'Orazi, V., Randich, S., Flaccomio, E., et al. 2009, A&A, 501, 973

Ducourant, C., Teixeira, R., Périé, J. P., et al. 2005, A&A, 438, 769

Dye, S., Warren, S. J., Hambly, N. C., et al. 2006, MNRAS, 372, 1227

Eisner, J. A. & Carpenter, J. M. 2006, ApJ, 641, 1162

Fazio, G. G., Hora, J. L., Allen, L. E., et al. 2004, ApJS, 154, 10

Freytag, B., Allard, F., Ludwig, H.-G., Homeier, D., & Steffen, M. 2010, A&A, 513, A19+

Frink, S., Röser, S., Neuhäuser, R., & Sterzik, M. F. 1997, A&A, 325, 613

Geers, V., Scholz, A., Jayawardhana, R., et al. 2011, ApJ, 726, 23

Ghez, A. M., Neugebauer, G., & Matthews, K. 1993, AJ, 106, 2005

Goodwin, S. P. & Whitworth, A. 2007a, A&A, 466, 943

Goodwin, S. P. & Whitworth, A. 2007b, A&A, 466, 943

Goodwin, S. P., Whitworth, A. P., & Ward-Thompson, D. 2004, A&A, 419, 543

Guieu, S., Dougados, C., Monin, J.-L., Magnier, E., & Martín, E. L. 2006, A&A, 446, 485

Hambly, N. C., Collins, R. S., Cross, N. J. G., et al. 2008, MNRAS, 384, 637

Hennebelle, P. 2012, in EAS Publications Series, Vol. 57, EAS Publications Series, ed. C. Reylé, C. Charbonnel, & M. Schultheis, 91–127

Hillenbrand, L. A. 1997, AJ, 113, 1733

Hillenbrand, L. A. & Carpenter, J. M. 2000, ApJ, 540, 236

Hillenbrand, L. A. & Hartmann, L. W. 1998, ApJ, 492, 540

Jarrett, T. H., Masci, F., Tsai, C. W., et al. 2012, AJ, 144, 68

Jeffries, R. D. 2012, in EAS Publications Series, Vol. 57, EAS Publications Series, ed. C. Reylé, C. Charbonnel, & M. Schultheis, 45–89

Kainulainen, J. & Tan, J. C. 2013, A&A, 549, A53

Kenyon, S. J., Gómez, M., & Whitney, B. A. 2008, Low Mass Star Formation in the Taurus-Auriga Clouds, ed. B. Reipurth, 405

Kirkpatrick, J. D., Barman, T. S., Burgasser, A. J., et al. 2006, ApJ, 639, 1120

Kirkpatrick, J. D., Cushing, M. C., Gelino, C. R., et al. 2011, ApJS, 197, 19

Kobayashi, N., Tokunaga, A. T., Terada, H., et al. 2000, in Society of Photo-Optical Instrumentation Engineers (SPIE) Conference Series, Vol. 4008, Optical and IR Telescope Instrumentation and Detectors, ed. M. Iye & A. F. Moorwood, 1056–1066

Kraus, A. L. & Hillenbrand, L. A. 2007, ApJ, 662, 413

Kroupa, P. & Bouvier, J. 2003, MNRAS, 346, 369

Kroupa, P., Tout, C. A., & Gilmore, G. 1993, MNRAS, 262, 545

Kumar, M. S. N. & Schmeja, S. 2007, A&A, 471, L33

Kuzuhara, M., Tamura, M., Ishii, M., et al. 2011, AJ, 141, 119

Lada, C. J., Muench, A. A., Lada, E. A., & Alves, J. F. 2004, AJ, 128, 1254

Larson, R. B. 1999, in Star Formation 1999, ed. T. Nakamoto, 336–340

Lee, T. A. 1968, ApJ, 152, 913

Leinert, C., Zinnecker, H., Weitzel, N., et al. 1993, A&A, 278, 129

Lodieu, N. 2013, MNRAS, 431, 3222

Lodieu, N., de Wit, W.-J., Carraro, G., et al. 2011a, A&A, 532, A103

Lodieu, N., Deacon, N. R., & Hambly, N. C. 2012a, MNRAS, 422, 1495

Lodieu, N., Deacon, N. R., Hambly, N. C., & Boudreault, S. 2012b, MNRAS, 426, 3403

Lodieu, N., Hambly, N. C., Dobbie, P. D., et al. 2011b, MNRAS, 418, 2604

Lodieu, N., Hambly, N. C., Jameson, R. F., et al. 2007, MNRAS, 374, 372

Low, C. & Lynden-Bell, D. 1976, MNRAS, 176, 367

Lucas, P. W., Hoare, M. G., Longmore, A., et al. 2008, MNRAS, 391, 136

Lucas, P. W. & Roche, P. F. 2000, MNRAS, 314, 858

Lucas, P. W., Roche, P. F., Allard, F., & Hauschildt, P. H. 2001, MNRAS, 326, 695

Lucas, P. W., Roche, P. F., & Tamura, M. 2005, MNRAS, 361, 211

Lucas, P. W., Weights, D. J., Roche, P. F., & Riddick, F. C. 2006, MNRAS, 373, L60

Luhman, K. L. 2004, ApJ, 617, 1216

Luhman, K. L. 2006, ApJ, 645, 676

Luhman, K. L. 2007, ApJS, 173, 104

Luhman, K. L., Allen, P. R., Espaillat, C., Hartmann, L., & Calvet, N. 2010, ApJS, 186, 111

Luhman, K. L., Briceño, C., Stauffer, J. R., et al. 2003a, ApJ, 590, 348

Luhman, K. L. & Mamajek, E. E. 2010, ApJL, 716, L120

Luhman, K. L., Mamajek, E. E., Allen, P. R., & Cruz, K. L. 2009, ApJ, 703, 399

Luhman, K. L., Rieke, G. H., Young, E. T., et al. 2000, ApJ, 540, 1016

Luhman, K. L., Stauffer, J. R., Muench, A. A., et al. 2003b, ApJ, 593, 1093

McLaughlin, D. E., Anderson, J., Meylan, G., et al. 2006, ApJS, 166, 249

Miller, G. E. & Scalo, J. M. 1979, ApJS, 41, 513

Miyazaki, S., Komiyama, Y., Sekiguchi, M., et al. 2002, PASJ, 54, 833

Mohanty, S., Jayawardhana, R., Huélamo, N., & Mamajek, E. 2007, ApJ, 657, 1064

Monet, D. G. 1998, in Bulletin of the American Astronomical Society, Vol. 30, American Astronomical Society Meeting Abstracts, 120.03

Muench, A., Getman, K., Hillenbrand, L., & Preibisch, T. 2008, Star Formation in the Orion Nebula I: Stellar Content, 483

Muench, A. A., Lada, C. J., Luhman, K. L., Muzerolle, J., & Young, E. 2007, AJ, 134, 411

Mužić, K., Scholz, A., Geers, V., Fissel, L., & Jayawardhana, R. 2011, ApJ, 732, 86

Mužić, K., Scholz, A., Geers, V., Jayawardhana, R., & Tamura, M. 2012, ApJ, 744, 134

Muzerolle, J., Hartmann, L., & Calvet, N. 1998, AJ, 116, 2965

Neuhäuser, R., Mugrauer, M., Seifahrt, A., Schmidt, T. O. B., & Vogt, N. 2008, A&A, 484, 281

Oasa, Y., Tamura, M., & Sugitani, K. 1999, ApJ, 526, 336

Ochsenbein, F., Bauer, P., & Marcout, J. 2000, A&AS, 143, 23

O'dell, C. R. & Wong, K. 1996, AJ, 111, 846

Offner, S. S. R., Clark, P. C., Hennebelle, P., et al. 2013, ArXiv e-prints

Ojha, D. K., Tamura, M., Nakajima, Y., et al. 2009, ApJ, 693, 634

Oliveira, J. M., Jeffries, R. D., & van Loon, J. T. 2009, MNRAS, 392, 1034

Ouchi, M., Shimasaku, K., Okamura, S., et al. 2004, ApJ, 611, 660

Pacucci, F., Ferrara, A., & D'Onghia, E. 2013, ApJL, 778, L42

Padgett, D. L., Rebull, L. M., Stapelfeldt, K. R., et al. 2008, ApJ, 672, 1013

Padoan, P. & Nordlund, Å. 2004, ApJ, 617, 559

Parker, R. J., Bouvier, J., Goodwin, S. P., et al. 2011, MNRAS, 412, 2489

Peña Ramírez, K., Béjar, V. J. S., Zapatero Osorio, M. R., Petr-Gotzens, M. G., & Martín, E. L. 2012, ApJ, 754, 30

Petr-Gotzens, M., Alcalá, J. M., Briceño, C., et al. 2011, The Messenger, 145, 29

Quanz, S. P., Goldman, B., Henning, T., et al. 2010, ApJ, 708, 770

Rayner, J. T., Cushing, M. C., & Vacca, W. D. 2009, ApJS, 185, 289

Rebull, L. M., Koenig, X. P., Padgett, D. L., et al. 2011, ApJS, 196, 4

Rebull, L. M., Padgett, D. L., McCabe, C.-E., et al. 2010, ApJS, 186, 259

Rees, M. J. 1976, MNRAS, 176, 483

Reid, I. N., Gizis, J. E., & Hawley, S. L. 2002, AJ, 124, 2721

Reipurth, B. 2000, AJ, 120, 3177

Reipurth, B. & Clarke, C. 2001, AJ, 122, 432

Ricci, L., Robberto, M., & Soderblom, D. R. 2008, AJ, 136, 2136

Riddick, F. C., Roche, P. F., & Lucas, P. W. 2007, MNRAS, 381, 1077

Rieke, G. H., Young, E. T., Engelbracht, C. W., et al. 2004, ApJS, 154, 25

Robberto, M., Soderblom, D. R., Scandariato, G., et al. 2010, AJ, 139, 950

Robichon, N., Arenou, F., Mermilliod, J.-C., & Turon, C. 1999, A&A, 345, 471

Robin, A. C., Reylé, C., Derrière, S., & Picaud, S. 2003, A&A, 409, 523

Robin, A. C., Reylé, C., Derrière, S., & Picaud, S. 2004, A&A, 416, 157

Rossow, W. B. 1978, Icarus, 36, 1

Salpeter, E. E. 1955, ApJ, 121, 161

Scelsi, L., Maggio, A., Micela, G., et al. 2007, A&A, 468, 405

Scholz, A., Geers, V., Jayawardhana, R., et al. 2009, ApJ, 702, 805

Scholz, A., Jayawardhana, R., Muzic, K., et al. 2012a, ApJ, 756, 24

Scholz, A., Muzic, K., Geers, V., et al. 2012b, ApJ, 744, 6

Shen, S., Wadsley, J., Hayfield, T., & Ellens, N. 2010, MNRAS, 401, 727

Skrutskie, M. F., Cutri, R. M., Stiening, R., et al. 2006, AJ, 131, 1163

Slesnick, C. L., Hillenbrand, L. A., & Carpenter, J. M. 2004, ApJ, 610, 1045

Smith, J. A., Tucker, D. L., Kent, S., et al. 2002, AJ, 123, 2121

Stamatellos, D. & Whitworth, A. P. 2009, MNRAS, 392, 413

Stapelfeldt, K. R., Krist, J. E., Menard, F., et al. 1998, ApJL, 502, L65

Stauffer, J. R., Schultz, G., & Kirkpatrick, J. D. 1998, ApJL, 499, L199

Sumi, T., Kamiya, K., Bennett, D. P., et al. 2011, Nature, 473, 349

Sung, H. & Bessell, M. S. 2010, AJ, 140, 2070

Suzuki, R., Tokoku, C., Ichikawa, T., et al. 2008, PASJ, 60, 1347

Tamura, M., Itoh, Y., Oasa, Y., & Nakajima, T. 1998, Science, 282, 1095

Tanaka, M., Letip, A., Nishimaki, Y., et al. 2007, PASJ, 59, 939

Teixeira, R., Ducourant, C., Sartori, M. J., et al. 2000, A&A, 361, 1143

Thies, I. & Kroupa, P. 2007, ApJ, 671, 767

Thies, I., Kroupa, P., Goodwin, S. P., Stamatellos, D., & Whitworth, A. P. 2010, ApJ, 717, 577

Todorov, K., Luhman, K. L., & McLeod, K. K. 2010, ApJL, 714, L84

van Dokkum, P. G. 2001, PASP, 113, 1420

Warren, S. J., Hambly, N. C., Dye, S., et al. 2007, MNRAS, 375, 213

Weights, D. J., Lucas, P. W., Roche, P. F., Pinfield, D. J., & Riddick, F. 2009, MNRAS, 392, 817

West, A. A., Hawley, S. L., Bochanski, J. J., et al. 2008, AJ, 135, 785

White, R. J. & Basri, G. 2003, ApJ, 582, 1109

Whitworth, A. P. & Stamatellos, D. 2006a, A&A, 458, 817

Whitworth, A. P. & Stamatellos, D. 2006b, A&A, 458, 817

Whitworth, A. P. & Zinnecker, H. 2004, A&A, 427, 299

Wright, E. L., Eisenhardt, P. R. M., Mainzer, A. K., et al. 2010, AJ, 140, 1868

Yagi, M., Kashikawa, N., Sekiguchi, M., et al. 2002, AJ, 123, 66

Yanagisawa, K., Okita, K., Shimizu, Y., et al. 2008, in Society of Photo-Optical Instrumentation Engineers (SPIE) Conference Series, Vol. 7014, Society of Photo-Optical Instrumentation Engineers (SPIE) Conference Series

Yanagisawa, K., Shimizu, Y., Okita, K., et al. 2006, in Society of Photo-Optical Instrumentation Engineers (SPIE) Conference Series, Vol. 6269, Society of Photo-Optical Instrumentation Engineers (SPIE) Conference Series

Zapatero Osorio, M. R., Béjar, V. J. S., Martín, E. L., et al. 2000, Science, 290, 103